# REANALYSIS OF THE GREAT LAKES DROGUE STUDIES DATA

## FINAL REPORT

AKIRA OKUBO
CURTIS C. EBBESMEYER
JONATHAN M. HELSETH
ALAN S. ROBBINS

marine sciences research center
state university of new york

SPECIAL REPORT 2

REFERENCE 76-2

MARINE SCIENCES RESEARCH CENTER
STATE UNIVERSITY OF NEW YORK
STONY BROOK, NEW YORK 11794

# REANALYSIS OF THE GREAT LAKES DROGUE STUDIES DATA: FINAL REPORT

Akira Okubo*, Curtis C. Ebbesmeyer**,
Jonathan M. Helseth*** and Alan S. Robbins*

February 15, 1976

*Sponsored by Great Lakes Environmental Research Laboratory, National Oceanic and Atmospheric Administration Ann Arbor, Michigan*

*Contract No.* 03-5-022-65

* The Marine Sciences Research Center, State University of New York, Stony Brook

** Evans-Hamilton, Inc., 6306 21st Ave. N.E., Seattle, Wash. 98115. Also affiliated with the Marine Sciences Research Center, SUNY, Stony Brook

*** Evans-Hamilton, Inc., 6306 21st Ave. N.E., Seattle, Wash. 98115

Special Report 2

Reference 76-2

Approved for Distribution

T.R. Schubel

J. R. Schubel, Director

Akira Okubo

A. Okubo
Principal Investigator

TABLE OF CONTENTS

LIST OF TABLES

## LIST OF FIGURES

LIST OF FIGURES
*(continued)*

ABSTRACT

In this report we reanalyse the Great Lakes Drogue Studies data taken in 1964. Original drogue position data are edited into smoothed position data for this purpose. The edited data are then processed using linear regression procedures to calculate not only Lagrangian deformations but also velocity gradient parameters, i.e. divergence, vorticity, deformation rates. The linear regression method also enables evaluation of turbulent characteristics, in particular momentary eddy diffusivities. The results show that i) the drogue area is controlled primarily by the cumulative effect of horizontal divergence, ii) a simple vorticity balance is established, iii) turbulence characteristics are generally consistent with the previous estimates by Okubo and Farlow in 1967, iv) momentary eddy diffusivities are relatively small and average $2 \times 10^2$ $cm^2/sec$ for all experiments. Values of the Lagrangian deformation and momentary eddy diffusivities are fed into the analytical solution of time-dependent advection-diffusion equation and the result shows favorable comparison with observed gross-scale drogue dispersion. Inspection of patterns within gross-scale drogue groups revealed that each group was composed of an average of five clusters. Small-scale variability was examined by computing the velocity gradient parameters for each cluster. Drogues tend to cluster over local convergences while the clusters themselves tend to diverge; that is, the gross-scale expands, small-scale tends to contract. A statistical test shows that 10-15 drogues are required to achieve a standard deviation equal to the 95% confidence limit of the gross-scale drogue group. This provides a guideline for designing future dispersion experiments.

# CHAPTER 1
# INTRODUCTION

During the summer of 1964 the Great Lakes-Illinois River Basins Project of the U. S. Federal Water Pollution Control Administration conducted a series of field studies with the use of drogues (i.e. current followers) in southern Lake Michigan and western Lake Erie. These studies were designed to obtain Lagrangian characteristics of diffusion, e.g. the root-mean-square distances between a pair of drogues. The study provided information on the scale and intensity of horizontal diffusion present at depths of 5 and 20 ft during the time of sampling. The ultimate goal of these studies was to predict the concentration distribution of pollutants discharged from rivers and sewage outfalls in the Great Lakes.

The details of the drogue construction and of the field methods were reported by Farlow (1965). And the analysis of the data was presented by Okubo and Farlow (1967). A complete report which includes the prediction of pollutant distributions was given by Okubo and Verber (1967).

The drogue experiments represent one of the most significant field studies of natural diffusion ever undertaken. Yet the data analyses were limited to discuss the statistical characteristics of drogue dispersion by the use of conventional methods of diffusion. We believed that a new look at the drogue data was now warranted based on recent advances in data analysis of current followers (Okubo, Ebbesmeyer and Helseth (1976)). That analysis shows that (i) we can determine Lagrangian deformations and turbulence statistics directly from drogue position data, (ii) such determinations allow time-dependent advection-diffusion equations to be directly evaluated, and (iii) those deformations can be transformed into velocity gradient parameters, i.e. divergence, vorticity, stretching deformation rate and shearing deformation rate so that the result may be compared with another new technique in determining these velocity gradient parameters from drogue data (Molinari and Kirwan (1975), Okubo and Ebbesmeyer (1976)).

These new methods provide a comprehensive framework in which we reanalyse this valuable set of drogue data. We will first investigate gross-scale drogue groups to determine Lagrangian deformations and higher-order turbulent displacements. This leads to further evaluations of the velocity gradient parameters, momentary eddy diffusivities, among others. Relations of the velocity gradient parameters to other dispersion characteristics such as drogue area will also be studied.

Ebbesmeyer, Okubo, Helseth and Robbins (1976) have extended Okubo's (1966) method for solving a general equation of time-dependent advection and diffusion. Lagrangian formulation enables us to solve the generalized equation analytically. Values of the Lagrangian deformations and momentary eddy diffusivities thus determined are used to evaluate the pattern of dispersion.

Within gross-scale drogue groups are found several sub-groups, i.e. clusters. Smaller-scale variability of velocity gradients and turbulence characteristics will be examined and compared with those of the gross scale.

# CHAPTER 2
# DATA FOR ANALYSIS: EDITING AND SMOOTHING

The following is general information on the experimental runs in the Great Lakes drogue studies. Fifty to ninety drogues were released in each of six experiments at depths of 5 ft (1.5 m) and 20 ft (6.1 m). On 25 and 26 June 1964, two studies were made in Lake Michigan about 1.5 miles WNW of the Indiana Harbor East Breakwater Light. On 15 and 16 July, two studies were conducted in Lake Erie about 5 miles WSW of Colchester, Ontario (July 16 runs have never been processed). Finally, on 15 and 16 August, two more studies were made in Lake Erie about 5.3 miles west of the Cleveland West Pierhead Light, Ohio.

The position of each drogue was determined at 5-10 minute intervals during a total duration of 4-6 hours for each experiment. The accuracy of each drogue position was estimated at ±2 m. The drogue position was finally transformed by a computer program into an absolute (x,y) coordinate system such that the x-axis pointed to the east, the y-axis to the north, and the origin of the system was taken at a central part of the studied area. The complete set of data was registered in punch cards which were available for this reanalysis.

Our close examination of these drogue data revealed that drogue trajectories showed erratic behavior. These errors are of two types: (i) those associated with an individual drogue, and (ii) those showing coherence among a sub-group of drogues. Errors of (i) were usually due to keypunching errors in the original raw data, while errors of (ii) were due to improper positioning of reference buoys.

Reference buoys were anchored in the field and used as fixed markers on aerial photographs to determine individual drogue positions. In practice several overlapping photographs of a drogue group were usually required. Each photograph contained several of the overall set of reference buoys. From knowledge of the overall pattern of reference buoys, the individual photographs could be placed together to form a complete picture of the entire drogue group. Thus if a reference buoy is improperly positioned it will affect the positions of many drogues.

To edit errors due to reference buoys we computed ratios of distances between each pair of reference buoys on the photographs. Since these buoys are fixed, these ratios should remain invariant between successive photographs taken several seconds apart (i.e., airplane elevation should not change significantly within several seconds). Comparing these ratios with those obtained from one high-altitude photograph of all reference buoys, we determined which reference buoys were mispositioned and corrected many of their actual positions. However, many other minor errors apparently remained which we were unable to correct without a complete re-examination of the original photographs--a task beyond the scope of this study.

To minimize these remaining minor and uncorrectable errors (estimated at ±5 m), we smoothed individual drogue trajectories by fitting both x and y as functions of time with third order polynomials in the least squares sense. Smoothed positions were then computed from these fits at 0.2 hour intervals ("Smoothed data"). In the following analysis we will use the smoothed data for calculation.

# CHAPTER 3
# ANALYSIS OF GROSS SCALE DROGUE GROUPS

The gross scale drogue group is composed of all the drogues observed continuously throughout a particular experiment. Drogues tracked intermittently have been deleted from our computations.

## 3.1 *Drogue area, elongation and mean orientation of principal axes of dispersion*

Smoothed positions of each drogue thus obtained after editing are referred to the north-east coordinate system. From these smoothed data we then compute the mean orientation of the "principal axes of dispersion."

The principal axes of dispersion are defined at any time as the major and minor axes along which the variance of drogue position is maximum and minimum, respectively. These axes may be thought of as the mutually perpendicular major and minor axes of an ellipse. Then we make the following definitions:

(a) Drogue area $A \equiv 4\pi\sigma_X\sigma_Y$ .

(b) Elongation $\varepsilon \equiv \sigma_X/\sigma_Y$ .

(c) Mean orientation of principal axes of diffusion, $\overline{\theta}$:

$$\overline{\theta} \equiv \frac{1}{n+1} \sum_{i=1}^{n+1} \theta_i$$

where $\sigma_X, \sigma_Y$ are standard deviations of drogue position along the major and minor axes, respectively; $\theta_i$ is the angular deviation of the minor axis from true north at the ith time; and n is the number of 0.2 hour intervals.

We then rotated all drogue positions in each experiment by a constant $\overline{\theta}$ . Figure 1 shows the major and minor axes for each experiment and their orientation relative to the orientation of the original raw data. Table 1 contains general information on the reanalysis of the Great Lakes Drogue Studies data for each of the eight experiments. Inspection of Table 1 and Figure 1 shows the following:

(i) An average of 50 drogues were

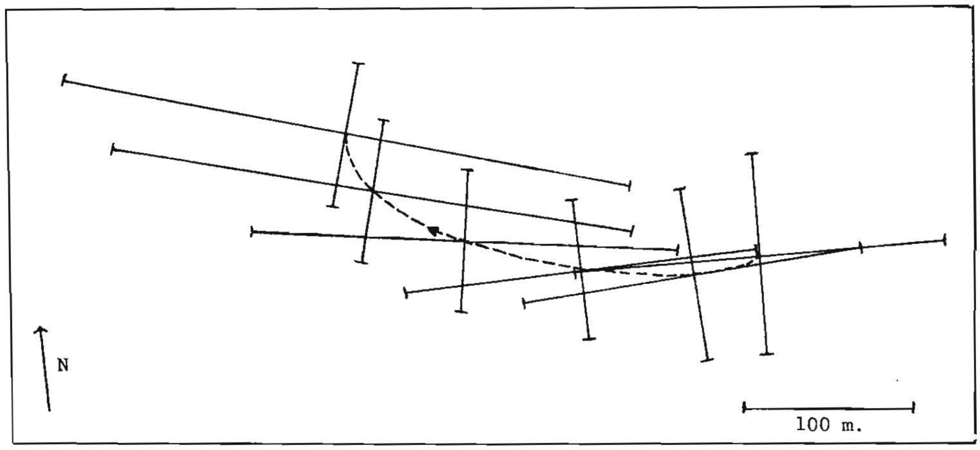


Figure 1a. Centroid trajectory and principal axes of diffusion for experiment 120. Principal axes measure one standard deviation.

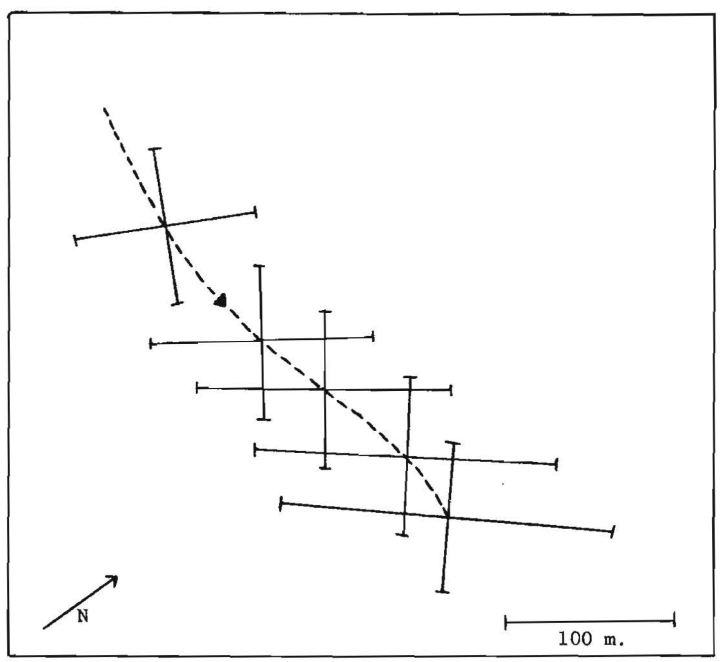


Figure 1b. Centroid trajectory and principal axes of diffusion for experiment 205. Principal axes measure one standard deviation.

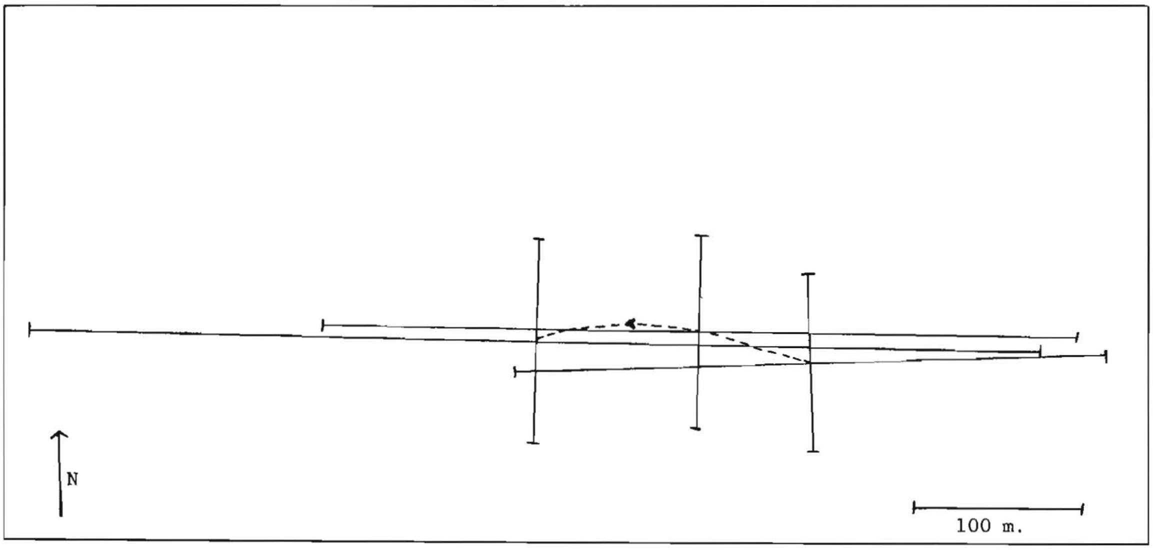


Figure 1c. Centroid trajectory and principal axes of diffusion for experiment 220. Principal axes measure one standard deviation.

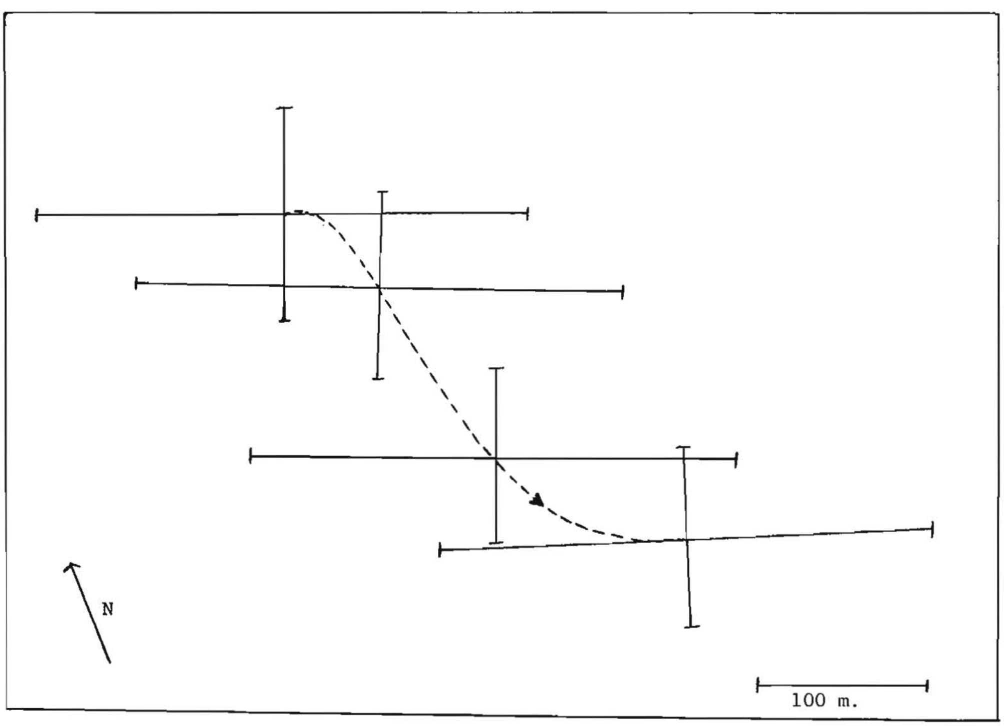


Figure 1d. Centroid trajectory and principal axes of diffusion for experiment 305. Principal axes measure one standard deviation.

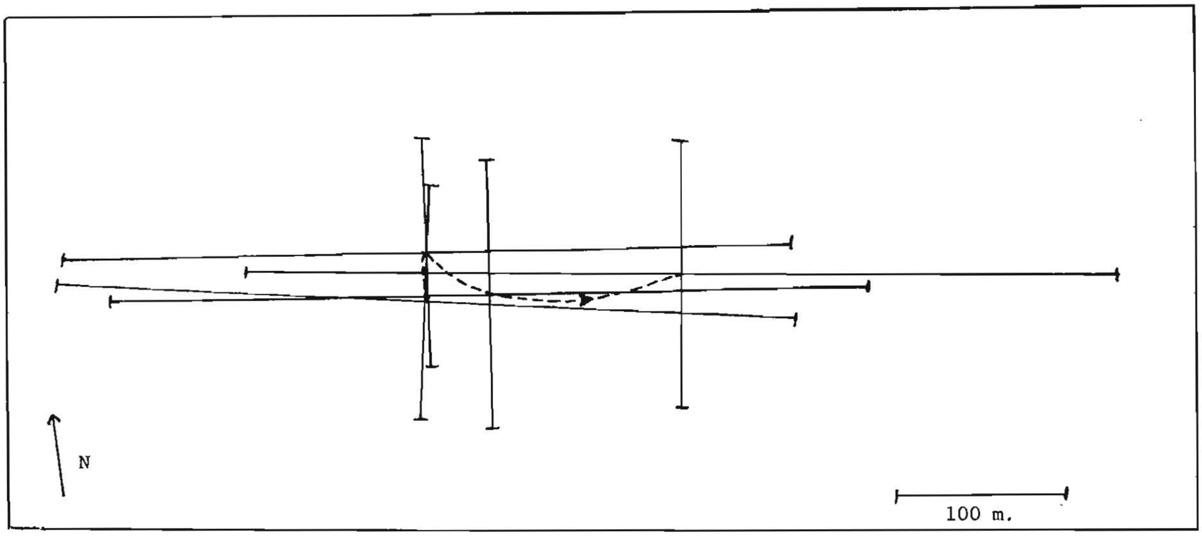


Figure 1e. Centroid trajectory and principal axes of diffusion for experiment 320. Principal axes measure one standard deviation.

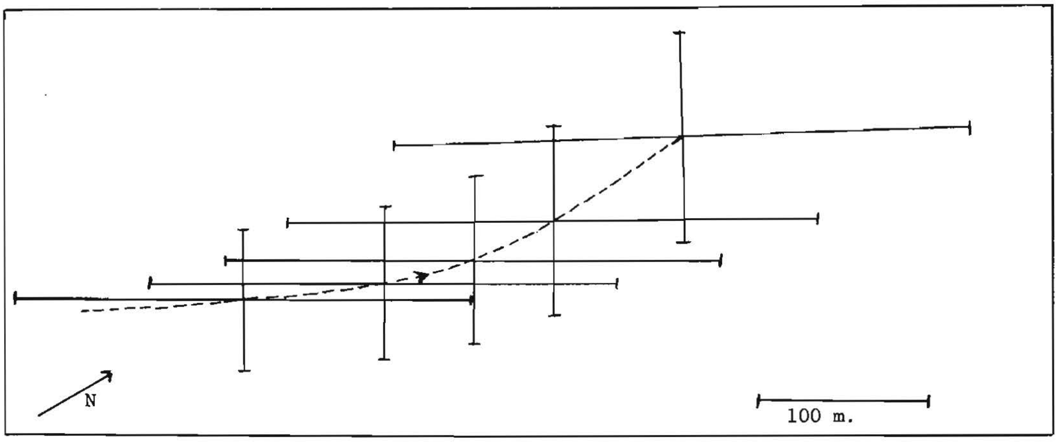


Figure 1f. Centroid trajectory and principal axes of diffusion for experiment 520. Principal axes measure one standard deviation.

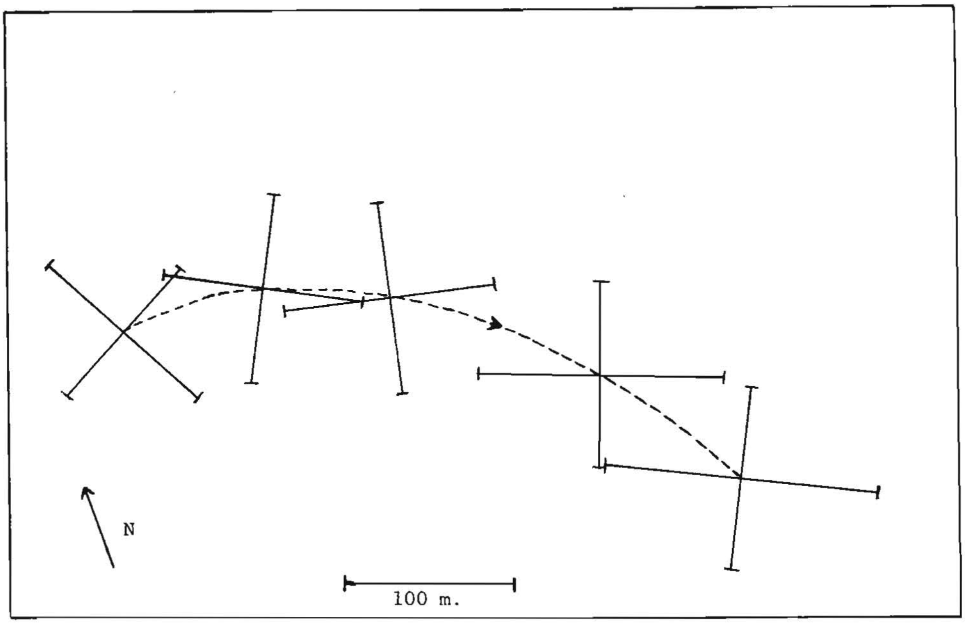


Figure 1g. Centroid trajectory and principal axes of diffusion for experiment 605. Principal axes measure one standard deviation.

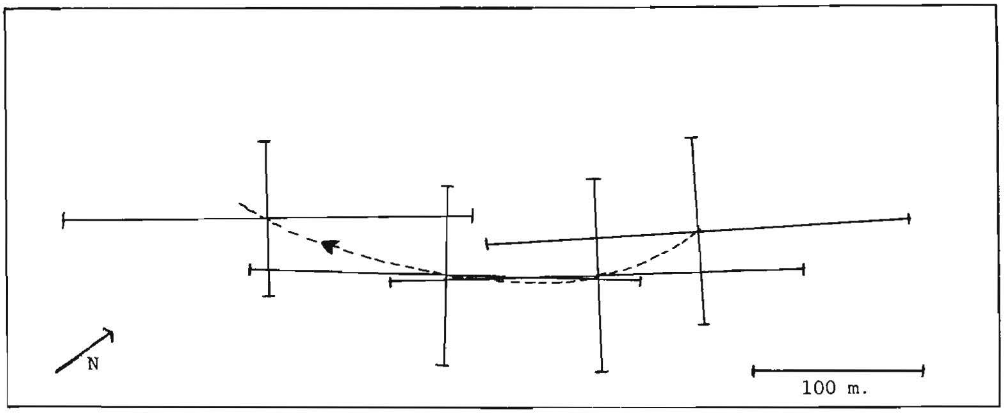


Figure 1h. Centroid trajectory and principal axes of diffusion for experiment 620. Principal axes measure one standard deviation.

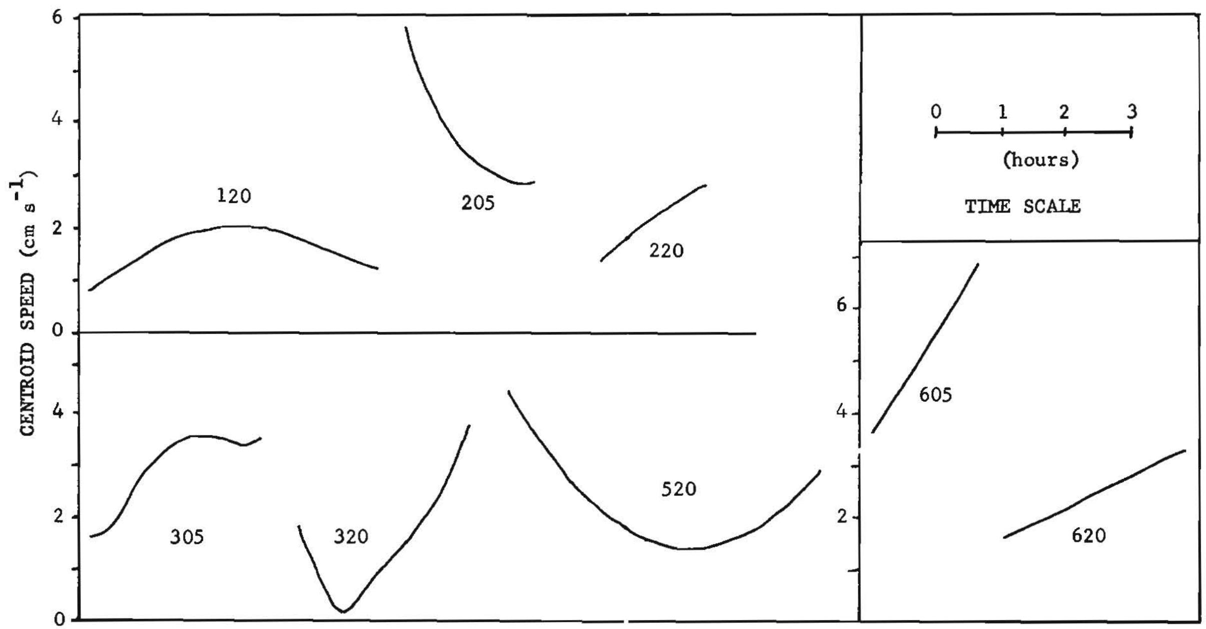


Figure 11. Centroid speed versus time for each experiment.

Table 1. General information on Great Lakes Drogue Studies[a].

| Experiment designation[b] | 1<br>Date | 2<br>Location | 3<br>Duration of Experiment (EST) | 4<br>No. of drogues | 5<br>Water depth (m) | 6<br>Drogue depth (m) | 7<br>$\frac{(6)}{(5)}$ | 8<br>Initial drogue area ($10^3$ $m^2/4$) | 9<br>Final drogue area/8 ($A/A_0$) |
|---|---|---|---|---|---|---|---|---|---|
| 120 | 6/25/64 | L. Michigan | 11:45-16:46 | 44 | 8.1 | 6.1 | .75 | 6.49 | 1.11 |
| 205 | 6/26/64 | " | 11:43-15:30 | 32 | 8.1 | 1.5 | .19 | 2.36 | 1.80 |
| 220 | " | " | " | 55 | 8.1 | 6.1 | .75 | 9.18 | 1.81 |
| 305 | 7/15/64 | 1. Erie | 12:25-15:45 | 56 | 7.5 | 1.5 | .20 | 9.09 | .836 |
| 320 | " | " | " | 54 | 7.5 | 6.1 | .81 | 15.3 | 1.22 |
| 520 | 8/15/64 | " | 11:14-16:50 | 74 | 12.6 | 6.1 | .48 | 5.91 | 1.71 |
| 605 | " | " | 12:27-16:20 | 28 | 12.6 | 1.5 | .12 | 6.50 | 1.41 |
| 620 | " | " | " | 57 | 12.6 | 6.1 | .48 | 6.87 | .813 |

[a] See text for definitions.
[b] e.g.; 120 experiment 1 at 20 foot drogue depth.

Table 1. Cont'd

| Experiment designation | 10<br>Initial minor axis ($10^2$ m) | 11<br>Initial major axis ($10^2$ m) | 12<br>Initial elongation | 13<br>Final elongation | 14<br>Wind speed ($cm^2$ $s^{-1}$) | 15<br>Centroid speed ($cm^2$ $s^{-1}$) | 16<br>Wind factor (%) |
|---|---|---|---|---|---|---|---|
| 120 | 5.92 | 1.10 | 1.86 | 3.88 | 400 | 1.62 | .4 |
| 205 | .453 | .521 | 1.09 | 2.07 | 420 | 3.76 | .9 |
| 220 | .528 | 1.74 | 3.39 | 4.65 | 420 | 2.19 | .5 |
| 305 | .628 | 1.45 | 2.35 | 2.74 | 380 | 2.96 | .8 |
| 320 | .703 | 2.17 | 3.15 | 3.05 | 380 | 1.55 | .4 |
| 520 | .427 | 1.39 | 3.25 | 2.76 | 320 | 2.28 | .7 |
| 605 | .556 | 1.17 | 1.10 | 1.40 | 360 | 5.30 | 1.5 |
| 620 | .553 | 1.24 | 2.22 | 2.46 | 360 | 2.41 | .7 |

continuously tracked during each experiment.

(ii) Orientation of the principal axes of diffusion remained nearly constant during most experiments.

(iii) In experiments 305 and 620 initial drogue area exceeded final drogue area.

(iv) In experiments 320 and 520 initial elongation exceeded final elongation.

(v) Centroid speeds were relatively low, ranging between 1 and 6 cm $s^{-1}$.

### 3.2 *Lagrangian deformations*

Given a set of drogue positions it is natural to study dispersion using the Lagrangian diffusion equation (Corrsin, 1962). Inspection of that equation shows that, to first order, it has a general analytic solution expressed in terms of Lagrangian deformations (Okubo, 1966). Yet those deformations have not previously been determined from field observations. Okubo, Ebbesmeyer and Helseth (1976) for the first time developed a method to determine Lagrangian deformations from analysis of current followers.

The method is outlined as follows. Given n drogues observed simultaneous at m times, we consider the present $x_i$, $y_i$ drogue coordinates as functions of time t in k increments, and their Lagrangian coordinate $a_i$, $b_i$ using the following notation:

$$x_i = x_i\ (a_i, b_i, k) \qquad i = 1, 2, \cdots, n$$

$$y_i = y_i\ (a_i, b_i, k) \qquad k = 1, 2, \cdots, m$$

Next we expand the $x_i$, $y_i$ coordinates of each drogue with respect to $a_i$, $b_i$ about the centroid $\bar{a}$, $\bar{b}$ :

$$\begin{aligned} x_i\ (a_i, b_i, k) = x\ (\bar{a}, \bar{b}, k) &+ e_{11}(k)(a_i-\bar{a}) \\ &+ e_{12}(k)(b_i-\bar{b}) \\ &+ x_i''\ (a_i, b_i, k) \\ y_i\ (a_i, b_i, k) = y\ (\bar{a}, \bar{b}, k) &+ e_{21}(k)(a_i-\bar{a}) \\ &+ e_{22}(k)(b_i-\bar{b}) \\ &+ y_i''\ (a_i, b_i, k) \end{aligned} \qquad (1)$$

where $x\ (\bar{a}, \bar{b}, k)$, $y\ (\bar{a}, \bar{b}, k)$ are the x, y coordinates of a drogue starting at $\bar{a}$, $\bar{b}$; $e_{11}(k) \equiv (\partial x/\partial a)_0$, $e_{12}(k) \equiv (\partial x/\partial b)_0$, $e_{21}(k) \equiv (\partial y/\partial a)_0$, $e_{22}(k) \equiv (\partial y/\partial b)_0$ are Lagrangian first order deformations evaluated at $\bar{a}$, $\bar{b}$ and depend only on time; and $x_i''$, $y_i''$ are second and higher order displacements.

Lagrangian coordinates (a, b) may be taken either as the initial positions of drogues at time k=1, or as the positions of drogues at any previous time k=j.

In the expansions of eq. (1) we have assumed that Lagrangian first order deformations are uniform within the drogue group. This formulation views the lake turbulence spectrum as separable into two major parts according to drogue group size: larger-scale eddies produce first order deformations whereas smaller-scale eddies produce higher order displacements. Thus as the drogue group spreads, the division between the part of the eddy spectrum assignable to first order deformations and higher order displacements tends toward smaller wave numbers and frequencies.

From eq. (1) Lagrangian deformations may be computed following the linear regression procedures of Okubo, Ebbesmeyer and Helseth (1976), henceforth abbreviated

OEH. Furthermore the OEH method enables us to compute parameters of mean velocity gradients directly from Lagrangian deformations. These parameters are divergence, relative vorticity, and deformation rates.

Before applying these procedures to all experiments, several exploratory computations with Experiment 520 were made to answer the following questions:

(i) What are the effects of smoothing drogue positions on computations of Lagrangian deformations?

(ii) What is the effect of varying the order of the polynomial fit on computations of Lagrangian deformations?

(iii) Does the Lagrangian approach of the OEH produce identical results to Okubo and Ebbesmeyer's (1976), henceforth abbreviated OE, in determining velocity gradients?

In order to answer the first two of these questions we first computed momentarily deformations $e^*_{ij}$ (see OEH) using both raw and smooth positions. Raw positions were linearly interpolated at 0.2 hour intervals. Smooth positions were obtained using both third and fourth order polynomials. To answer the third question we computed $g_{ij}$ using both OEH and OE from fourth order polynomial fits:

$$g_{11} \equiv ({}^{\partial u}/\partial x)_0, \; g_{12} \equiv ({}^{\partial u}/\partial y)_0,$$

$$g_{21} \equiv ({}^{\partial v}/\partial x)_0, \; g_{22} \equiv ({}^{\partial v}/\partial y)_0.$$

The results shown in Figure 2 lead to the following answers:

(i) Smoothing drogue positions corresponds to smoothing $e^*_{ij}$, i.e., $e^*_{ij}$ computed from smooth positions appear as smooth curves centered within ragged curves computed from unsmooth positions. Note that the ragged curves often exceed the 95% confidence limits from smooth positions.

(ii) Varying the polynomial degree within reasonable limits changes $e^*_{ij}$ by small amounts compared with the raggedness noted in (i) and the 95% confidence limits.

(iii) OEH and OE methods produce current shears differing by small amounts compared with the raggedness associated with raw data and the 95% confidence limits. We conclude that a third order polynomial fit provides a satisfactory degree of smoothing.

Lagrangian deformations were then computed for all experiments using the OEH procedure and third order smoothing. Figure 3 shows the time series of each component Lagrangian deformation and corresponding 95% confidence limits. These deformations were then used to compute divergence, vorticity, and deformation rates.

### 3.3 *Velocity gradient parameters, i.e. divergence, relative vorticity, and deformation rates*

Velocity gradients are of special interest to physical limnologists. First, velocity gradients have elementary kinematic interpretations of the differential motion of parcels of water. Second, they are conventionally used as characteristic indicators of the fluxes of momentum in combination with eddy viscosities. Thus knowledge of these gradients can be useful in studying the dynamics of lake currents and frontal zones (Kirwan, 1975).

Time series of horizontal divergence $\gamma$, relative vorticity $\eta$, stretching deformation rate $\alpha$, and shearing deformation rate h were computed directly from Lagrangian deformations $e^*_{ij}$ following the OEH procedure. Since that procedure produces results nearly identical with the OE procedure (as shown in the previous section), the OEH procedure is preferred since *both* Lagrangian deformations and current characteristics may be obtained at once rather than only current characteristics in the OE procedure.

Figure 4 shows time series of $\gamma$, $\eta$, $\alpha$, h and their 95% confidence limits for each experiment. Shown also are histograms for

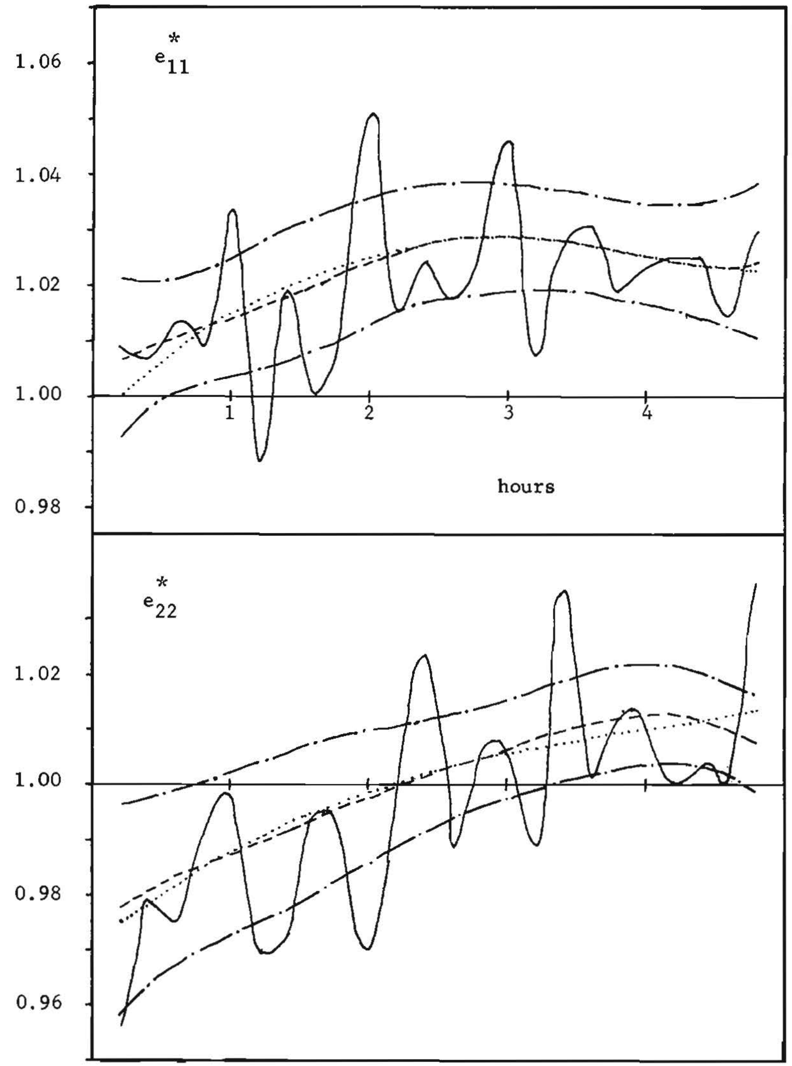


Figure 2a1. Lagrangian deformations $e^*_{11}$ and $e^*_{22}$ versus time for experiment 520 computed using OEH method from: —— raw data; ...... third order polynomial fit; ---- fourth order polynomial fit. The lines —·— are 95% confidence limits computed from the fourth order polynomial fit. Note that for these comparisons, positions were referenced to true north instead of in the frame of mean principal axes of diffusion.

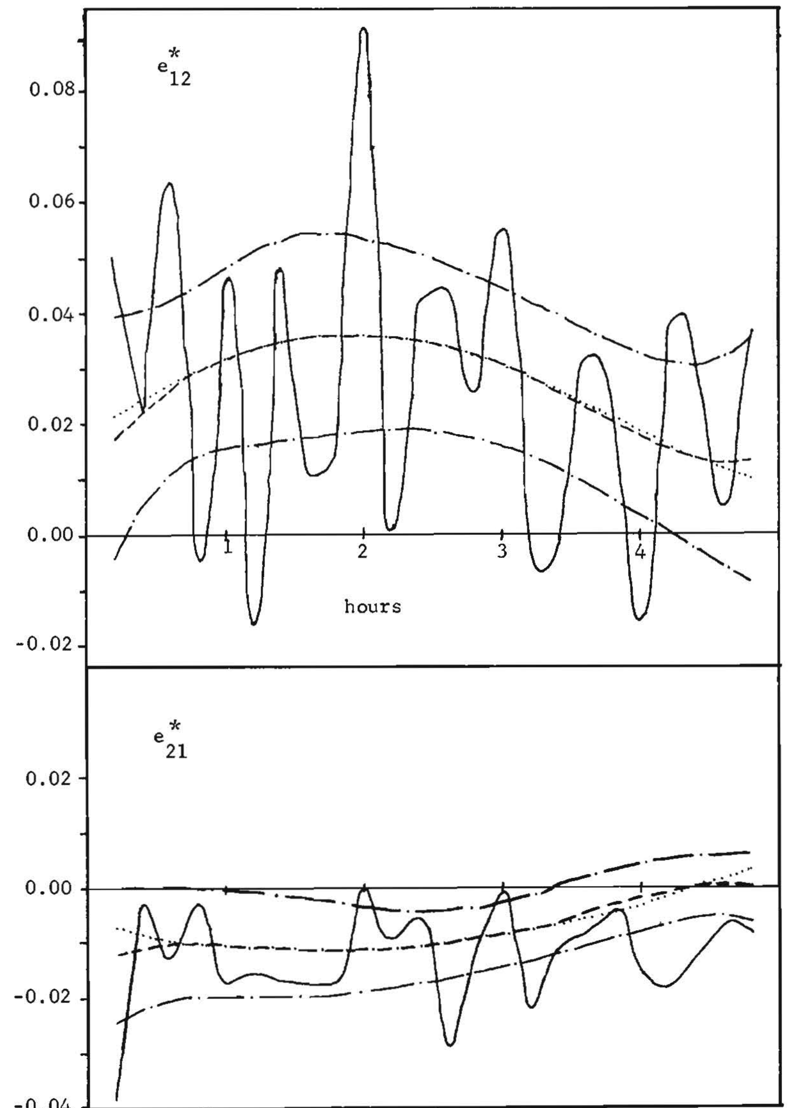


Figure 2a2. Lagrangian deformations $e^*_{12}$ and $e^*_{21}$ versus time for experiment 520 computed using OEH method from: —— raw data; ...... third order polynomial fit; ---- fourth order polynomial fit. The lines —·— are 95% confidence limits computed from the fourth order polynomial fit. Note that for these comparisons, positions were referenced to true north instead of in the frame of mean principal axes of diffusion.

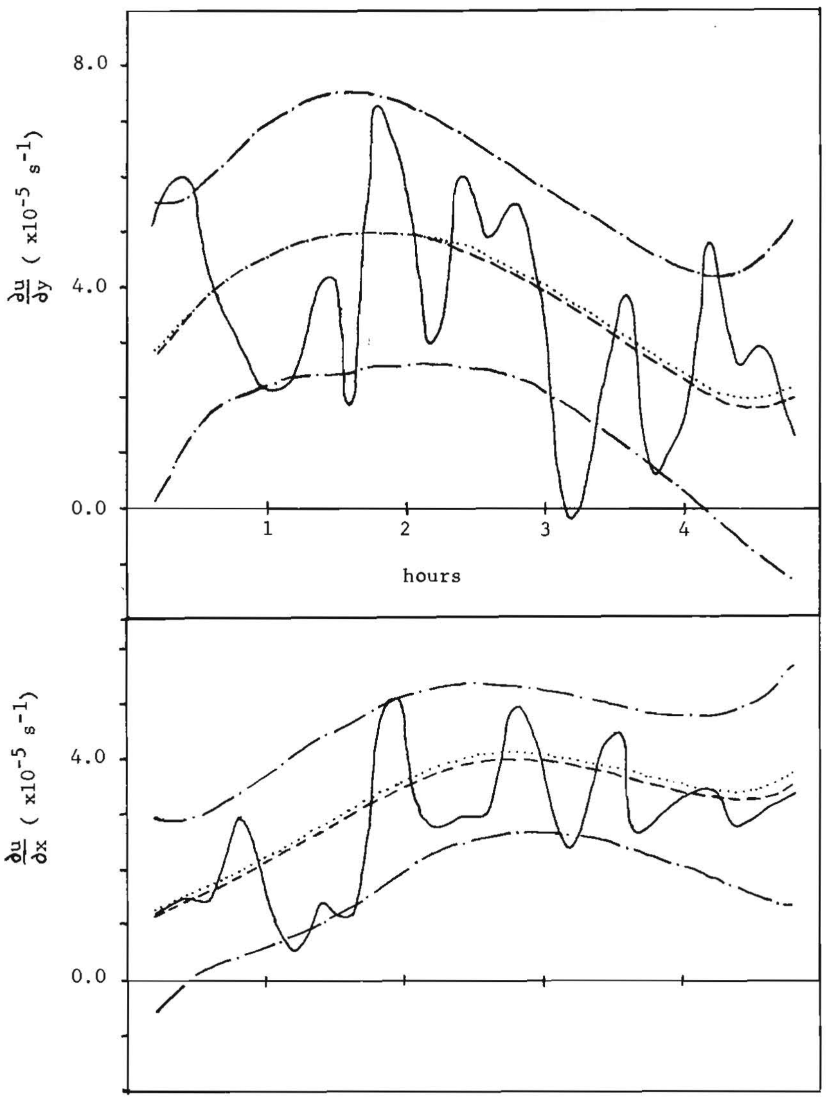


Figure 2b1. $\partial u/\partial y$ and $\partial u/\partial x$ versus time for experiment 520 computed from: —— unsmoothed positions using OEH method; ........ from fourth order polynomial fit using OE method; - - - from fourth order polynomial fit using OEH method. The lines —·— are 95% confidence limits computed by OE method from fourth order polynomial fit. Note that for these comparisons, positions were referenced to true north instead of in the frame of mean principal axes of diffusion.

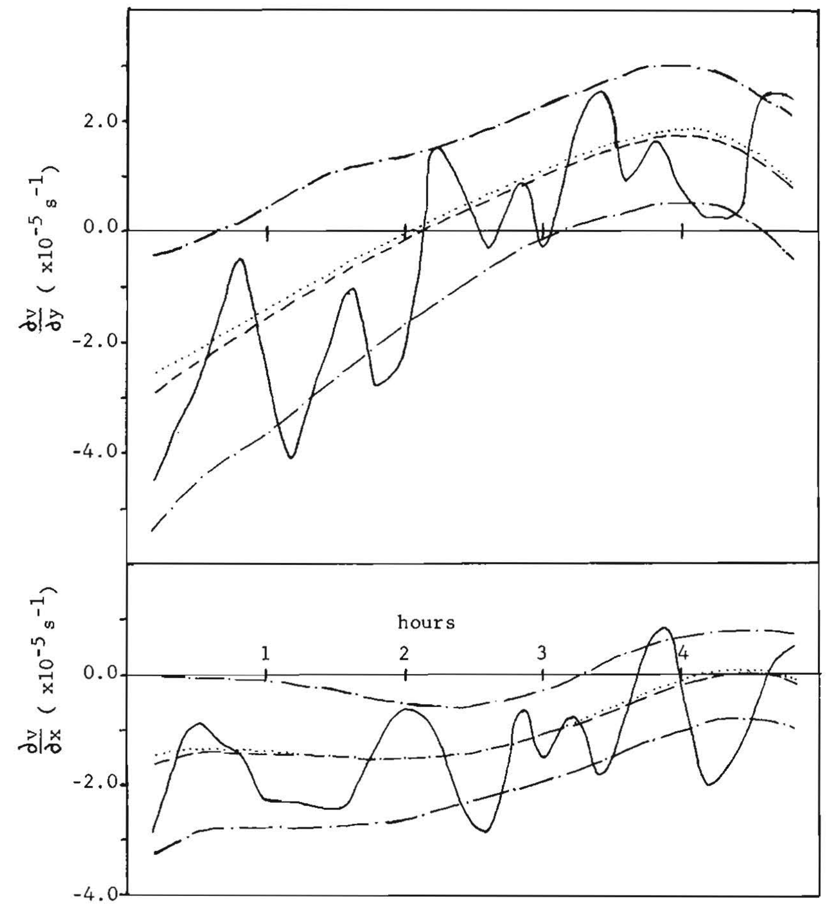


Figure 2b2. $\partial v/\partial y$ and $\partial v/\partial x$ versus time for experiment 520 computed from: —— unsmoothed positions using OEH method; ........ from fourth order polynomial fit using OE method; - - - from fourth order polynomial fit using OEH method. The lines —·— are 95% confidence limits computed from OE method from fourth order polynomial fit. Note that for these comparisons, positions were referenced to true north instead of in the frame of mean principal axes of diffusion.

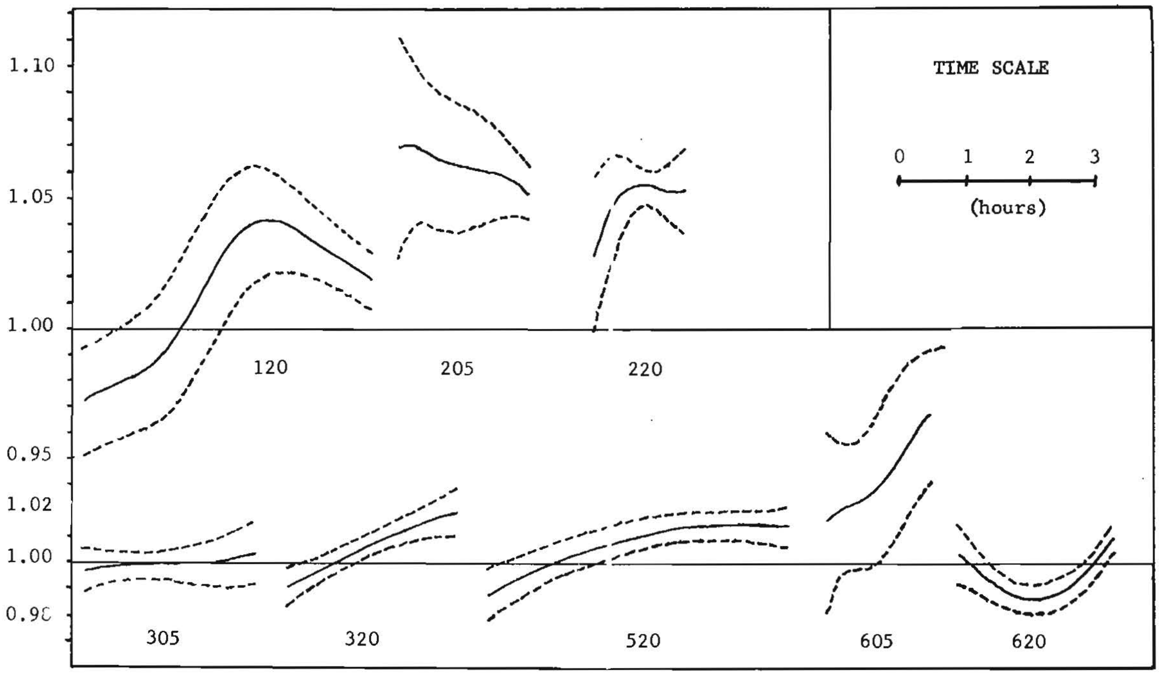


Figure 3a. Time series of Lagrangian deformation $e_{11}^*$ (solid lines) and 95% confidence limits (dashed lines) for each experiment.

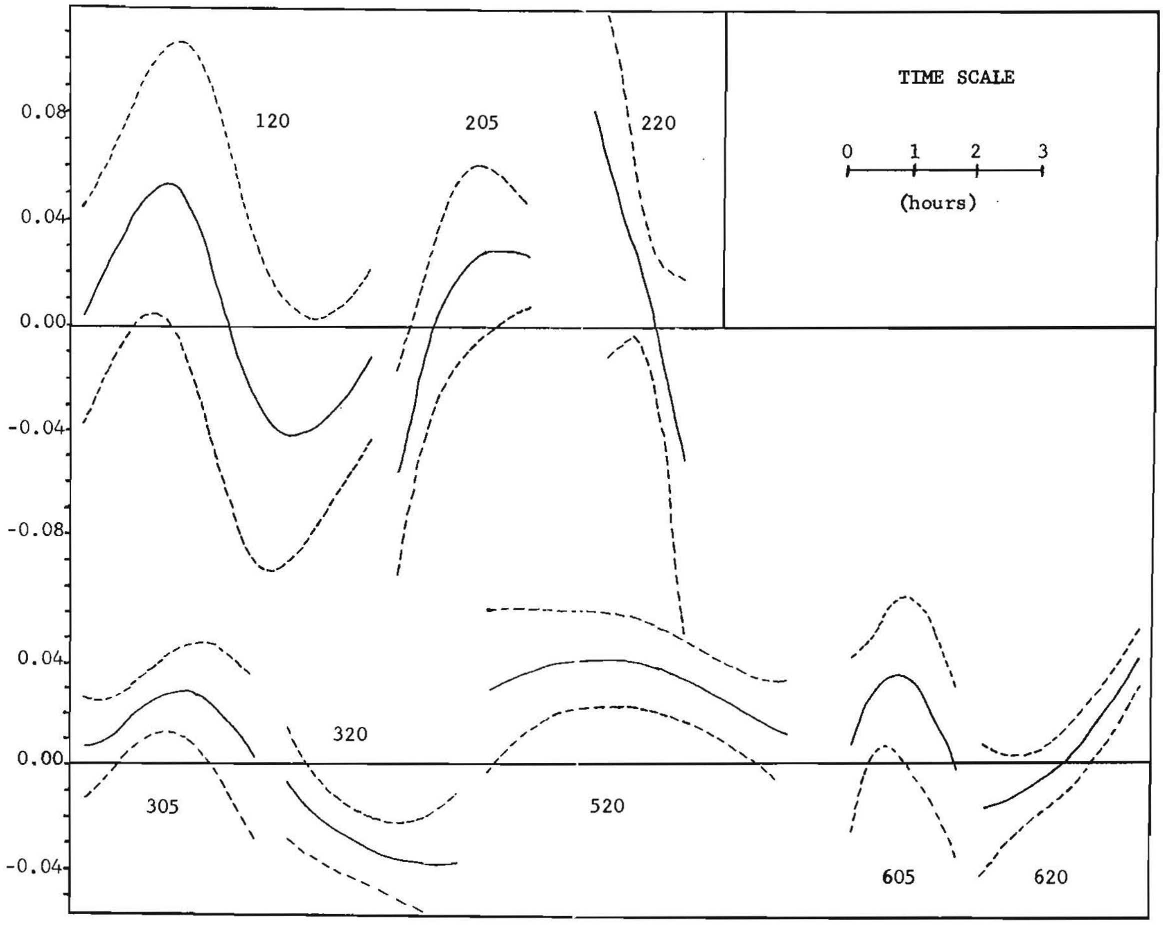


Figure 3b. Time series of Lagrangian deformation $e_{12}^*$ (solid lines) and 95% confidence limits (dashed lines) for each experiment.

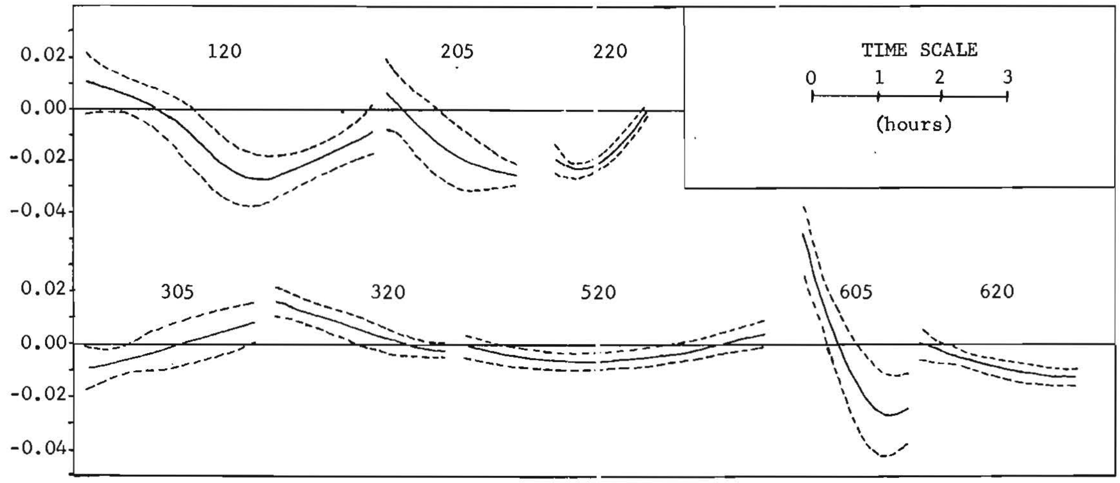


Figure 3c. Time series of Lagrangian deformation $e^{*}_{21}$ (solid lines) and 95% confidence limits (dashed lines) for each experiment.

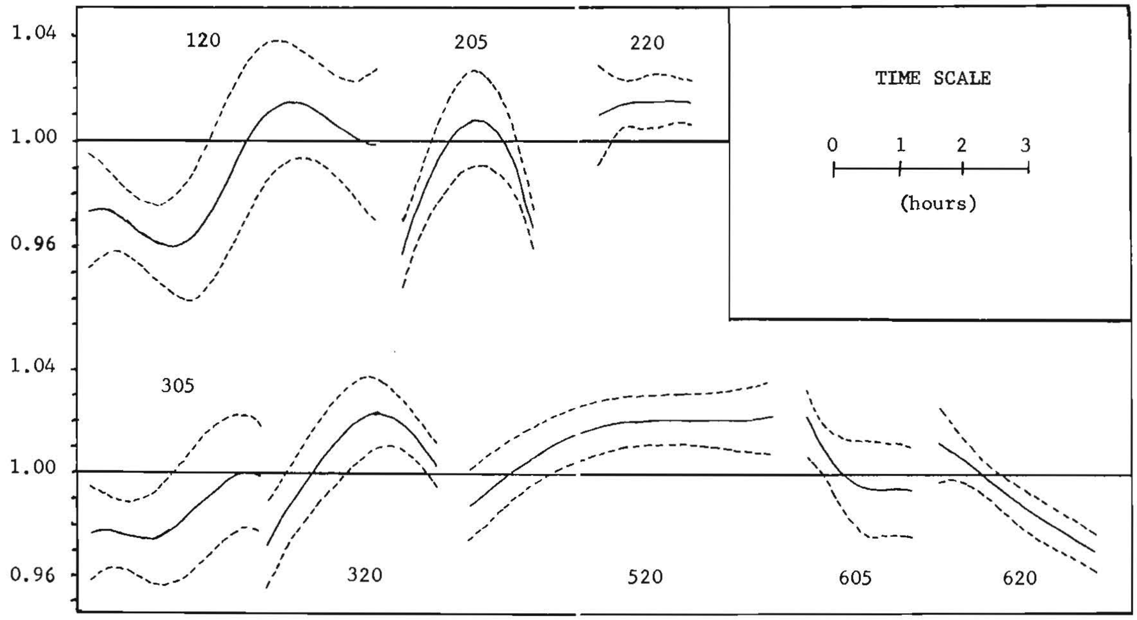


Figure 3d. Time series of Lagrangian deformation $e^{*}_{22}$ (solid lines) and 95% confidence limits (dashed lines) for each experiment.

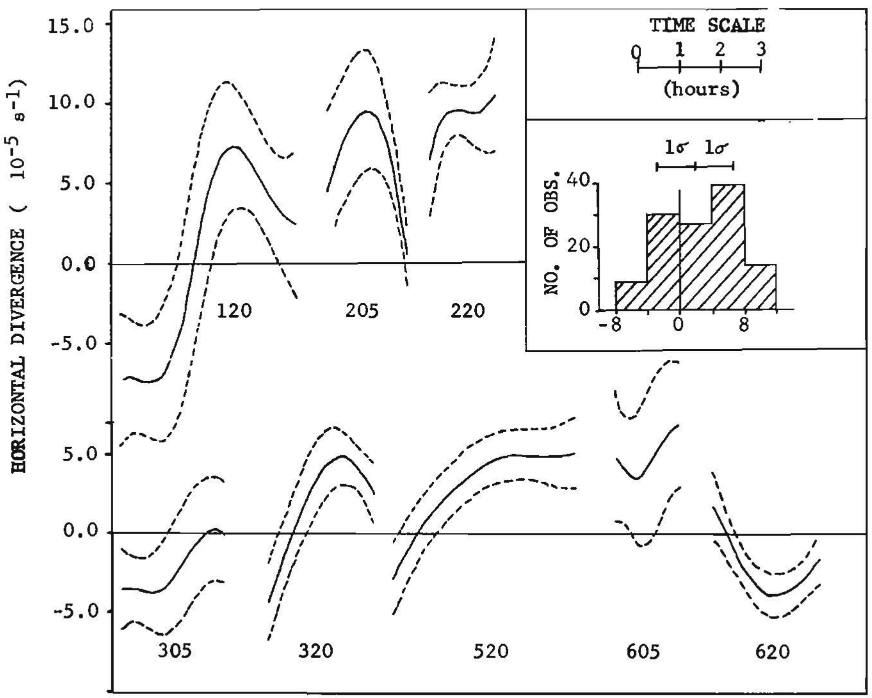


**Figure 4a.** Time series of horizontal divergence (solid line) and 95% confidence limits (dashed lines). Insert shows histogram of values (118) from all experiments.

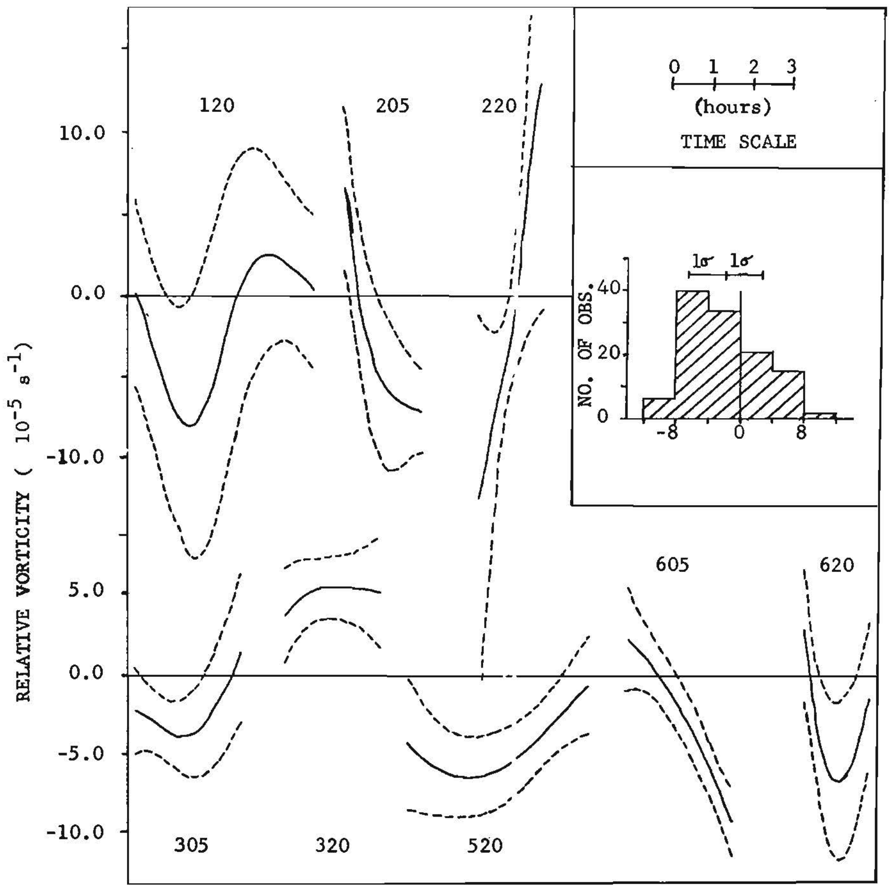


**Figure 4b.** Time series of relative vorticity (solid lines) and 95% confidence limits (dashed lines). Insert shows histogram of values (118) from all experiments.

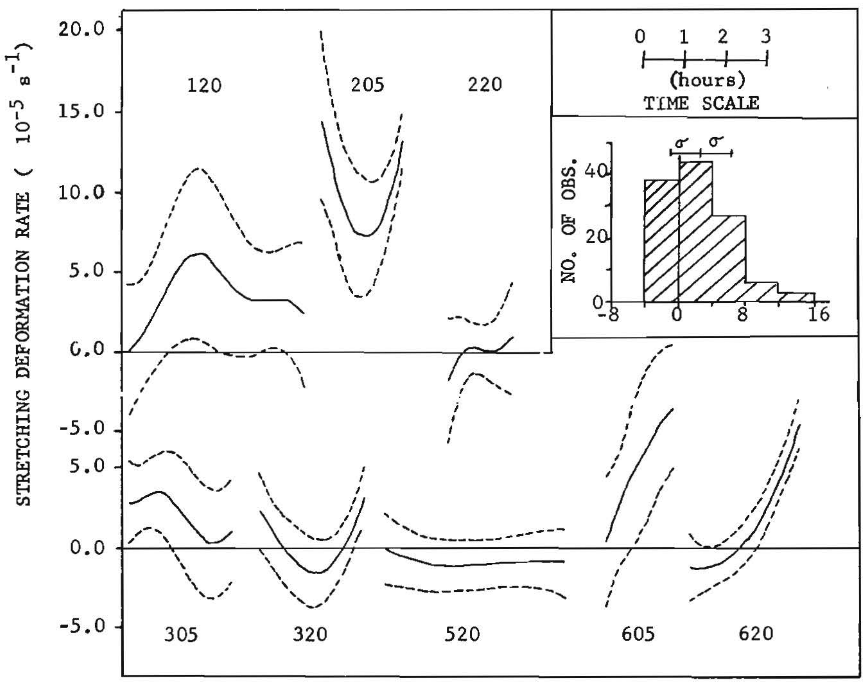


Figure 4c. Time series of stretching deformation rate (solid lines) and 95% confidence limits (dashed lines). Insert shows histogram of values (118) from all experiments.

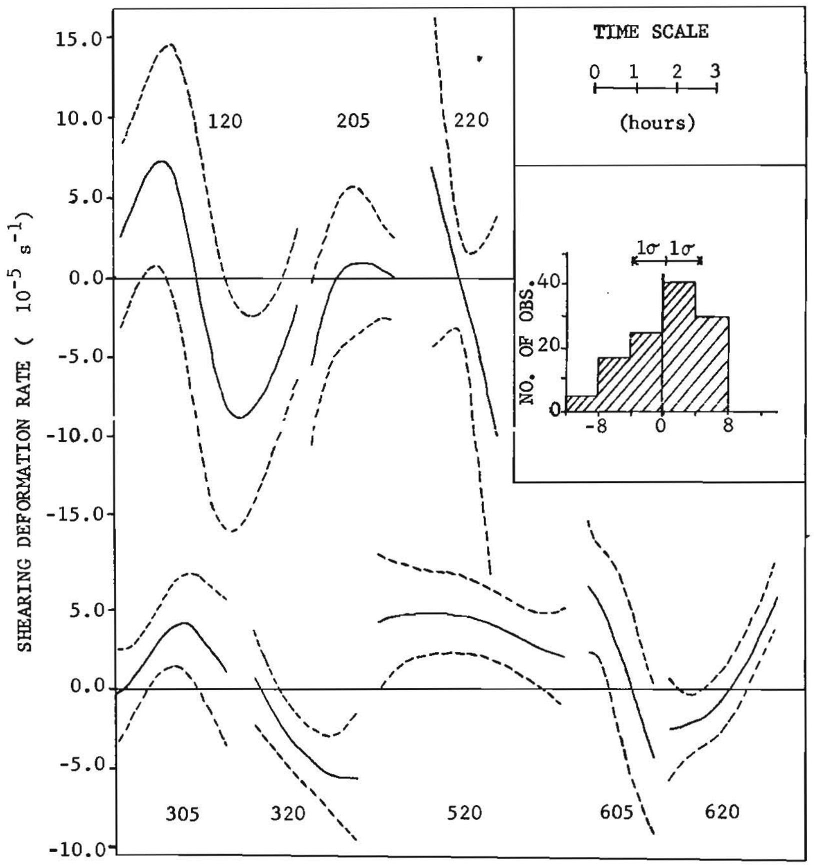


Figure 4d. Time series of shearing deformation rate (solid lines) and 95% confidence limits (dashed lines). Insert shows histogram of values (118) from all experiments.

the combination of all experiments, i.e., 118 values of each current property sorted according to 4 x $10^{-5}$ $s^{-1}$ class intervals. Finally Table 2 shows mean values for each experiment and for all experiments taken as a whole, i.e., the mean of the 118 values used in the histograms.

Inspection of Figure 4 and Table 2 reveals the following:

(i) No apparent pattern to temporal variations. However the histograms qualitatively appear skewed Gaussian. Shearing deformation rate and relative vorticity histograms are skewed in opposite directions. Mean horizontal divergence is positive in a distribution containing 33% negative values. Mean stretching deformation rate is positive accounting for the elongation in most experiments.

(ii) 95% confidence limits usually exceed standard deviation by average factors of 1.4 to 2.3.

(iii) The following close approximations can be used to deduce deformations from current shear obtained from current meters:

$$\frac{\partial u}{\partial x} \approx \dot{e}^{*}_{11} \qquad \frac{\partial v}{\partial x} \approx \dot{e}^{*}_{21}$$

$$\frac{\partial u}{\partial y} \approx \dot{e}^{*}_{12} \qquad \frac{\partial v}{\partial y} \approx \dot{e}^{*}_{22} \qquad (2)$$

These approximations result from the fact that $e^{*}_{11}$ and $e^{*}_{22} \approx 1$, whereas $e^{*}_{21}$ and $e^{*}_{12} \approx 10^{-2} - 10^{-3}$.

### 3.4 *Further relations of* $\gamma$, $\eta$, $\alpha$, h

In addition to time series, histograms and mean values of divergence, vorticity and deformation rates given in Section 3.3, the following descriptions prove useful for understanding diffusive patterns: (a) normalized drogue area versus integrated divergence; (b) simple vorticity balance; (c) singularity diagrams; (d) comparison of Ebbesmeyer's (1975) method of computing $\partial u/\partial y$ (henceforth called the Eb method) with $\partial u/\partial y$ computed from the OEH procedure.

(a) Normalized drogue area versus integrated divergence

Drogue area is approximately related to horizontal divergence by

$$\gamma = \frac{1}{A}\frac{dA}{dt}$$

so that

$$\frac{A}{A_0} \equiv \frac{A(t)}{A(t=0)} = \exp\left[\int_0^t \gamma(t')dt'\right] \qquad (3)$$

where A/A (t = 0) will be referred to as normalized drogue area, and the integral will be referred to as the integrated divergence. Note that $A/A_0$ is also a dilution factor.

If we associate A with a vertical cylinder of water having unit volume and height D, then for this volume to be conserved $D \propto A^{-1}$, or

$$D = \exp -\left[\int_0^t \gamma(t')dt'\right] \qquad (4)$$

In practice it is easier to evaluate integrated divergence as $\prod_{i=1}^{n} J^{*}_{i}$ .

Figure 5 shows time series of normalized drogue area versus integrated divergence for each experiment. These curves show that divergence controls drogue area to a great extent. In this approach to diffusion the area characterizes effluent dispersion due to larger scale eddies. Since these are primarily responsible for spreading of a patch, horizontal divergence explains most of the area growth of a patch.

(b) Simple vorticity balance

The vertical component of the absolute vorticity ($\eta$ + f) obeys the following

Table 2. Mean divergence, vorticity, and deformation rates with standard deviations and mean 95% confidence intervals.

| Experiment designation | Horizontal divergence ($10^{-5}$ $s^{-1}$) | | | | Relative vorticity ($10^{-5}$ $s^{-1}$) | | | |
|---|---|---|---|---|---|---|---|---|
| | mean | | ± 95% | ± 95% | mean | | ± 95% | ± 95% |
| 120 | .169 | 5.81 | 4.10 | 0.706 | -1.88 | 3.85 | 6.69 | 1.74 |
| 205 | 6.78 | 2.79 | 3.37 | 1.21 | -3.38 | 4.70 | 4.15 | 0.883 |
| 220 | 9.14 | 1.03 | 2.45 | 2.38 | -1.29 | 8.84 | 7.75 | 0.887 |
| 305 | -2.10 | 1.64 | 2.91 | 1.77 | -2.35 | 1.64 | 2.94 | 1.79 |
| 320 | 2.03 | 2.92 | 1.97 | 0.675 | 5.02 | .498 | 2.49 | 5.00 |
| 520 | 3.09 | 2.41 | 1.74 | 0.722 | -4.67 | 1.80 | 2.69 | 1.49 |
| 605 | 4.98 | 1.29 | 4.17 | 3.23 | -3.68 | 3.10 | 4.51 | 1.46 |
| 620 | -2.21 | 1.79 | 1.40 | 0.782 | -2.74 | 3.82 | 2.00 | 0.524 |
| mean of all experiment | 2.74 | 2.46 | 2.76 | 1.43 | -1.87 | 3.53 | 4.15 | 1.72 |
| mean of all values | 2.10 | 4.66 | | | -2.02 | 4.60 | | |

Table 2. Cont'd.

| Experiment designation | Stretching deformation rate ($10^{-5}$ $s^{-1}$) | | | | Shearing deformation rate ($10^{-5}$ $s^{-1}$) | | | |
|---|---|---|---|---|---|---|---|---|
| | mean | | ± 95% | ± 95% | mean | | ± 95% | ± 95% |
| 120 | 3.56 | 1.64 | 4.10 | 2.50 | -1.22 | 6.02 | 6.69 | 1.11 |
| 205 | 9.93 | 2.55 | 3.37 | 1.32 | -.540 | 2.09 | 4.15 | 1.99 |
| 220 | 5.03 | .763 | 2.45 | 3.21 | -1.61 | 5.71 | 7.75 | 1.36 |
| 305 | 2.02 | 1.24 | 2.91 | 2.35 | 2.40 | 1.42 | 2.94 | 2.07 |
| 320 | 0.140 | 1.54 | 1.97 | 1.28 | -3.50 | 2.08 | 2.49 | 1.20 |
| 520 | -.870 | 0.280 | 1.74 | 6.21 | 3.94 | 0.970 | 2.69 | 2.77 |
| 605 | 5.14 | 2.99 | 4.17 | 1.40 | 1.58 | 3.90 | 4.51 | 1.16 |
| 620 | 2.33 | 4.42 | 1.40 | 0.317 | 0.340 | 2.82 | 2.00 | 0.709 |
| mean of all experiment | 3.41 | 1.93 | 2.76 | 2.32 | .174 | 3.13 | 4.15 | 1.55 |
| mean of all values | 2.65 | 3.57 | | | 0.420 | 4.26 | | |

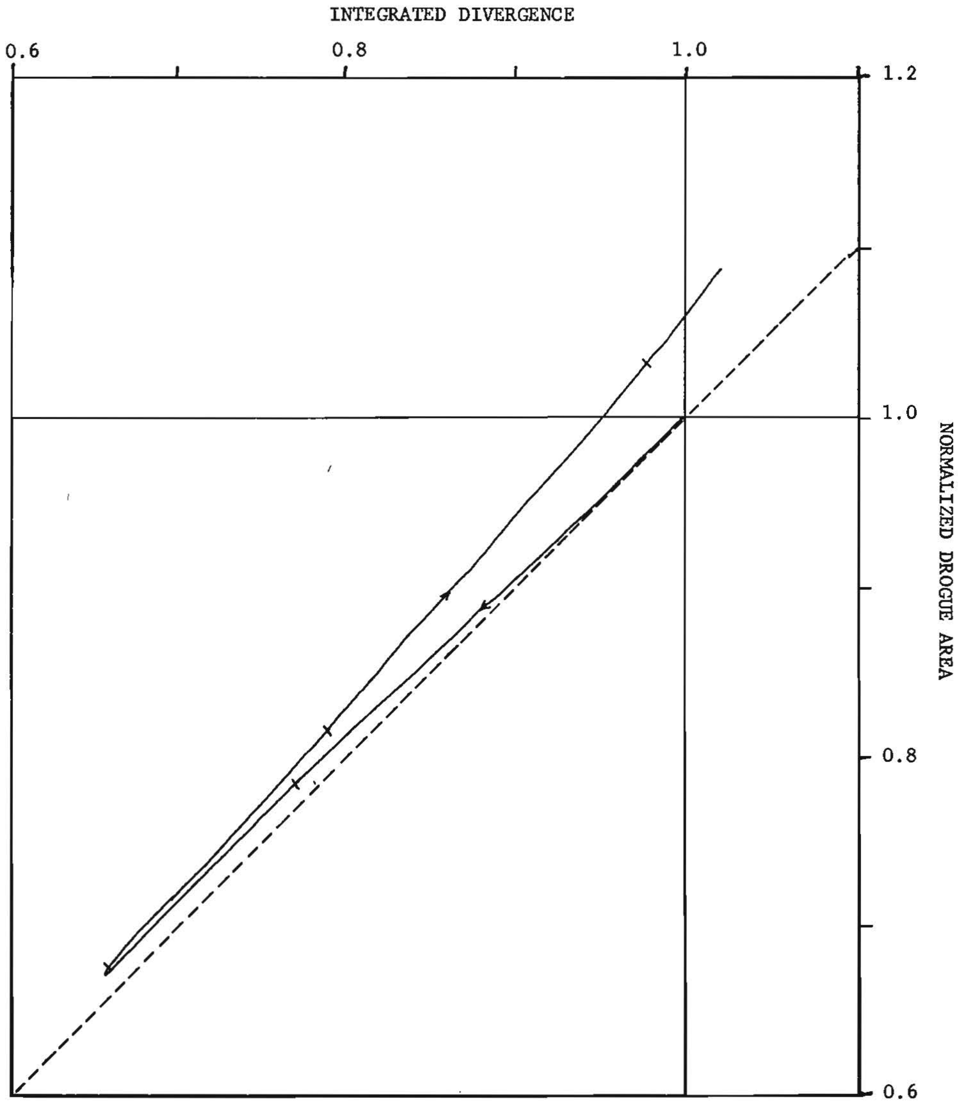


Figure 5a1. Time series of normalized drogue area versus integrated divergence for experiment 120. Tics mark one hour intervals. Dashed line represents equality.

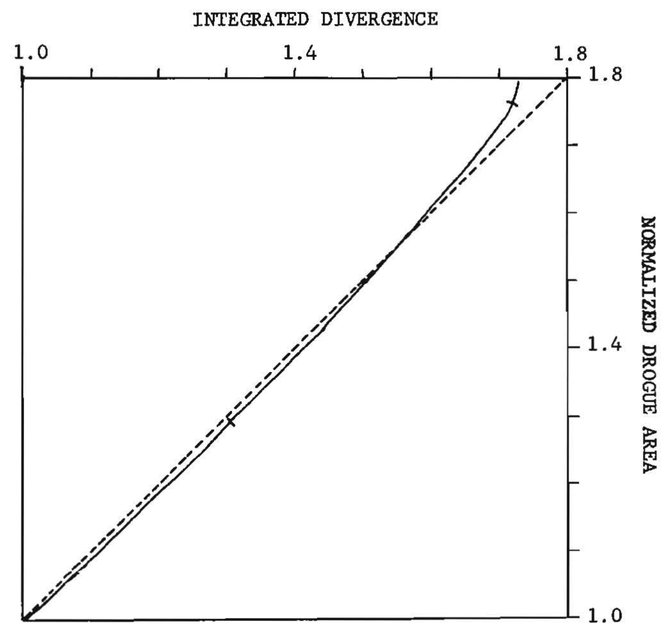


Figure 5a2. Time series of normalized drogue area versus integrated divergence for experiment 205. Tics mark one hour intervals. Dashed line represents equality.

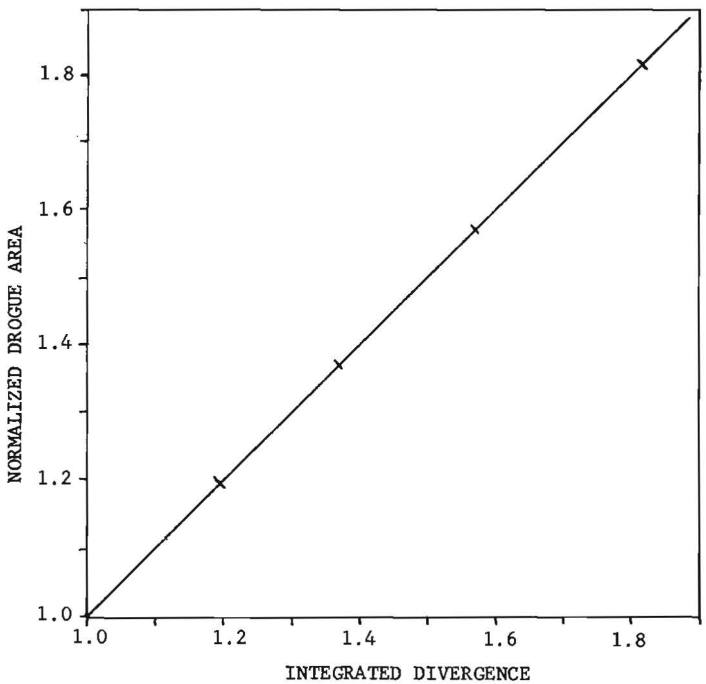


Figure 5a3. Time series of normalized drogue area versus integrated divergence for experiment 220. Tics mark half hour intervals.

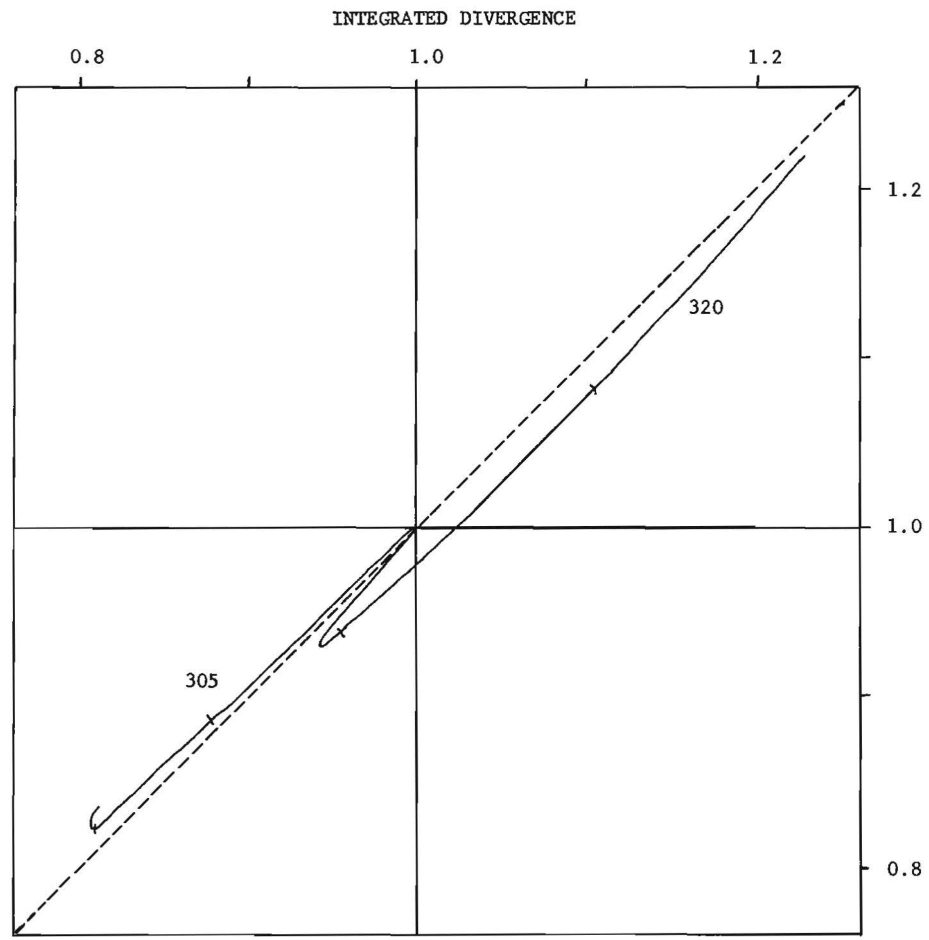


Figure 5a4. Time series of normalized drogue area versus integrated divergence for experiments 305 and 320. Tics mark one hour intervals. Dashed line represents equality.

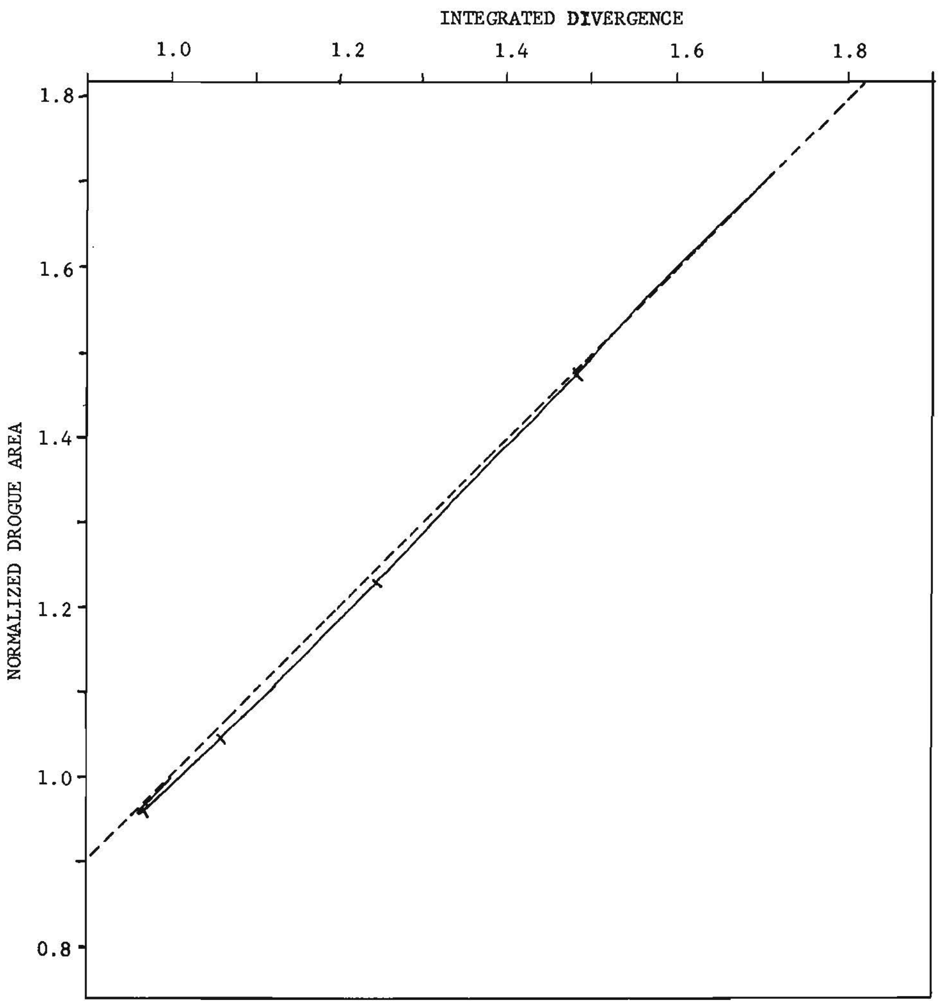


Figure 5a5. Time series of normalized drogue area versus integrated divergence for experiment 520. Tics mark one hour intervals. Dashed line represents equality.

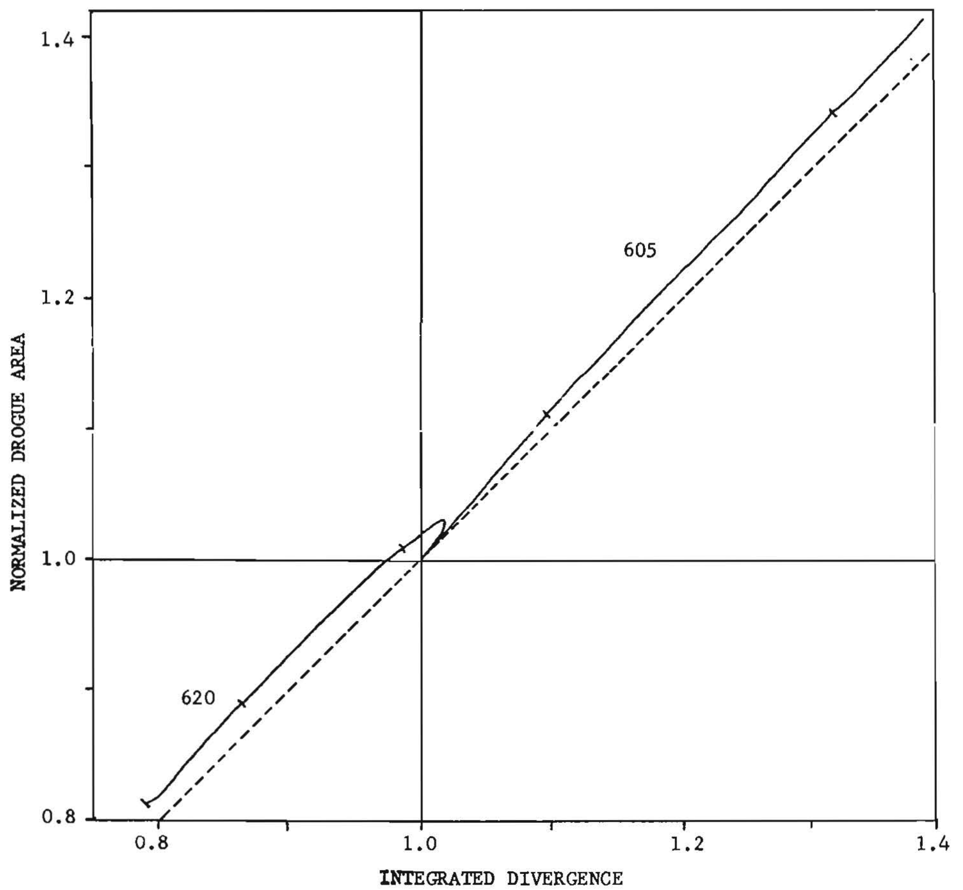


Figure 5a6. Time series of normalized drogue area versus integrated divergence for experiments 605 and 620. Tics mark one hour intervals. Dashed line represents equality.

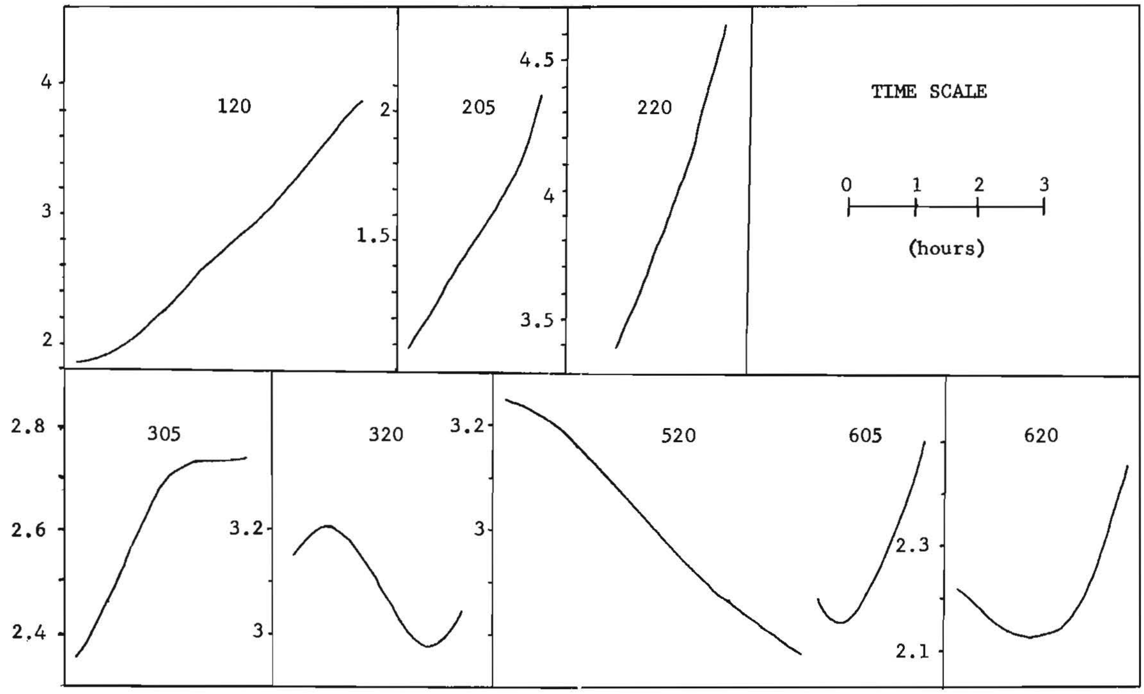


Figure 5b. Time series of elongation for each experiment.

dynamic equation

$$\frac{d}{dt}(\eta+f) + (\eta+f)\gamma + \left(\frac{\partial v}{\partial z}\frac{\partial w}{\partial x} - \frac{\partial u}{\partial z}\frac{\partial w}{\partial y}\right) - 2\Omega\cos\phi\,\frac{\partial w}{\partial y} + w\frac{\partial f}{\partial y}\tan\phi = -\left(\frac{\partial \alpha}{\partial x}\frac{\partial p}{\partial x} + \frac{\partial \alpha}{\partial y}\frac{\partial p}{\partial y}\right) + \left(\frac{\partial Fy}{\partial x} - \frac{\partial Fx}{\partial y}\right) \quad (5)$$

where

- $\eta$ : vertical component of relative vorticity
- $f$ : vertical component of planetary vorticity ($1.08 \times 10^{-4}\ s^{-1}$)
- $\gamma$ : horizontal divergence
- $u,v,w$ : x, y, z components of velocity
- $\Omega$ : earth's angular rotation
- $\phi$ : latitude
- $\alpha$ : specific volume of sea water
- $p$ : pressure
- $F_x, F_y$ : x, y - components of frictional forces

If we ignore the terms involving the vertical velocity and also the baroclinic term, (5) is reduced to

$$\frac{d}{dt}(\eta+f) + (\eta+f)\gamma = T_f \quad (6)$$

where $T_f \equiv \frac{\partial Fy}{\partial x} - \frac{\partial Fx}{\partial y}$ : frictional torque.

Dividing (6) by D, the vertical height of a water column and using the relation (4), we obtain

$$\frac{d}{dt}\left(\frac{\eta+f}{D}\right) = \frac{T_f}{D} \quad (7)$$

Equation (7) states that without frictional torque, potential vorticity, $\frac{\eta+f}{D}$, is conserved:

$$\frac{\eta+f}{D} = \text{constant} \quad (8)$$

Figure 6 shows for each experiment time series of frictional torque (computed as in OE) versus D times rate of change of potential vorticity. 95% confidence limits of frictional torque have been added to show the significance of deviations from 45° -- a perfect balance. In general the simple balance of eq. (7) is satisfied within the 95% confidence limits. The mean relation usually forms a straight line deviating somewhat from the perfect 45° inclination.

(c) Singularity diagrams

Okubo (1970) developed a method of classifying singularities of two-dimensional fluid flow according to a graph of divergence $\gamma$ versus a stability parameter $S \equiv \alpha^2 + h^2 - \eta^2$. The various regions and lines on such a "singularity diagram" are classified according to six types of singularity: inward and outward spirals; vortices; inward and outward nodal points and saddle points.

Figure 7 shows time series of singularity diagrams for each experiment. No patterns are apparent in the temporal variations. From Figure 7 the number of observations of each type of singularity has been summarized in Table 3. Thus we find approximately 1/3 of all observations classified as spirals (38%), nodals (32%) or saddles (30%).

(d) Comparison of $\partial u/\partial y$ computed from OEH and Eb methods

Ebbesmeyer (1975) noted that the current shear component $\partial u/\partial y$ could be computed from temporal variations of the linear regression coefficient, or

$$\frac{\partial u}{\partial y} = \frac{1}{t}\,\frac{d(\beta^{-1}t)}{dt}$$

$$\beta = \frac{1}{\rho}\,\frac{\sigma_y}{\sigma_x} \quad (9)$$

and $\rho^2$ is the correlation coefficient. Equation (9) is valid under the following assumptions: point-source initial condition, purely shearing flow ($\eta(t) = -h(t)$, $\gamma(t) = \alpha(t) = 0$) and constant eddy diffusivities.

Results from the OEH procedure (Fig. 4)

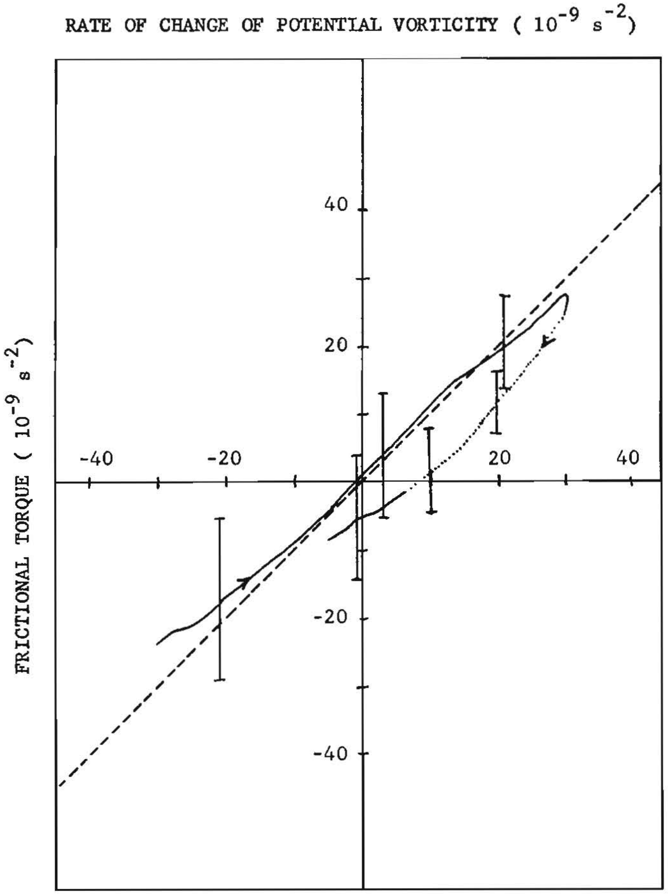


Figure 6a. Time series of vorticity balance in eq. 6 for experiment 120. Bars represent 95% confidence limits of frictional torque. Dotted line represents interval when bars do not extend past 45° inclination (dashed line) which corresponds with balance of frictional torque and rate of change of potential vorticity in the unit water column.

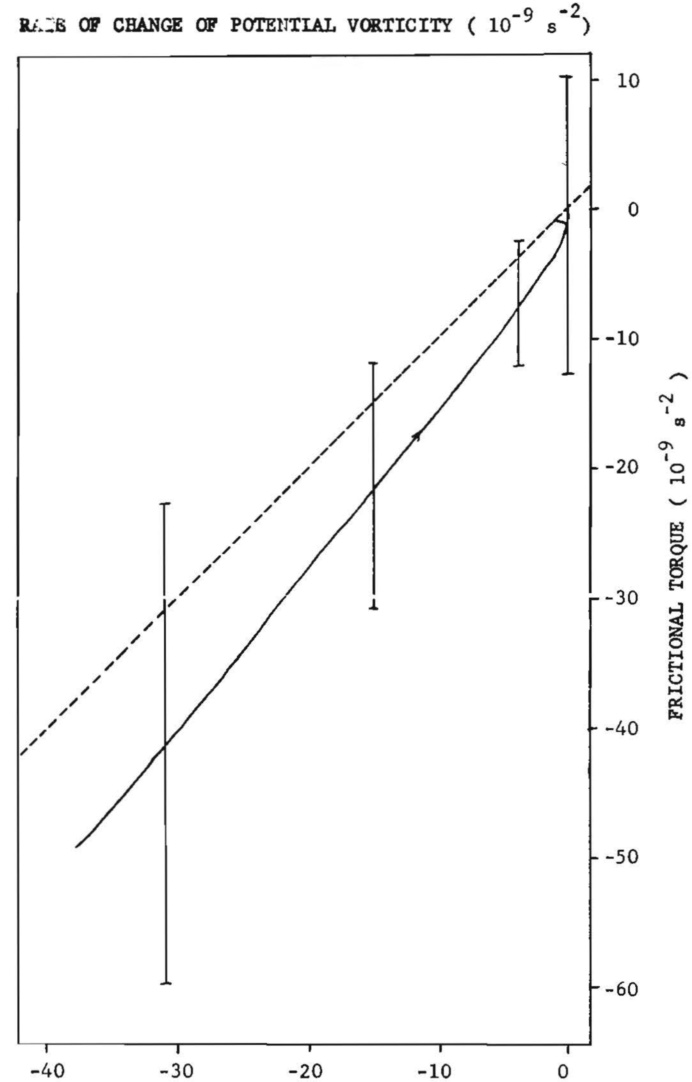


Figure 6b. Time series of vorticity balance in eq. 6 for experiment 205. Bars represent 95% confidence limits of frictional torque. Dashed line at 45° inclination corresponds with balance of frictional torque and rate of change of potential vorticity in the unit water column.

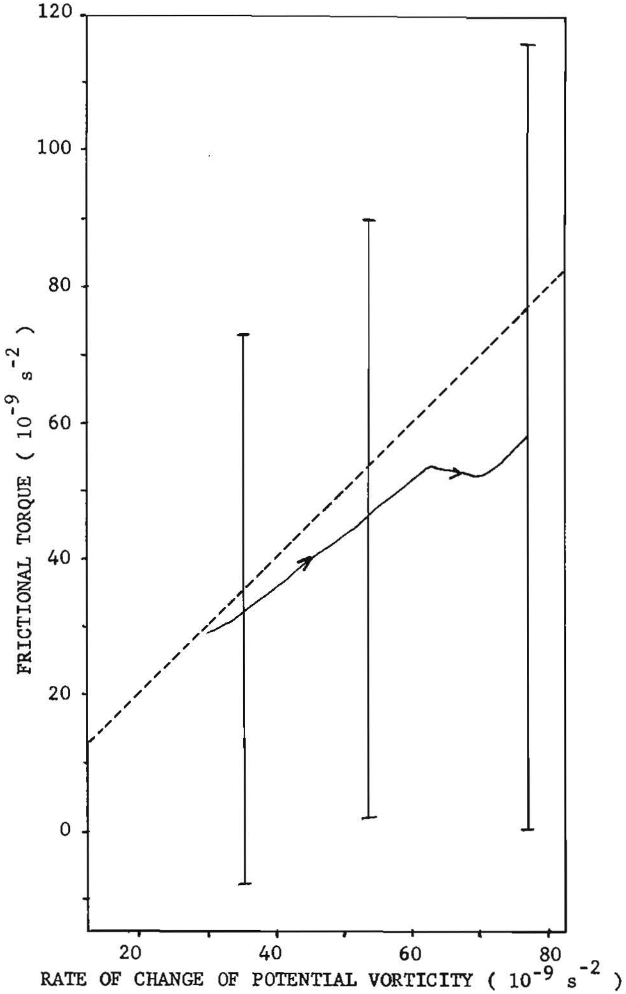


Figure 6c. Time series of vorticity balance in eq. 6 for experiment 220. Bars represent 95% confidence limits of frictional torque. Dashed line at 45° inclination corresponds with balance of frictional torque and rate of change of potential vorticity in the unit water column.

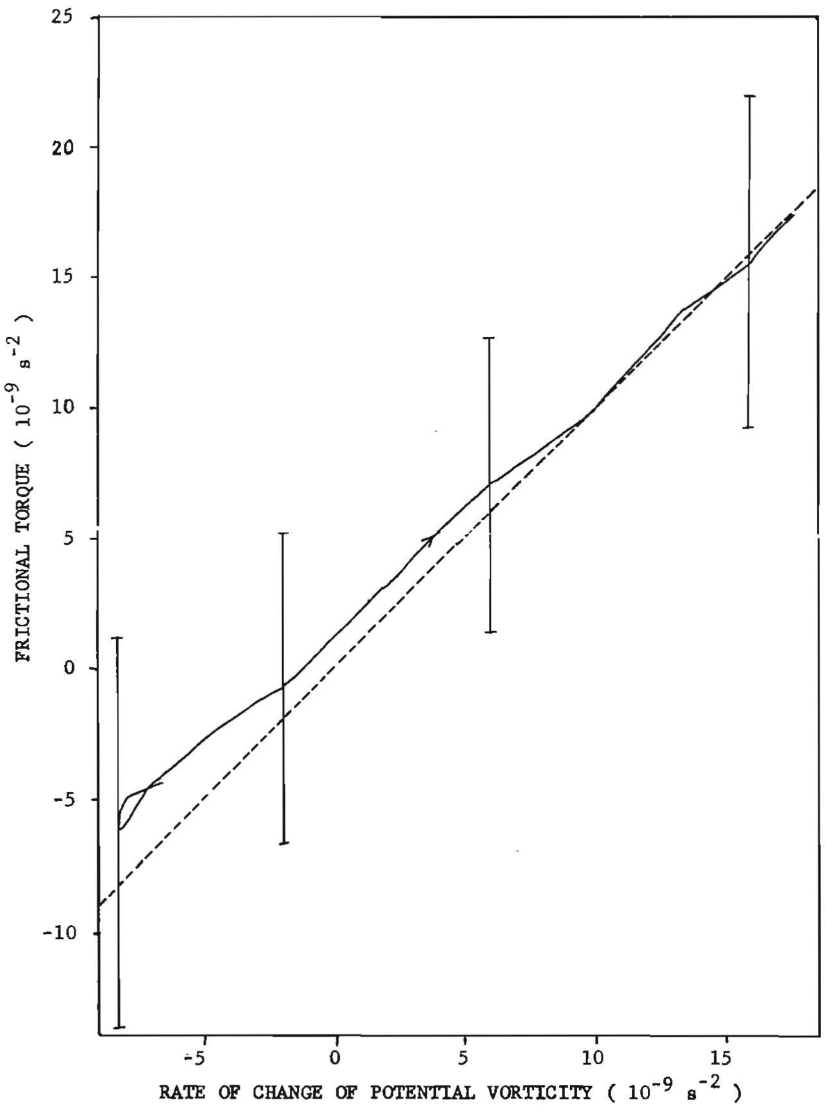


Figure 6d. Time series of vorticity balance in eq. 6 for experiment 305. Bars represent 95% confidence limits of frictional torque. Dashed line at 45° inclination corresponds with balance of frictional torque and rate of change of potential vorticity in the unit water column.

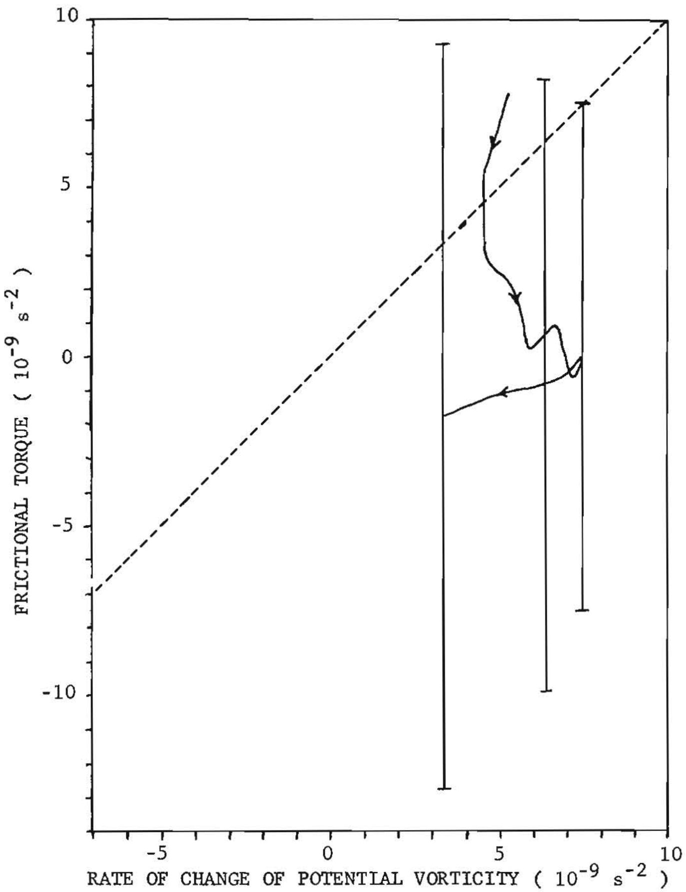


Figure 6e. Time series of vorticity balance in eq. 6 for experiment 320. Bars represent 95% confidence limits of frictional torque. Dashed line at 45° inclination corresponds with balance of frictional torque and rate of change of potential vorticity in the unit water column.

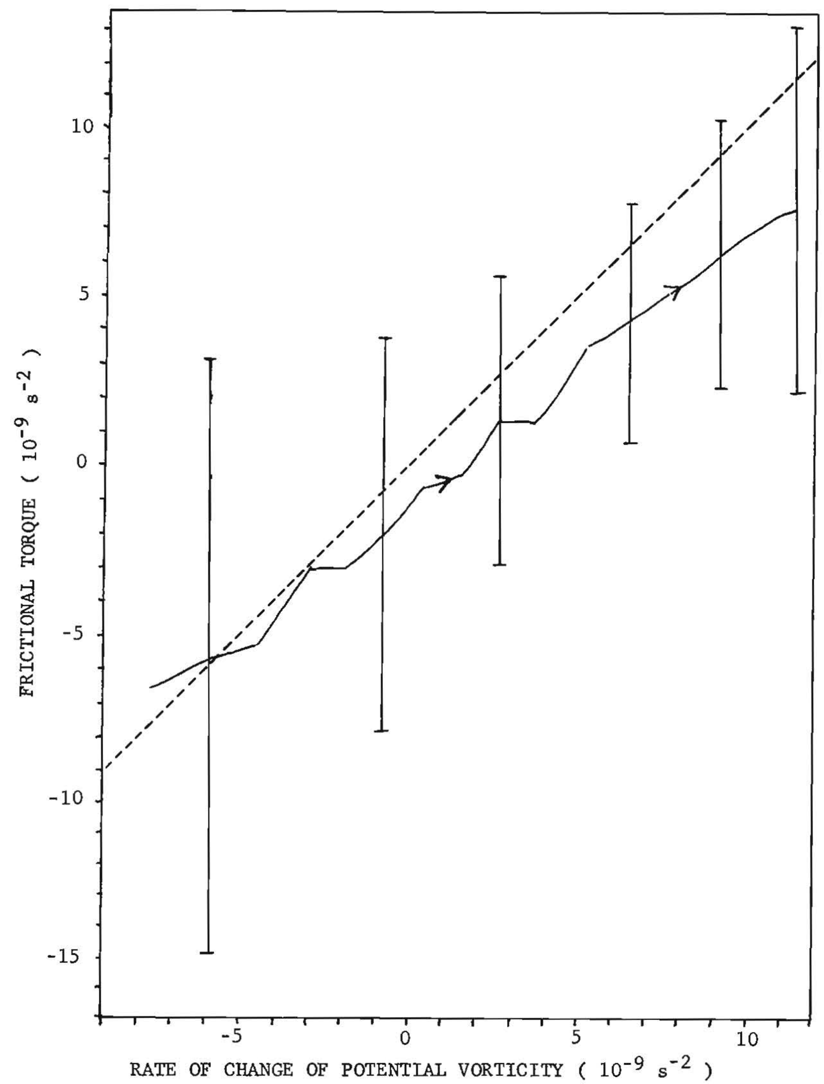


Figure 6f. Time series of vorticity balance in eq. 6 for experiment 520. Bars represent 95% confidence limits of frictional torque. Dashed line at 45° inclination corresponds with balance of frictional torque and rate of change of potential vorticity in the unit water column.

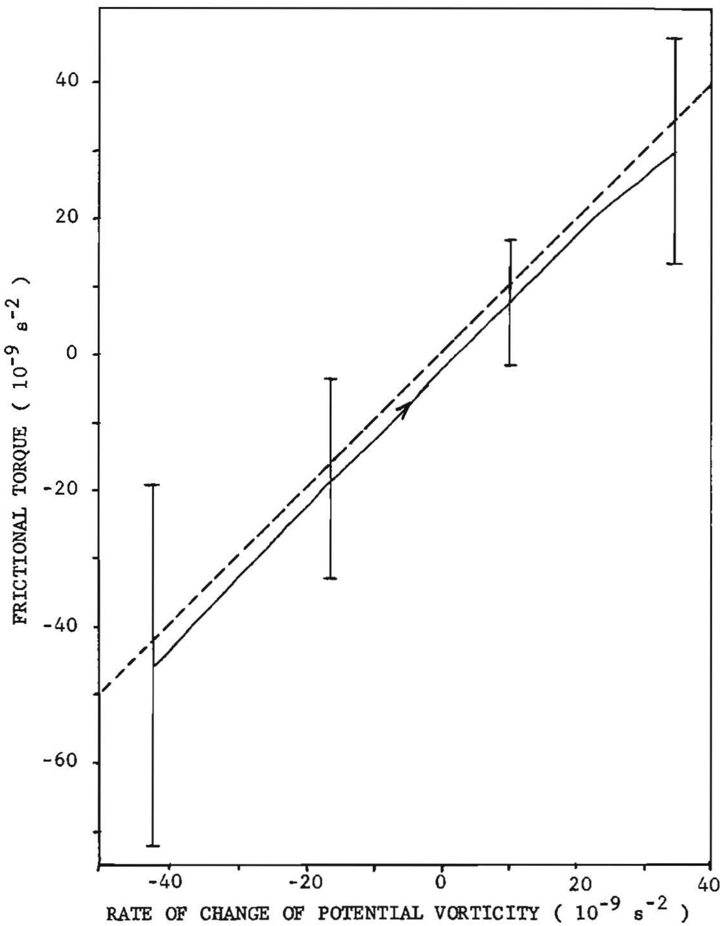


Figure 6g. Time series of vorticity balance in eq. 6 for experiment 605. Bars represent 95% confidence limits of frictional torque. Dashed line at 45° inclination corresponds with balance of frictional torque and rate of change of potential vorticity in the unit water column.

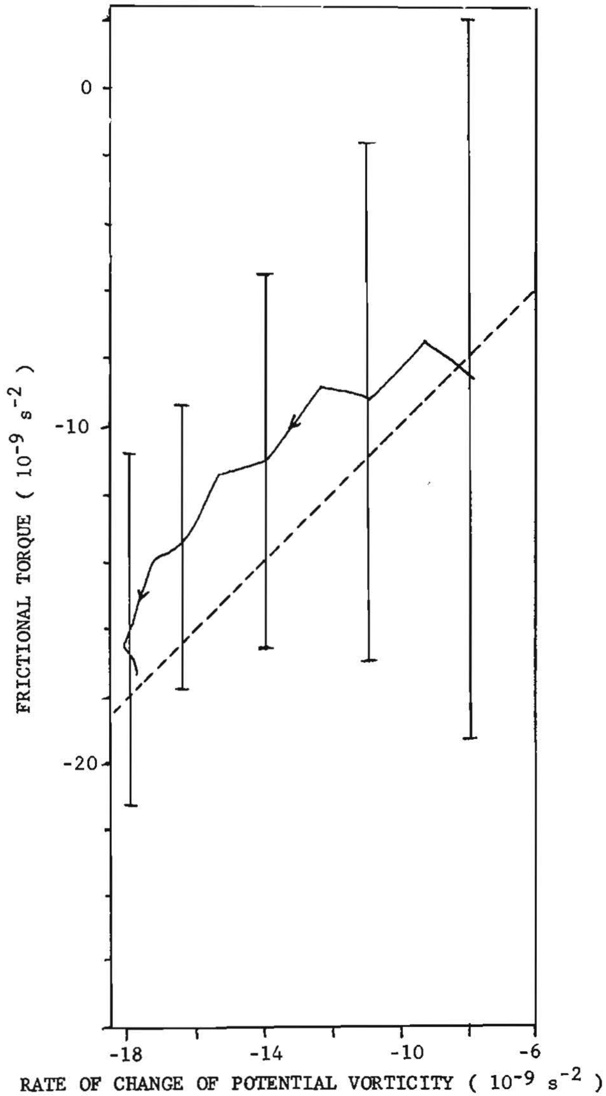


Figure 6h. Time series of vorticity balance in eq. 6 for experiment 620. Bars represents 95% confidence limits of frictional torque. Dashed line at 45° inclination corresponds with balance of frictional torque and rate of change of potential vorticity in the unit water column.

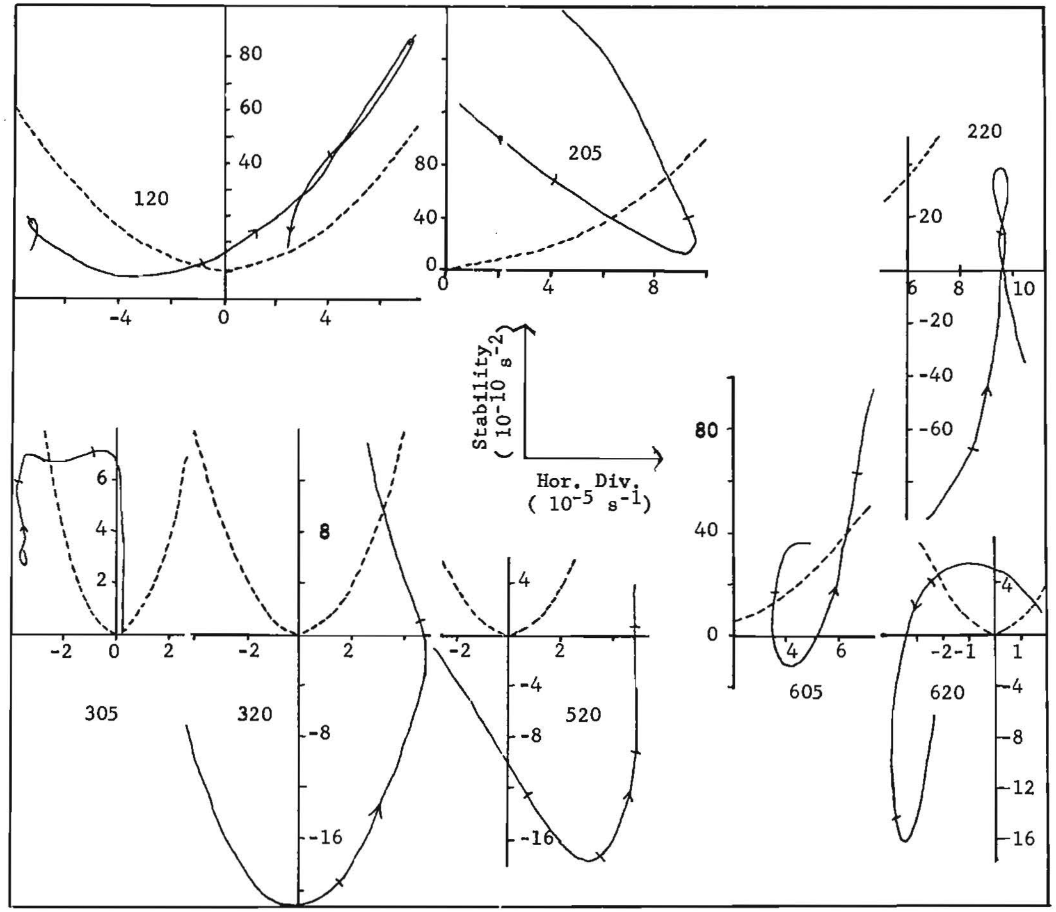


Figure 7a. Singularity diagrams for each experiment. Time proceeds in direction of arrow. Dashed line separates saddle and nodal points.

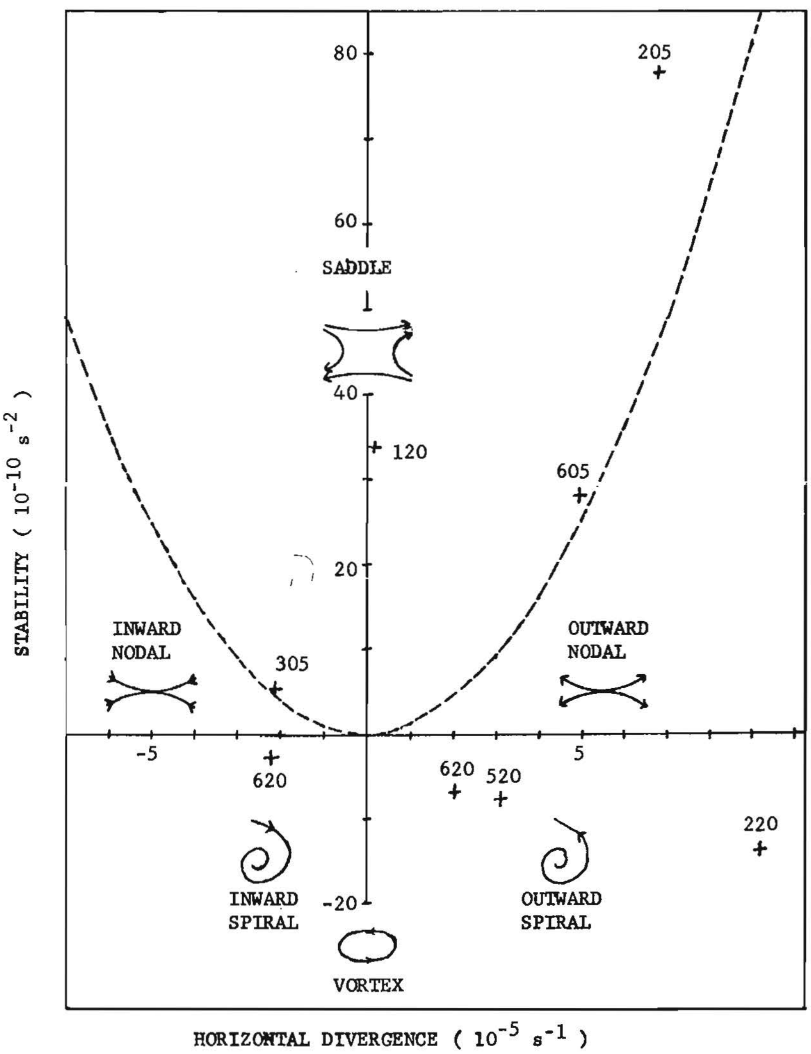


Figure 7b. Singularity diagram for mean values (+) of each experiment. Dashed line represents division between saddle and nodal singularities.

Table 3. Distribution of flow singularities. Numbers of 0.2 hour intervals having designated singularities.

| Experiment designation | Type of Singularity | | | | | |
|---|---|---|---|---|---|---|
| | Inward nodal | Outward nodal | Saddle | Inward spiral | Outward spiral | Vortex |
| 120 | 9 | 0 | 14 | 0 | 0 | 0 |
| 205 | 0 | 6 | 5 | 0 | 0 | 0 |
| 220 | 0 | 4 | 0 | 0 | 5 | 0 |
| 305 | 7 | 0 | 7 | 0 | 0 | 0 |
| 320 | 0 | 3 | 1 | 3 | 7 | 0 |
| 520 | 0 | 4 | 0 | 3 | 15 | 1 |
| 605 | 0 | 1 | 5 | 0 | 3 | 0 |
| 620 | 2 | 1 | 3 | 7 | 0 | 0 |
| Totals | 18 | 19 | 35 | 13 | 30 | 1 |
| % of Grand Total (116) | 15.5 | 16.4 | 30.2 | 11.2 | 25.9 | 0.9 |

show that these assumptions are not matched at instantaneous times. However Table 2 and the histograms of Figures 4b and 4d show that time averages of $\eta$ and h tend to be of opposite size, partially validating assumption of purely shearing flow. To validate assumption of point-source initial condition we simulated a point-source by subtracting initial drogue coordinates from subsequent positions for each experiment. We then applied the OEH and Eb methods to these corrected positions and obtained average $\partial u/\partial y$ for each experiment. The results are shown in Figure 8.

Figure 8a shows that the Eb method approximates the OEH method for time averages as follows

$$\overline{\left(\frac{\partial u}{\partial y}\right)}_{OEH} \approx 0.2 \overline{\left(\frac{\partial u}{\partial y}\right)}_{Eb} \tag{10}$$

It should be kept in mind that the OEH method uses four shears to 'fit' the flow field, whereas the Eb method is much simpler and uses only one shear component.

### 3.5 *Turbulence characteristics*

Turbulence characteristics have been computed using OE and OEH methods. The characteristics of interest are:

(a) Standard deviation of turbulent displacement, $\sigma''_r$

$$\sigma''_r \equiv (\sigma''^2_X + \sigma''^2_Y)^{1/2} \tag{11}$$

where $\sigma''_X$, $\sigma''_Y$ are standard deviations of component turbulent displacements directed along the mean principal axes.

(b) Standard deviation of turbulent speed, $\sigma''_s$

$$\sigma''_s \equiv (\sigma''^2_u + \sigma''^2_v)^{1/2} \tag{12}$$

where $\sigma''_u$, $\sigma''_v$ are standard deviations of turbulent speed components directed along the mean principal axes.

(c) Relative turbulent speed

This is defined as a percentage;

$$100\ \sigma''_s(\bar{u}^2 + \bar{v}^2)^{-1/2} \tag{13}$$

where $\bar{u}$, $\bar{v}$ are centroid speed components directed along the mean principal axes.

(d) Momentary eddy diffusivities, $K_x$, $K_y$

Component momentary eddy diffusivities $K_x$, $K_y$ directed along the mean major and minor axes are defined as

$$K_x \equiv \sigma''_x\ \sigma''_u$$

$$K_y \equiv \sigma''_y\ \sigma''_v$$

$$K \equiv (K_x K_y)^{1/2} \tag{14}$$

Standard deviations of turbulent displacements and speeds, and momentary eddy diffusivities were computed at 0.2 hour intervals for each experiment and graphed in Figure 9. Table 4 contains time averages of $\sigma''_r$, $\sigma''_s$, K, $K_x$, and $K_y$. From Figure 9 and Table 4 we make the following observations:

(i) There are no apparent patterns to temporal variations of turbulent characteristics.

(ii) The standard deviation of turbulent displacement, $\sigma''_r$, approximates Okubo and Farlow's (1967) length of energy containing eddies. For comparison we computed time averaged $\sigma''_r$ from unsmooth positions as shown in Table 5. The average difference between $\sigma''_r$ computed from smooth and unsmooth positions is 5.8 m -- about equal to our estimate of positioning errors after initial editing described in Chapter 2.

(iii) The standard deviation of turbulent speed exceeds Okubo and Farlow's (1967) turbulent intensities by a factor of about 2.2. We also note that

$$\sigma''_s \approx \sigma''_r(\Delta t)^{-1} \tag{15}$$

provides a close approximation.

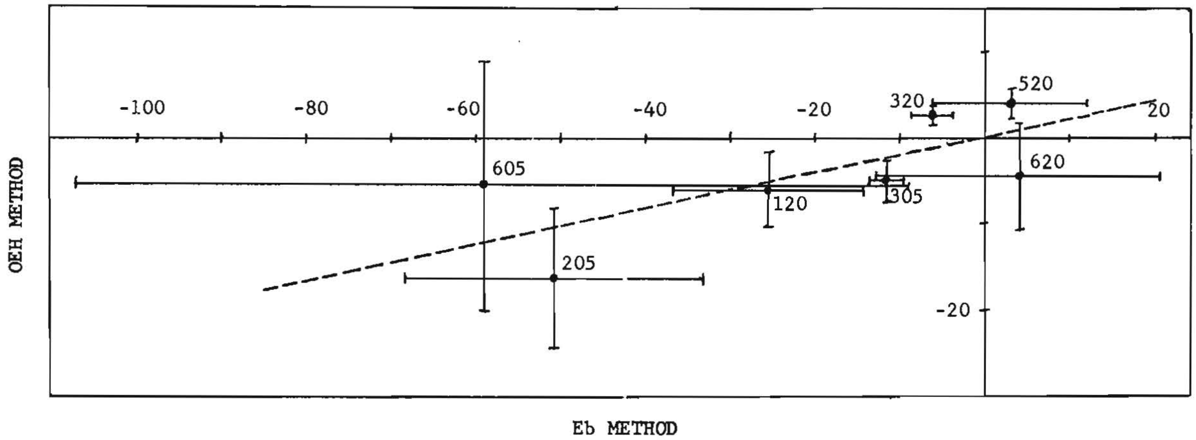


Figure 8a. Comparison of mean $\partial u/\partial y$ computed from OEH method (Okubo, Ebbesmeyer, and Helseth (1975)) and Eb method (Ebbesmeyer (1975)). Both axes are in units of $10^{-5}$ $s^{-1}$. Dashed line represents relation $(\partial u/\partial y)_{OEH} = 0.2\ (\partial u/\partial y)_{Eb}$. Bars represent one standard deviation of instantaneous values for each experiment.

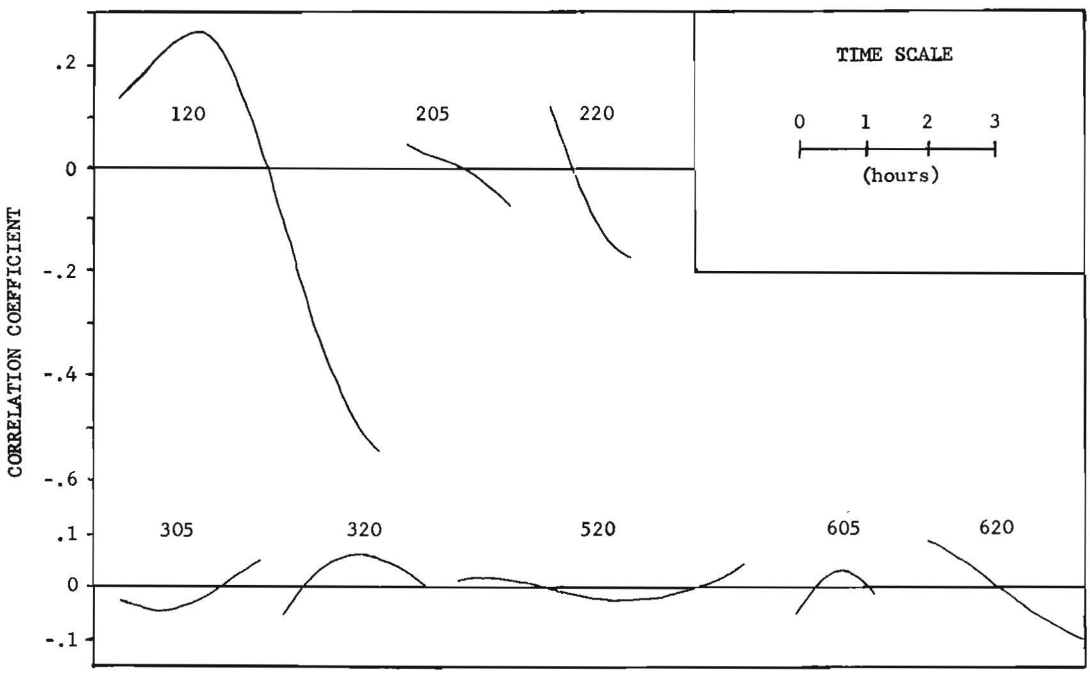


Figure 8b. Time series of the correlation coefficient for each experiment.

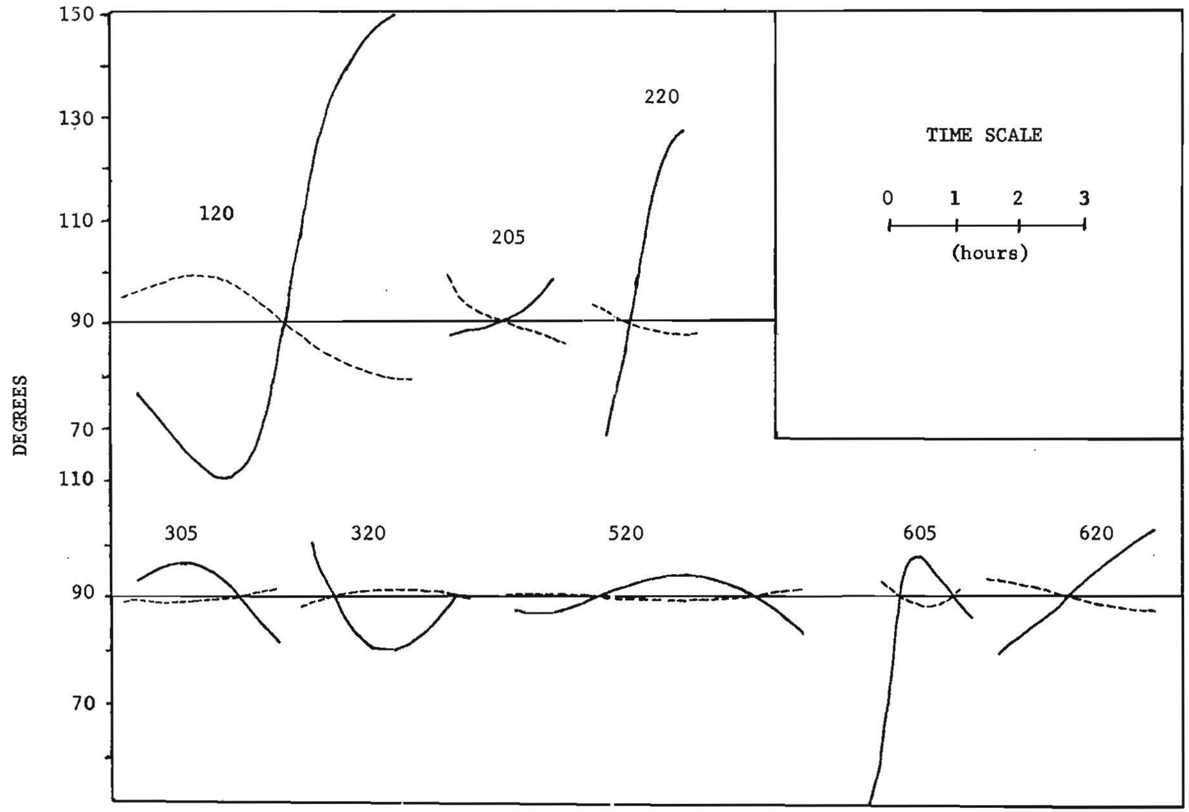


Figure 8c. Time series of the angles ( measured from the x-axis ) of the regression coefficient (solid lines) and deviations of the instantaneous minor axes (dashed lines).

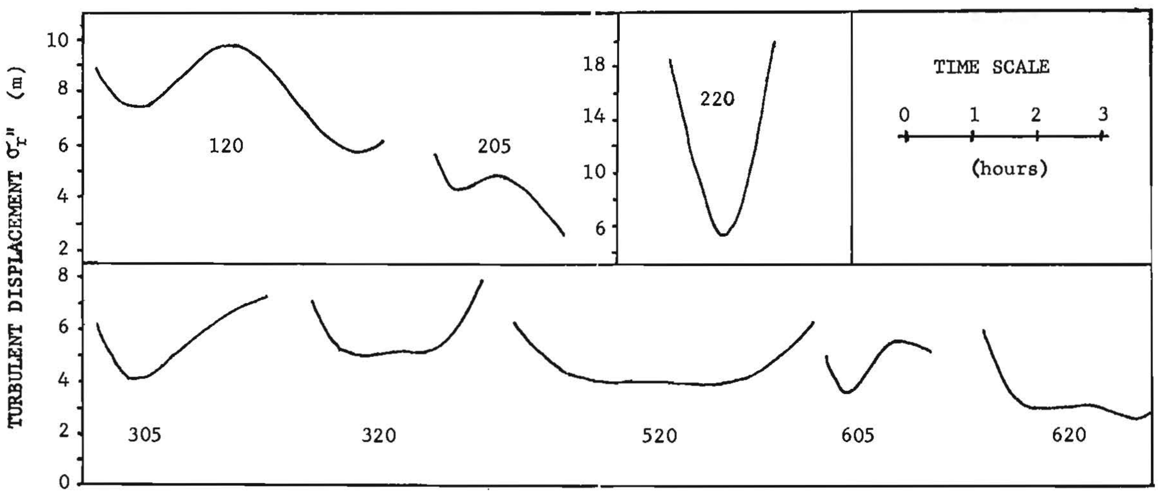


Figure 9a. Time series of turbulent displacement for each experiment.

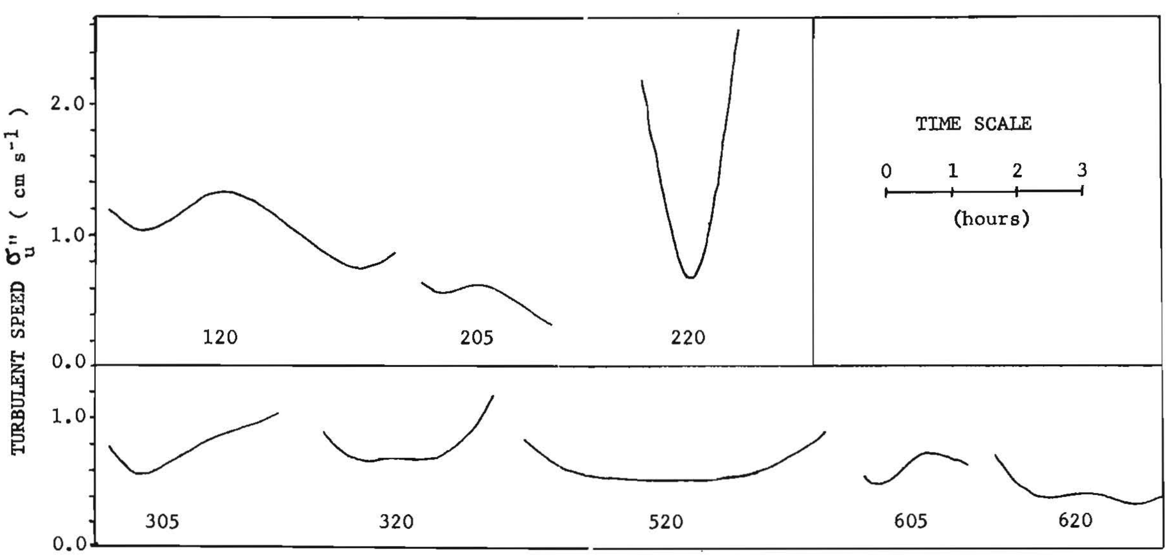


Figure 9b. Time series of turbulent speed for each experiment.

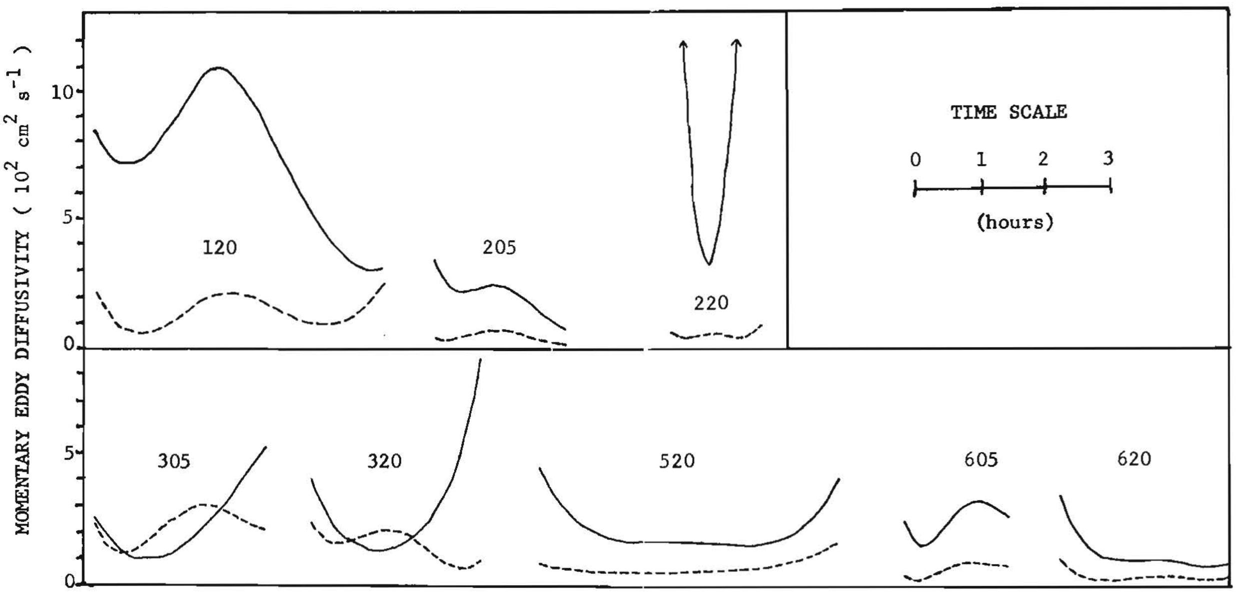


Figure 9c. Time series of components of momentary eddy diffusivity. $K_x$, solid lines; $K_y$, dashed lines.

Table 4

Mean turbulence characteristics

| Experiment designation | Standard deviation of turbulent displacement $\sigma_r''$ (m) | | | Standard deviation of turbulent speed $\sigma_s''$ (cm s$^{-1}$) | Momentary eddy diffusivities ($10^2$ cm$^2$ s$^{-1}$) | | |
|---|---|---|---|---|---|---|---|
| | (1) For un-smooth positions | (2) For smooth positions | (2)-(1) | | $K_x$ | $K_y$ | $K$ |
| 120 | 21.2 | 7.92 | 13.3 | 1.06 | 7.24 | 1.43 | 3.13 |
| 205 | 5.06 | 4.38 | 0.68 | 0.545 | 2.03 | 0.439 | 0.932 |
| 220 | 25.9 | 12.1 | 13.8 | 1.61 | 22.1 | 2.14 | 3.62 |
| 305 | 6.70 | 5.65 | 1.05 | 0.792 | 2.37 | 2.25 | 2.23 |
| 320 | 8.07 | 5.77 | 2.30 | 0.791 | 3.11 | 1.58 | 2.02 |
| 520 | 8.86 | 4.58 | 4.28 | 0.626 | 2.22 | 0.733 | 1.26 |
| 605 | 9.81 | 4.90 | 4.91 | 0.640 | 2.54 | 0.649 | 1.27 |
| 620 | 9.52 | 3.38 | 6.14 | 0.453 | 1.25 | 0.371 | 0.676 |

Table 5a. Times at which properties of clusters and random selection were computed.

| Experiment designation | Beginning | Middle (hours) | End |
|---|---|---|---|
| 120 | .4 | 2.4 | 4.4 |
| 205 | .4 | 1.2 | 2.0 |
| 220 | 1.0 | 1.8 | 2.4 |
| 305 | .4 | 1.6 | 2.6 |
| 320 | .5 | 1.7 | 2.7 |
| 520 | 1.0 | 2.8 | 4.6 |
| 605 | .8 | 1.4 | 2.0 |
| 620 | .4 | 1.6 | 2.8 |

Table 5b. Numbers of drogues within clusters.

| Experiment designation | Numbers of drogues in clusters | | | | | | | |
|---|---|---|---|---|---|---|---|---|
| | A | B | C | D | E | F | G | H |
| 120 | 5 | 6 | 9 | 10 | 11 | | | |
| 205 | 11 | 19 | | | | | | |
| 220 | 4 | 4 | 4 | 5 | 6 | 6 | 8 | 12 |
| 305 | 9 | 9 | 10 | 10 | 13 | | | |
| 320 | 4 | 7 | 8 | 9 | 10 | 12 | | |
| 520 | 9 | 12 | 12 | 13 | 19 | | | |
| 605 | 4 | 6 | 8 | 10 | | 10 | | |
| 620 | 5 | 5 | 5 | 9 | 10 | | 10 | |

(iv) Momentary eddy diffusivity, K, averages $1.9 \times 10^2$ $cm^2$ $s^{-1}$ for all experiments. The corresponding components average $K_x = 5.4 \times 10^2$ $cm^2$ $s^{-1}$, and $K_y = 1.2 \times 10^2$ $cm^2$ $s^{-1}$, or a ratio $K_x K_y^{-1} = 4.5$.

# CHAPTER 4
# ANALYSIS OF SMALLER-SCALE VARIABILITY

## 4.1 *Clusters*

Examination of patterns within gross-scale drogue groups showed that each was composed of an average of five clusters. We distinguished these clusters by visual examination of patterns near the end of each experiment (Fig. 10) when clusters were most evident. Figure 10 shows the gross-scale drogue groups near the beginning, middle and end of each experiment. Table 5 shows the numbers of clusters and numbers of drogues within each cluster.

To examine smaller-scale variability, we computed properties as before for each cluster at the three times noted in Table 5. The results are summarized for divergence, vorticity, stability criterion and deformation rates in Figure 11; for the vorticity balance in Figure 12; and for turbulent displacement and speed in Table 6. Inspection of Figures 11 and 12 and Table 6 shows the following:

(i) In general divergence, vorticity and deformation rates within clusters show no relation to values within corresponding gross-scale drogue groups.

(ii) While the gross-scale expands, clusters tend to contract. We interpret Figure 11a as showing that drogues tend to cluster over local convergences while the clusters themselves tend to diverge.

(iii) The vorticity balance in eq. (7) is satisfied within clusters over a greater range of frictional torque and rate of change of potential vorticity than for gross-scale drogue groups.

(iv) Turbulent speed and displacement of clusters were both about one-half corresponding values of gross-scale drogue groups. This equals a reduction of turbulent speed of about 0.4 cm $s^{-1}$, and a reduction of turbulent displacement of 3.3 m. We attribute a significant part of these reductions to smaller numbers of drogues used in the computations. Typically each gross-scale drogue group contained an average of 5.3 clusters, each of which contained an average of 8.8 drogues.

## 4.2 *Random Selection*

A recurring question is: "How many drogues are sufficient for an experiment?" In an attempt to answer this question we selected at random (Marked slips of paper were drawn from a hat by a blindfolded person) 6, 8, 10, 12, 15, 20 and 30 drogues from each experiment (i.e., 56 different random selections) and determined properties for the three times noted in Table 5. We then graphed the standard deviation of differences between these random selections and corresponding gross-scale values as shown in Figure 13 for divergence, vorticity and deformation rates. Dashed lines in Figure 13 correspond to the average 95% confidence limits of the gross-scale of all experiments. The intersection of the dashed and solid lines indicates the number of drogues required to lower the standard deviation to the 95% confidence limits. For an alternative view Figure 14 shows gross-scale horizontal divergence and relative vorticity versus corresponding values for random selections of 6, 15 and 30 drogues.

Figure 13 shows that 10-15 drogues are required to achieve a standard deviation equal to the 95% confidence limits of the gross-scale drogue group. With hindsight we conclude that these experiments could have been conducted with 10-15

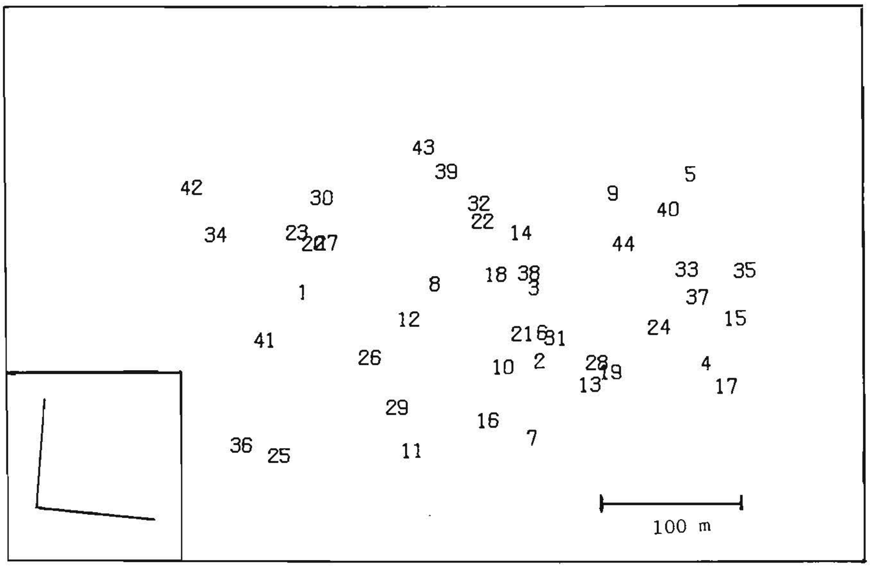


Figure 10a1. Positions of drogues used in gross-scale calculations for the beginning of experiment 120. Inset shows orientation of mean principal axes of diffusion.

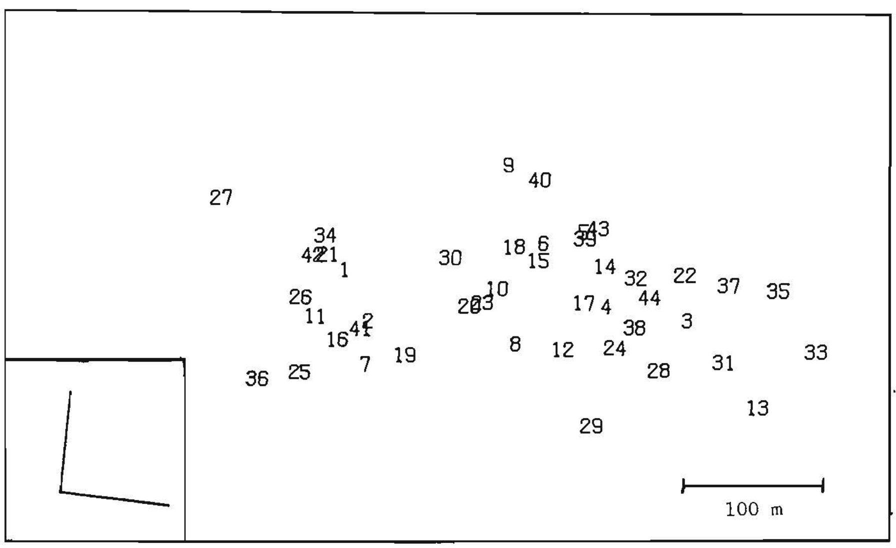


Figure 10a2. Positions of drogues used in gross-scale calculations for the middle of experiment 120. Inset shows orientation of mean principal axes of diffusion.

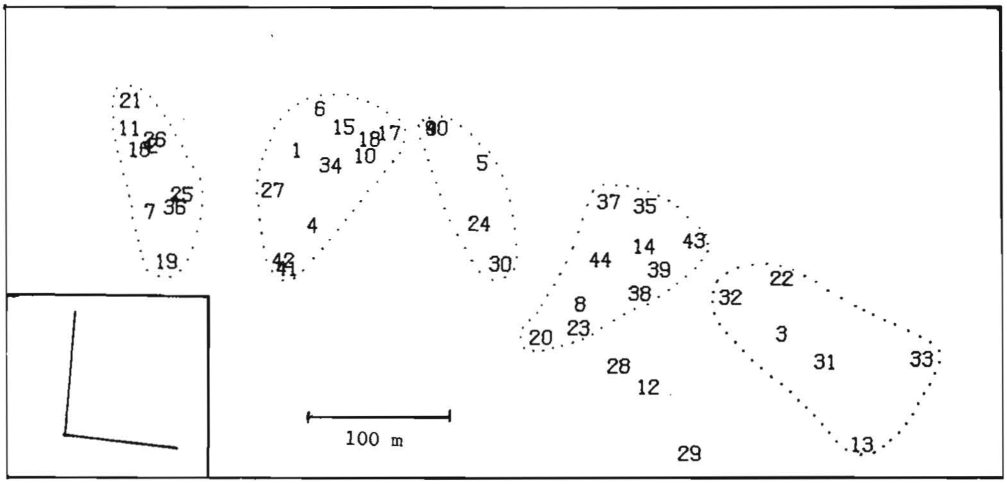


Figure 10a3. Positions of drogues used in gross-scale calculations for the end of experiment 120. Inset shows orientation of mean principal axes of diffusion. Dotted lines circumscribe clusters.

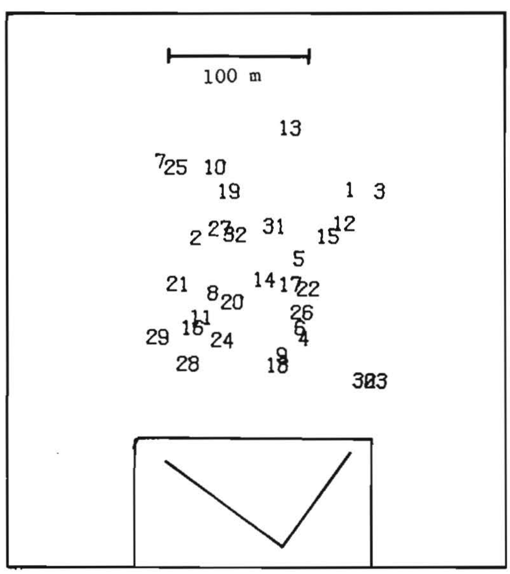


Figure 10b1. Positions of drogues used in gross-scale calculations for the beginning of experiment 205. Inset shows orientation of mean principal axes of diffusion.

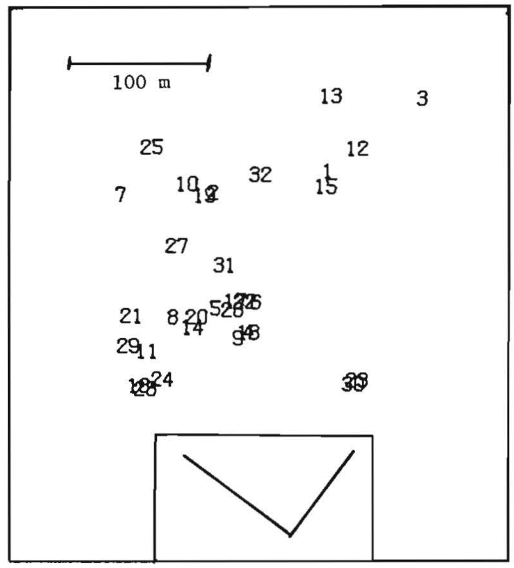


Figure 10b2. Positions of drogues used in gross-scale calculations for the middle of experiment 205. Inset shows orientation of mean principal axes of diffusion.

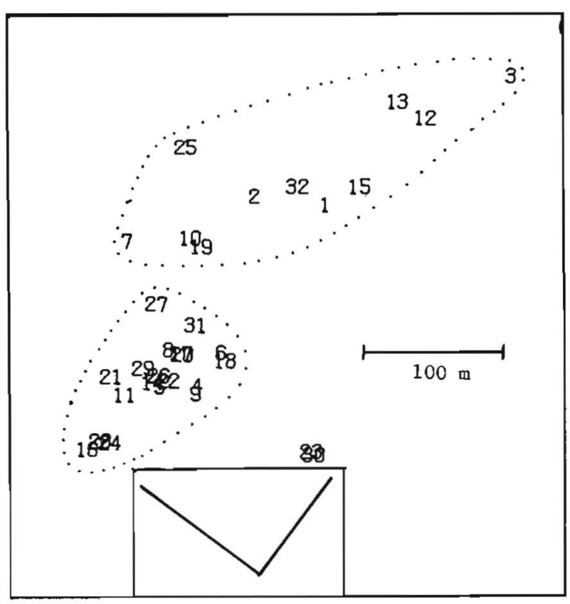


Figure 10b3. Positions of drogues used in gross-scale calculations for the end of experiment 205. Inset shows orientation of mean principal axes of diffusion. Dotted lines circumscribe clusters.

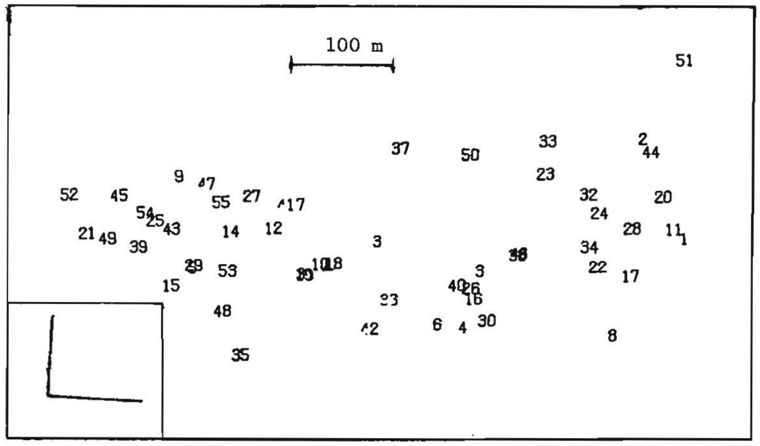


Figure 10c1. Positions of drogues used in gross-scale calculations for the beginning of experiment 220. Inset shows orientation of mean principal axes of diffusion.

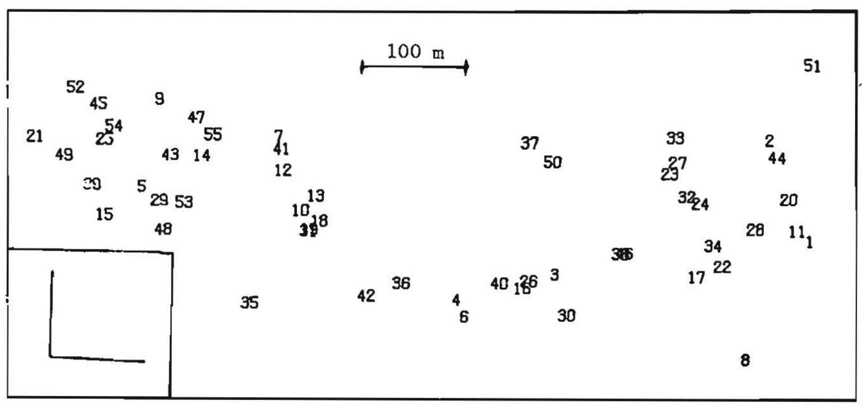


Figure 10c2. Positions of drogues used in gross-scale calculations for the middle of experiment 220. Inset show orientation of mean principal axes of diffusion.

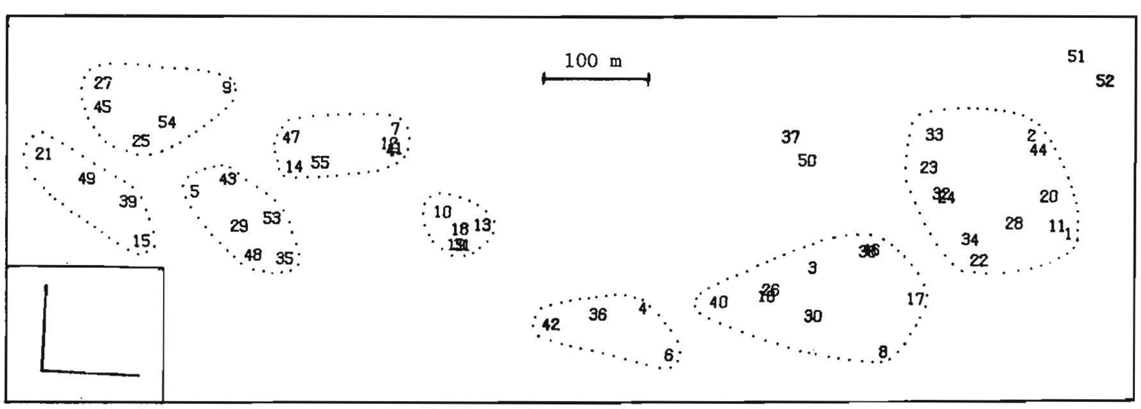


Figure 10c3. Positions of drogues used in gross-scale calculations for the end of experiment 220. Inset shows orientation of mean principal axes of diffusion. Dotted lines circumscribe clusters.

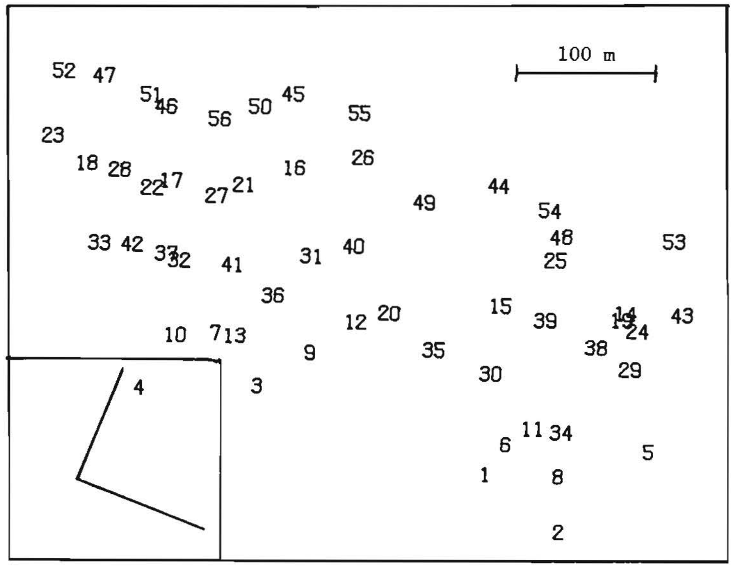


Figure 10d1. Positions of drogues used in gross-scale calculations for the beginning of experiment 305. Inset shows orientation of mean principal axes of diffusion.

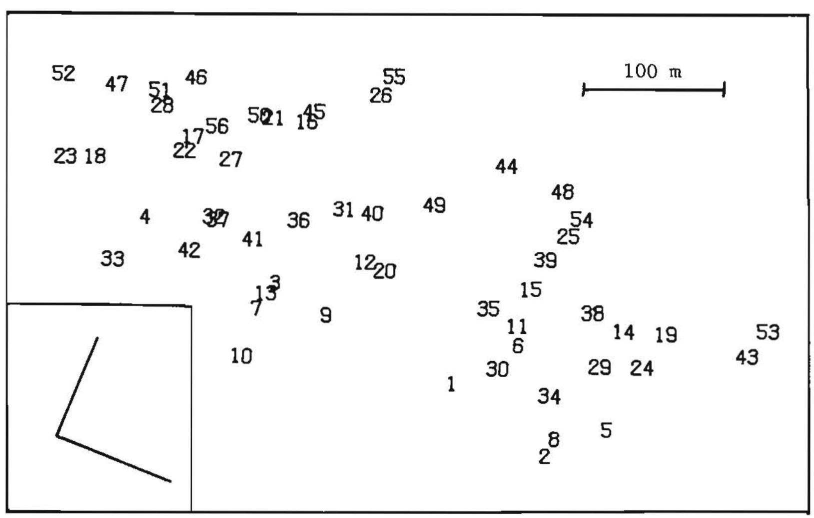


Figure 10d2. Positions of drogues used in gross-scale calculations for the middle of experiment 305. Inset shows orientation of mean principal axes of diffusion.

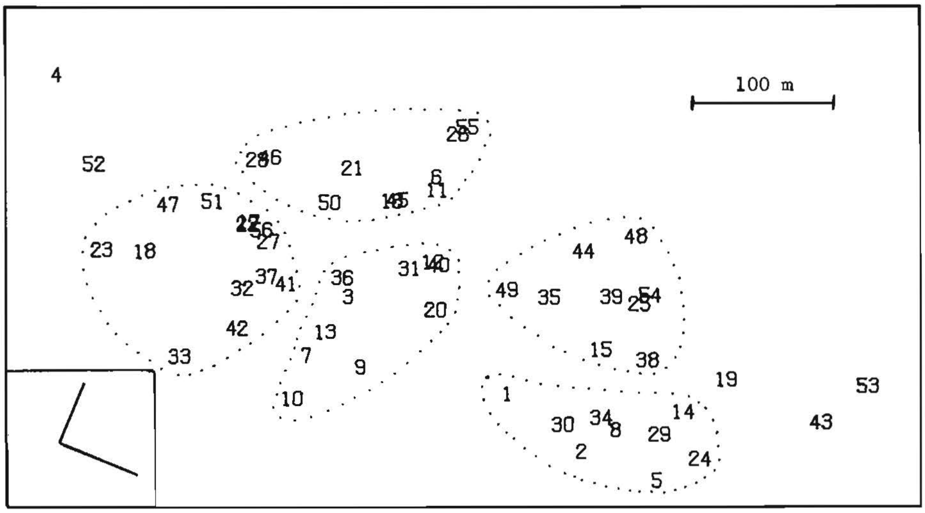


Figure 10d3. Positions of drogues used in gross-scale calculations for the end of experiment 305. Inset shows orientation of mean principal axes of diffusion. Dotted lines circumscribe clusters.

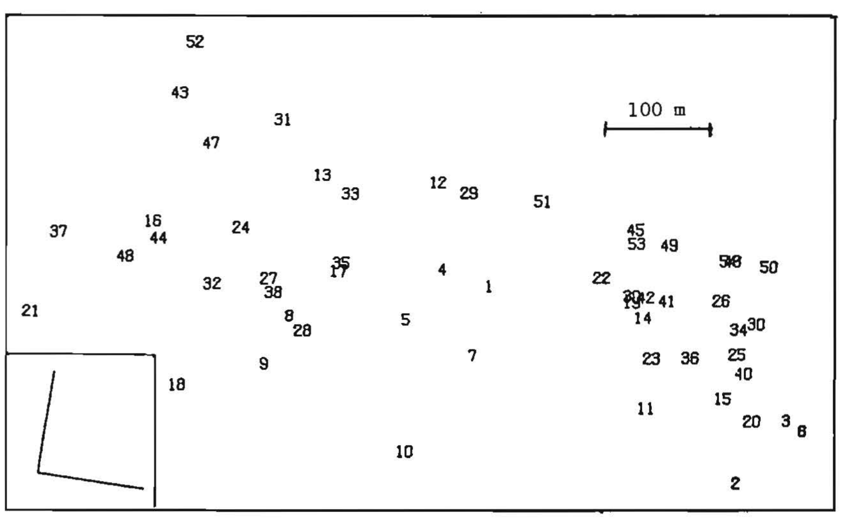


Figure 10e1. Positions of drogues used in gross-scale calculations for the beginning of experiment 320. Inset shows orientation of mean principal axes of diffusion.

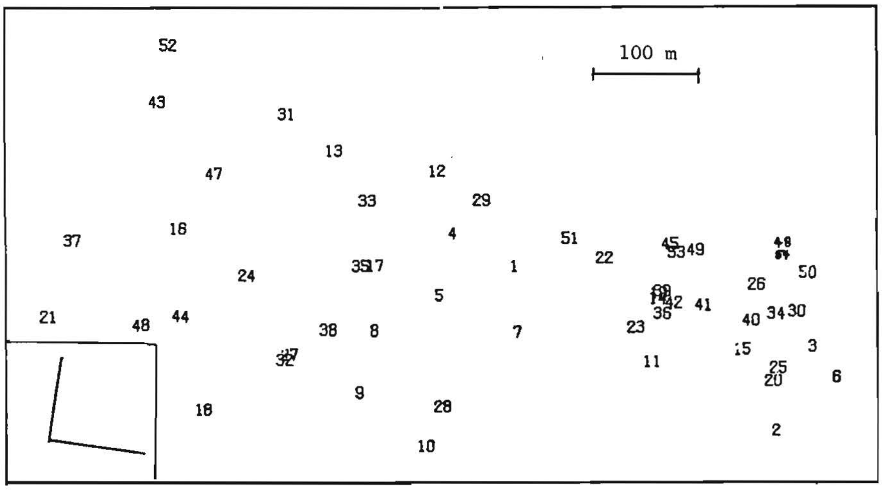


Figure 10e2. Positons of drogues used in gross-scale calculations for the middle of experiment 320. Inset shows orientation of mean principal axes of diffusion.

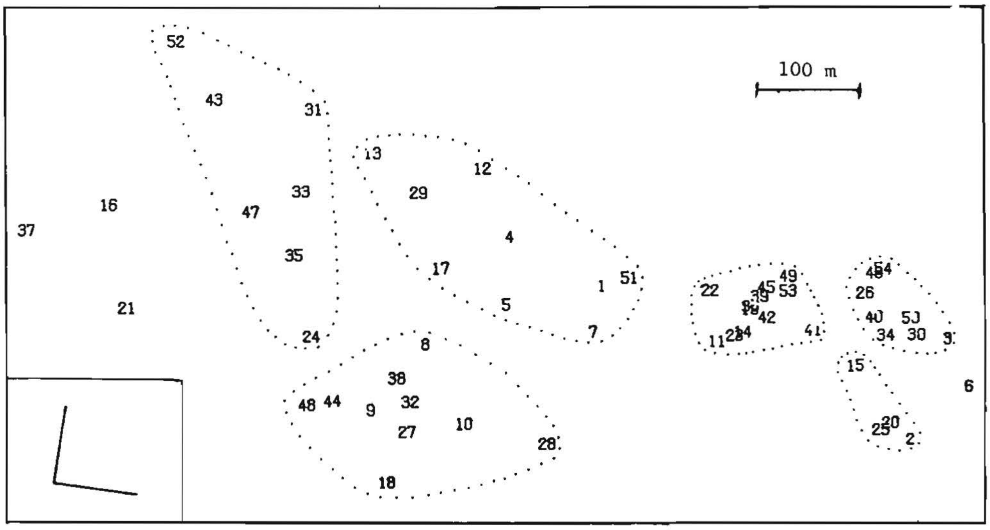


Figure 10e3. Positions of drogues used in gross-scale calculations for the end of experiment 320. Inset shows orientation of mean principal axes of diffusion. Dotted lines circumscribe clusters.

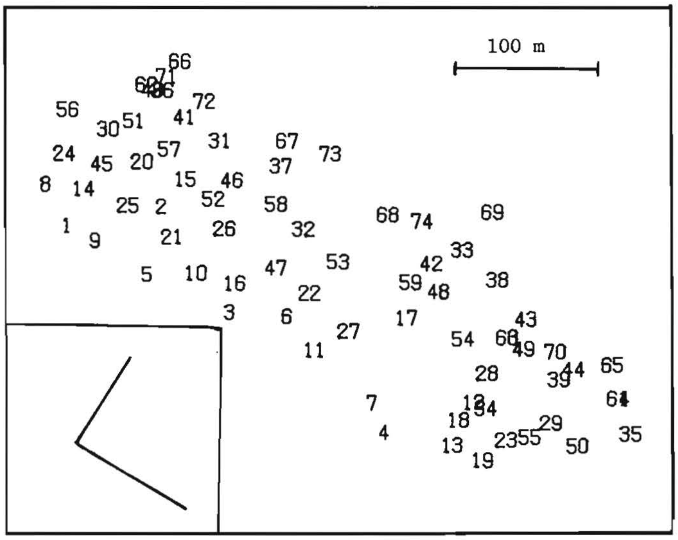


Figure 10f1. Positions of drogues used in gross-scale calculations for the beginning of experiment 520. Inset shows orientation of mean principal axes of diffusion.

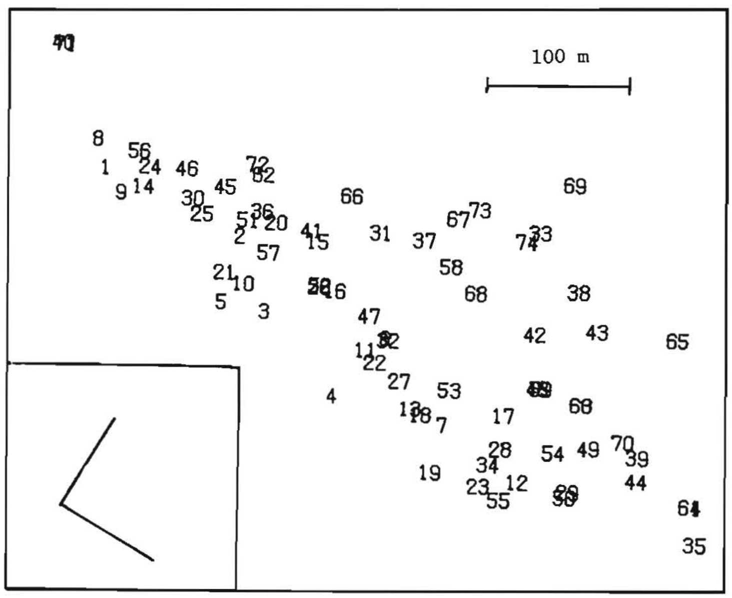


Figure 10f2. Positions of drogues used in gross-scale calculations for the middle of experiment 520. Inset shows orientation of mean principal axes of diffusion.

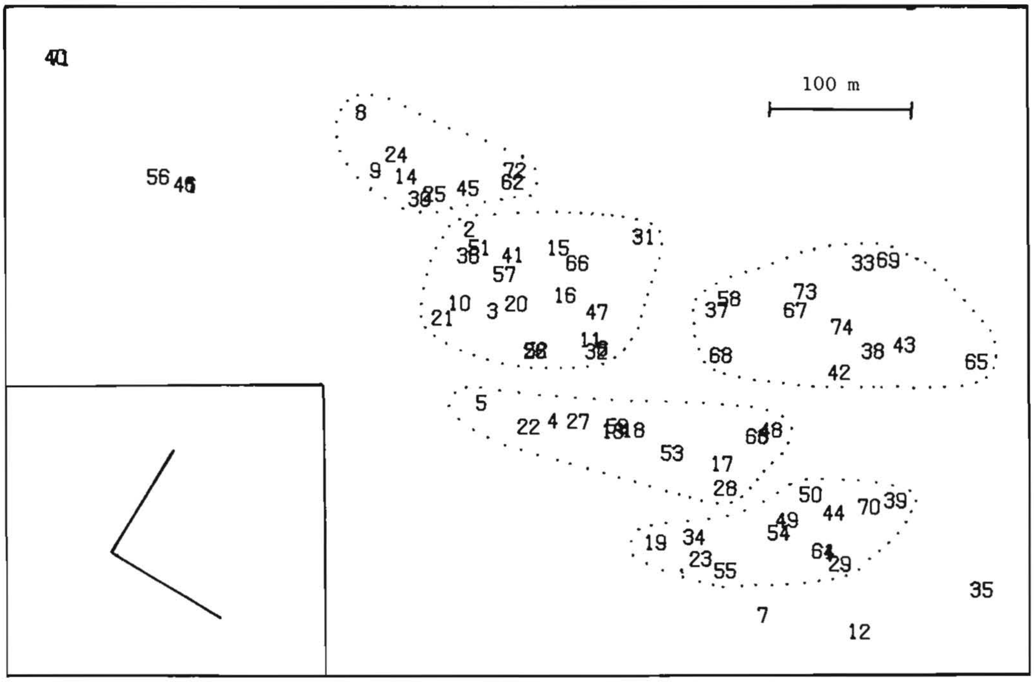


Figure 10f3. Positions of drogues used in gross-scale calculations for the end of experiment 520. Inset shows orientation of mean principal axes of diffusion. Dotted lines circumscribe clusters.

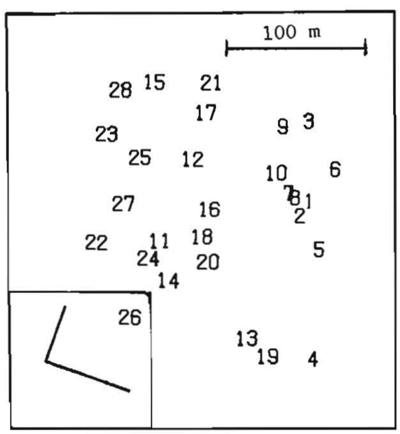


Figure 10g1. Positions of drogues used in gross-scale calculations for the beginning of experiment 605. Inset shows orientation of mean principal axes of diffusion.

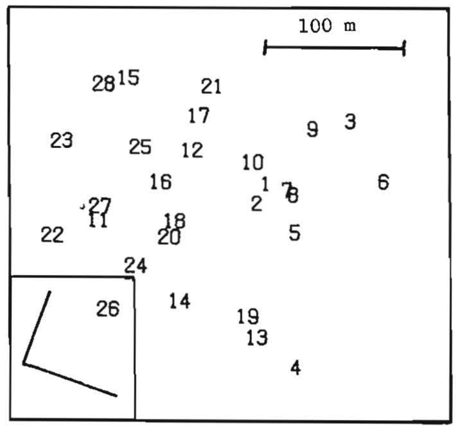


Figure 10g2. Positions of drogues used in gross-scale calculations for the middle of experiment 605. Inset shows orientation of mean principal axes of diffusion.

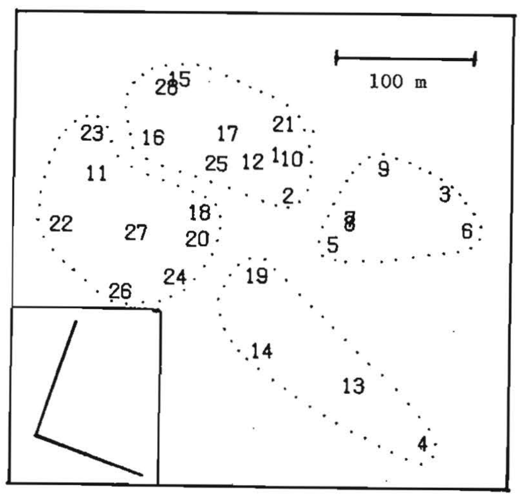


Figure 10g3. Positions of drogues used in gross-scale calculations for the end of experiment 605. Inset shows orientation of mean principal axes of diffusion. Dotted lines circumscribe clusters.

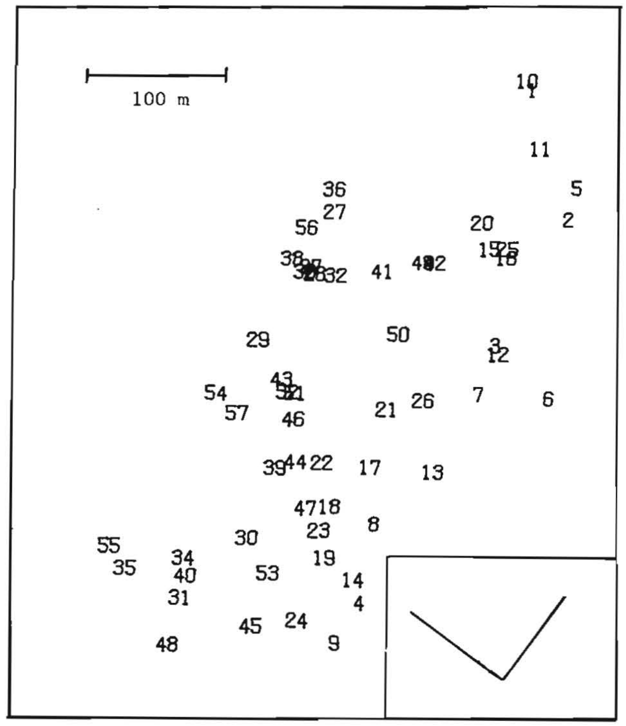


Figure 10h1. Positions of drogues used in gross-scale calculations for the beginning of experiment 620. Inset shows the orientation of mean principal axes of diffusion.

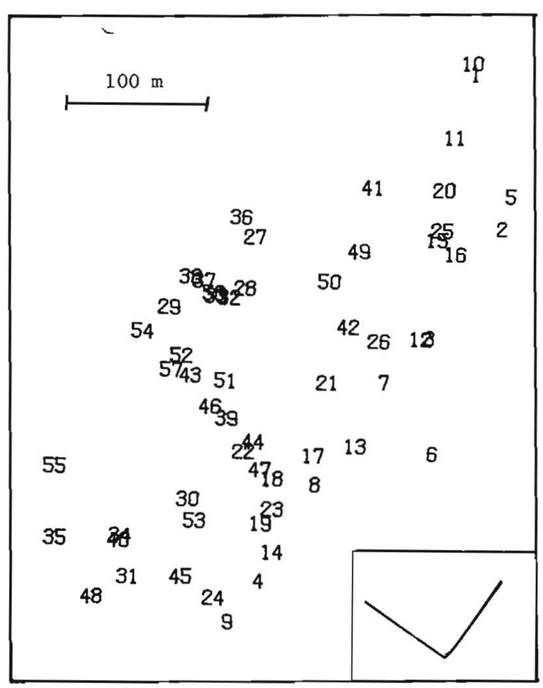


Figure 10h2. Positions of drogues used in gross-scale calculations for the middle of experiment 620. Inset shows orientation of mean principal axes of diffusion.

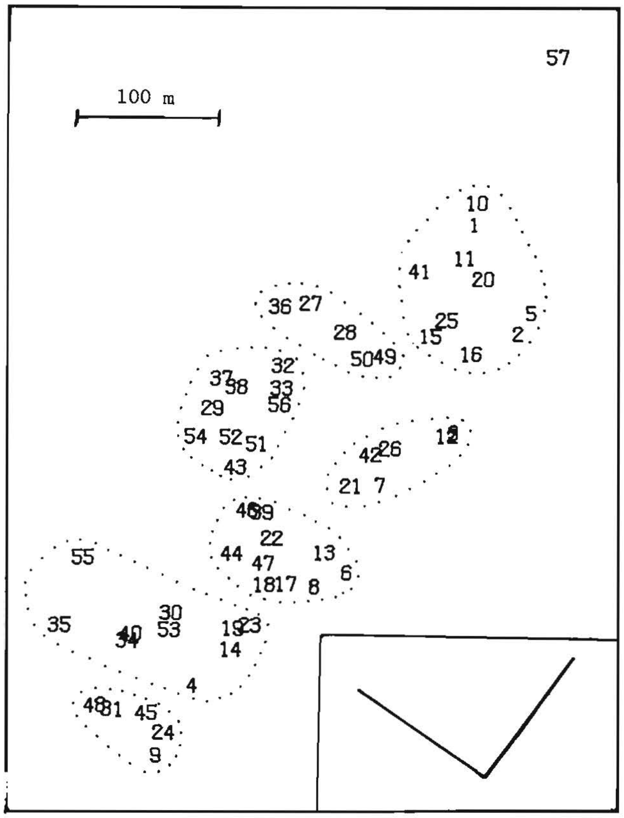


Figure 10h3. Positions of drogues used in gross-scale calculations for the end of experiment 620. Inset shows the orientation of mean principal axes of diffusion. Dotted lines circumscribe clusters.

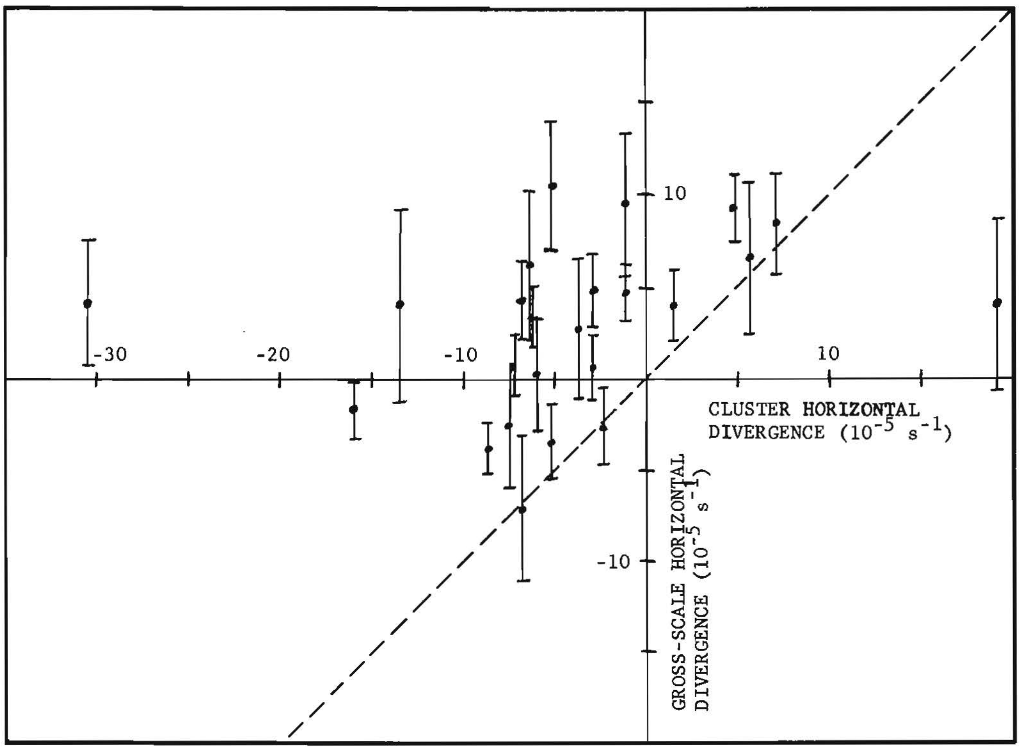


Figure 11a. Gross-scale horizontal divergence versus corresponding mean values for the clusters. Note that 95% confidence limits (bars) for 5 out of 24 values intersect the 45° line (dashed), and 13 out of 24 values lie in the upper left quadrant indicating that clusters tend to contract while gross-scales expand.

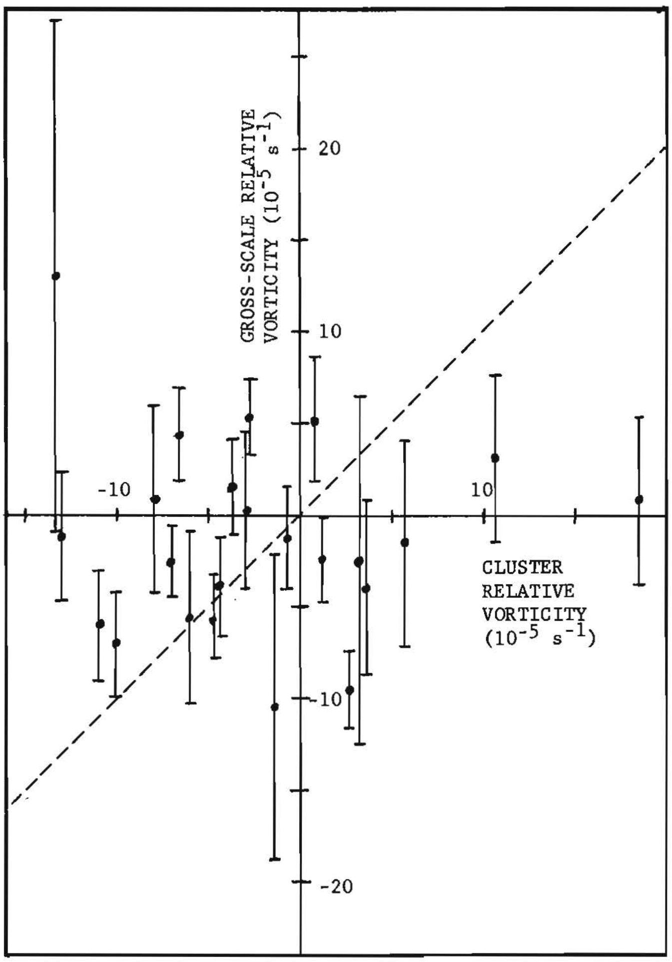


Figure 11b. Gross-scale relative vorticity versus corresponding mean values for clusters. Note that 95% confidence limits (bars) for 6 out of 24 (8 experiments x 3 sampling times) values intersect the $45^{o}$ line (dashed).

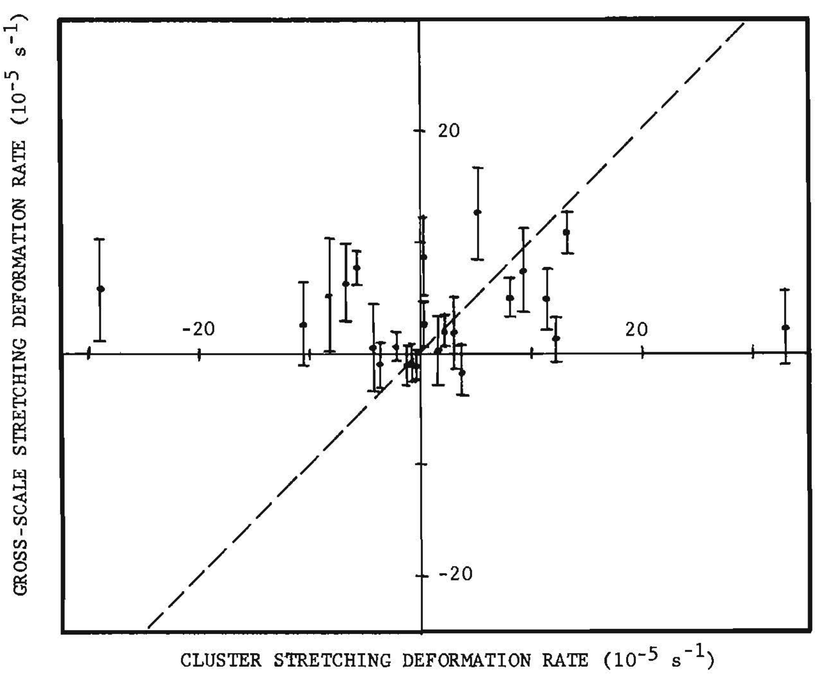


Figure 11c. Gross-scale stretching deformation rate versus corresponding mean values for clusters. Note that 95% confidence limits (bars) for 7 out of 24 values intersect the 45° line (dashed).

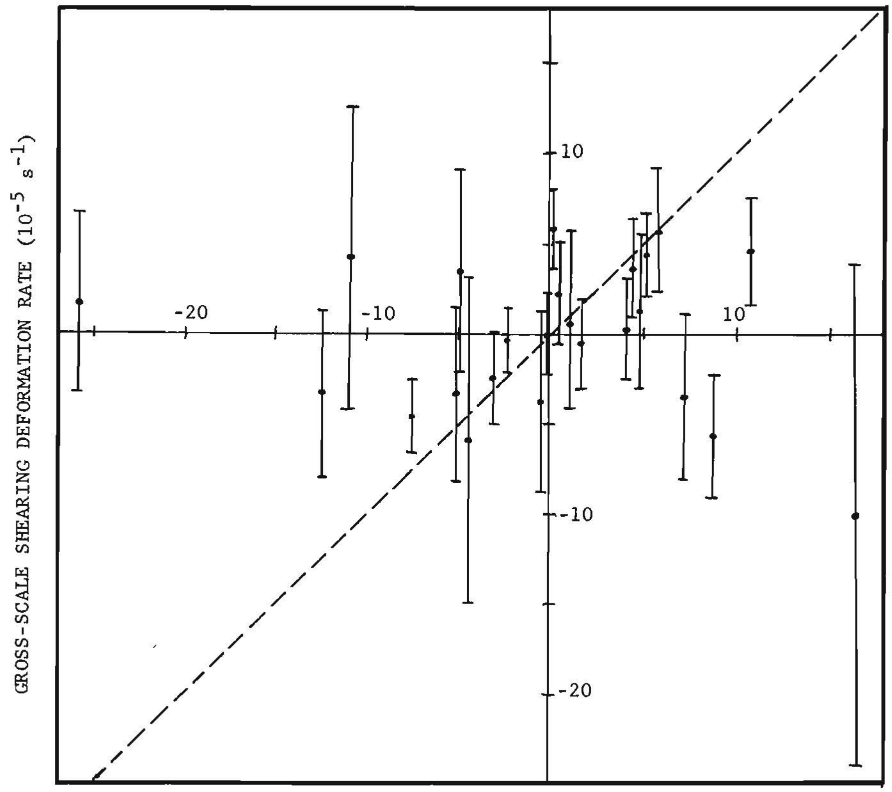


Figure 11d. Gross-scale shearing deformation rate versus corresponding mean values for clusters. Note that 95% confidence limits (bars) for 12 out of 24 values intersect the 45° line (dashed).

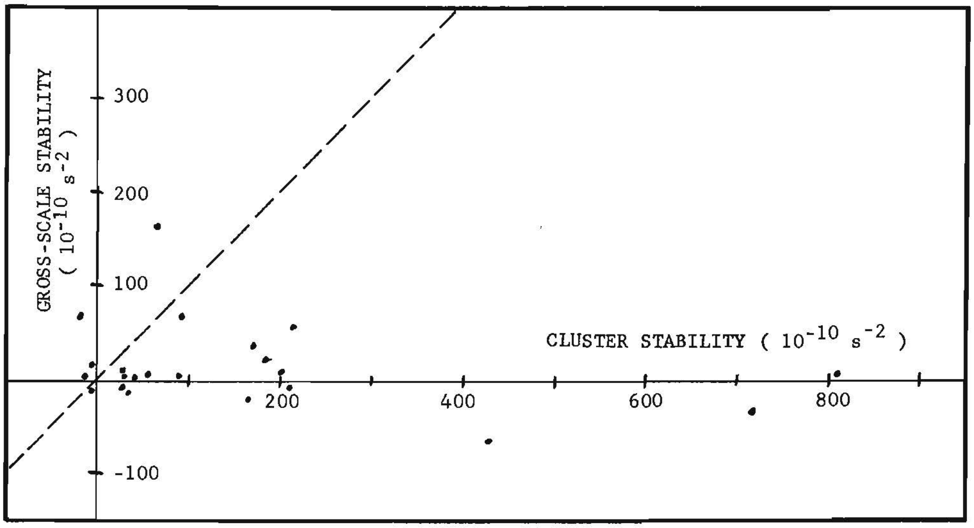


Figure 11e. Gross-scale stability versus corresponding mean values for clusters. The 45° line is dashed.

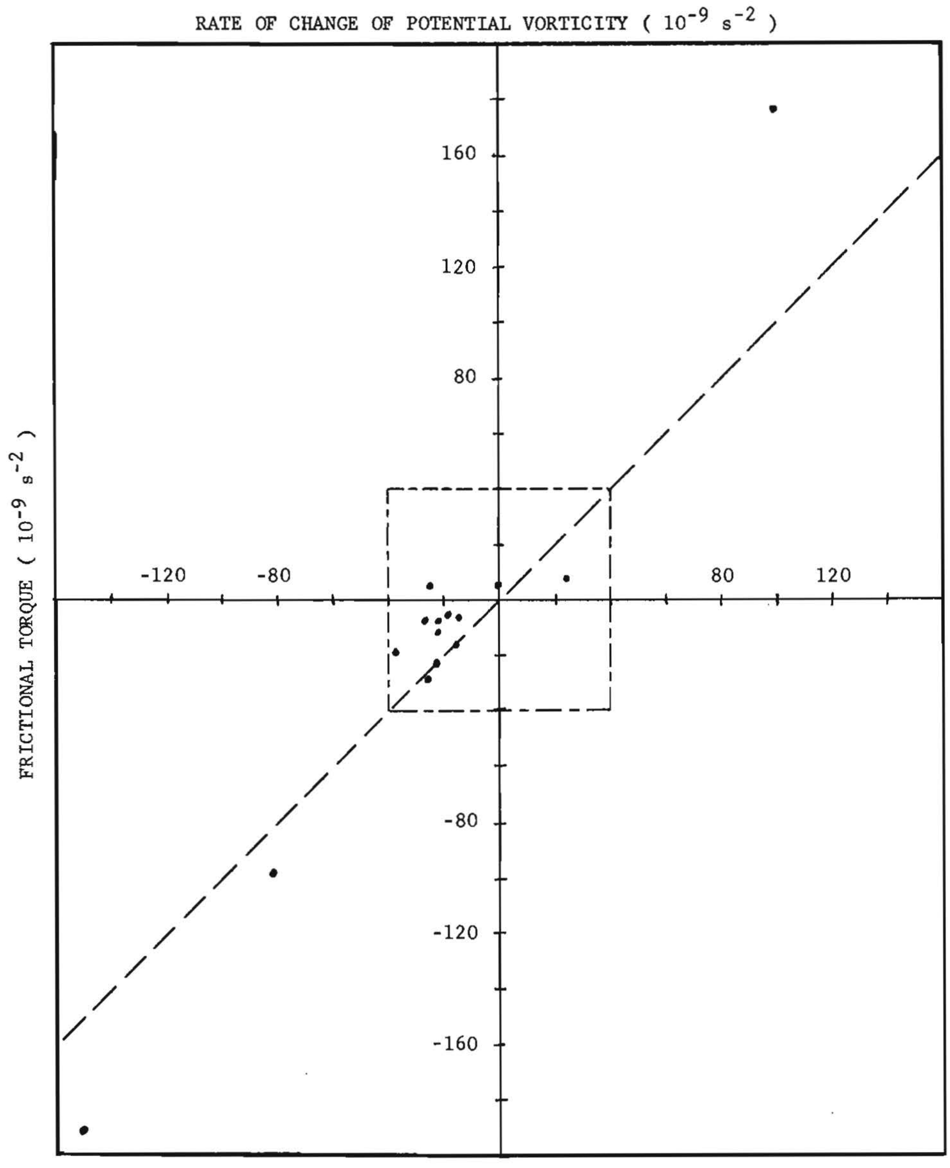


Figure 12a. Vorticity balance within clusters (•) for experiment 120. Shorter dashes approximately circumscribe vorticity balance of gross-scale drogue groups. Longer dashes indicates a balance of frictional torque and rate of change of potential vorticity.

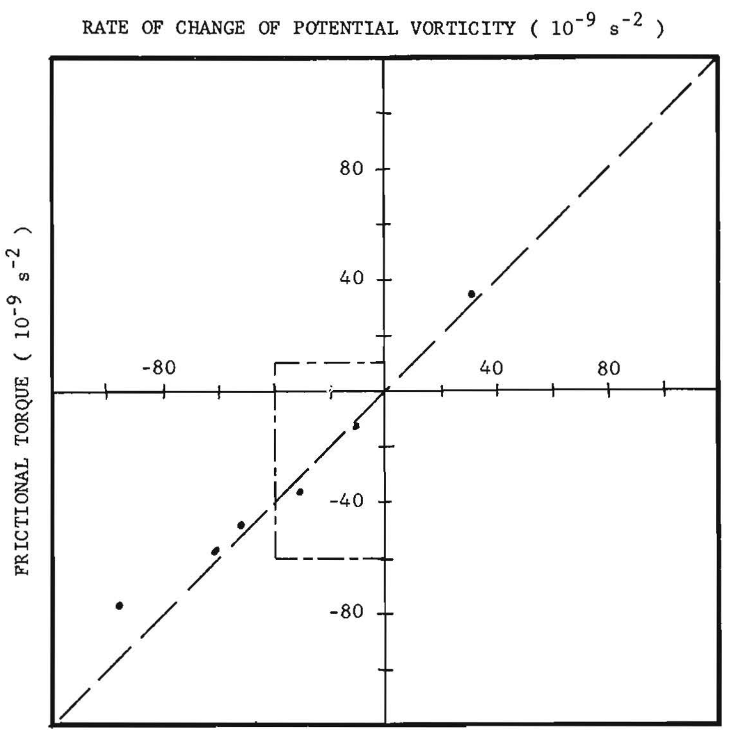


Figure 12b. Vorticity balance within clusters (•) for experiment 205. Shorter dashes approximately circumscribe vorticity balance of gross-scale drogue groups. Longer dashes indicates a balance of frictional torque and rate of change of potential vorticity.

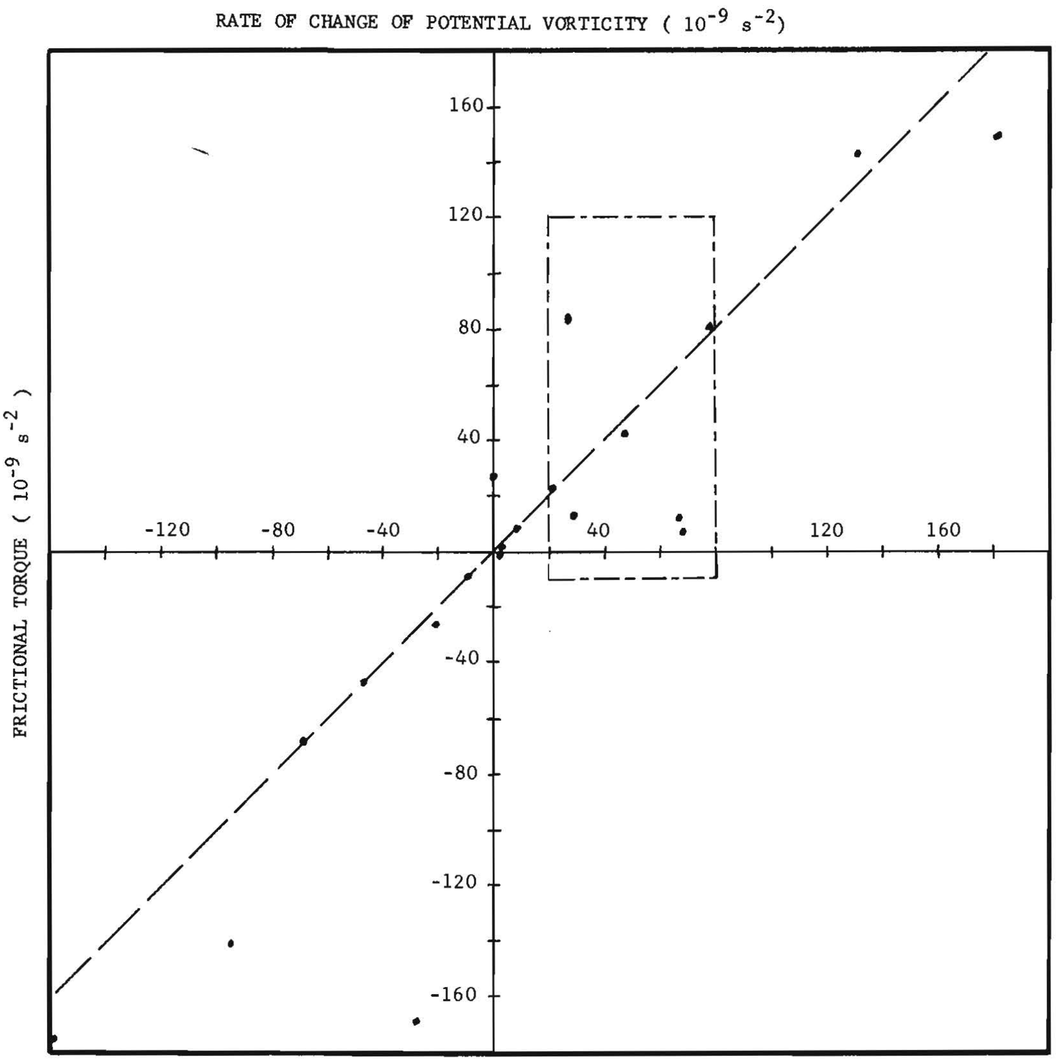


Figure 12c. Vorticity balance within clusters (•) for experiment 220. Shorter dashes approximately circumscribe vorticity balance of gross-scale drogue groups. Longer dashes indicates a balance of frictional torque and rate of change of potential vorticity.

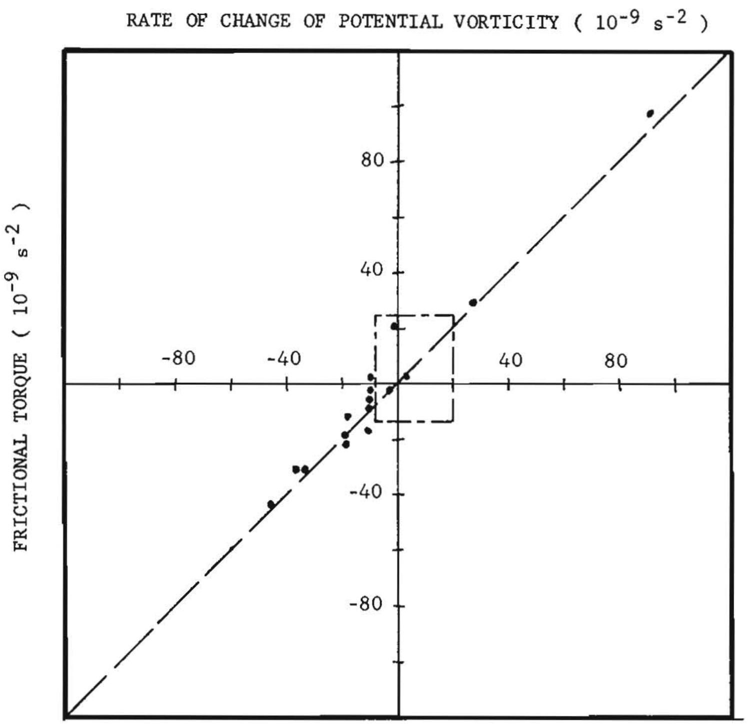


Figure 12d. Vorticity balance within clusters (•) for experiment 305. Shorter dashes approximately circumscribe vorticity balance of gross-scale drogue groups. Longer dashes indicates a balance of frictional torque and rate of change of potential vorticity.

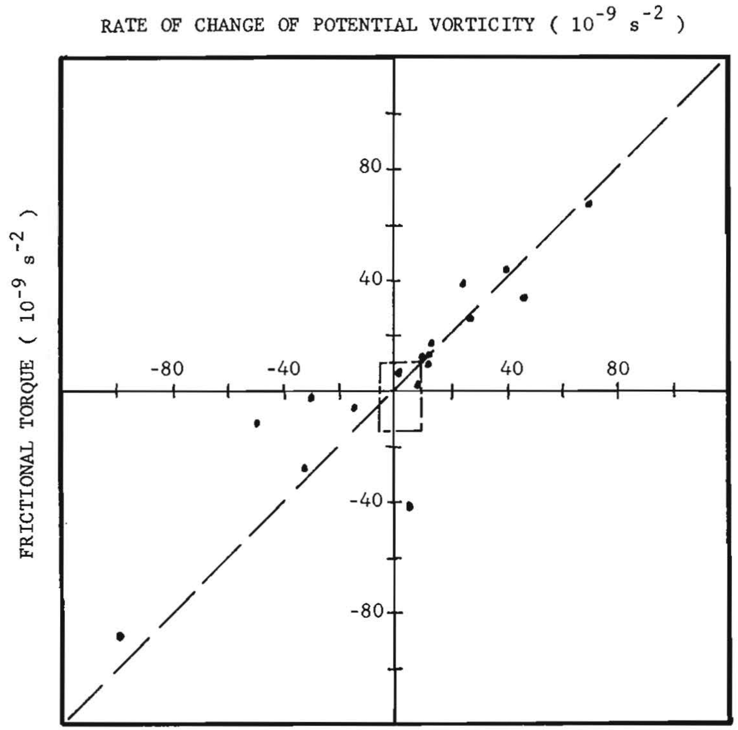


Figure 12e. Vorticity balance within clusters (•) for experiment 320. Shorter dashes approximately circumscribe vorticity balance of gross-scale drogue groups. Longer dashes indicates a balance of frictional torque and rate of change of potential vorticity.

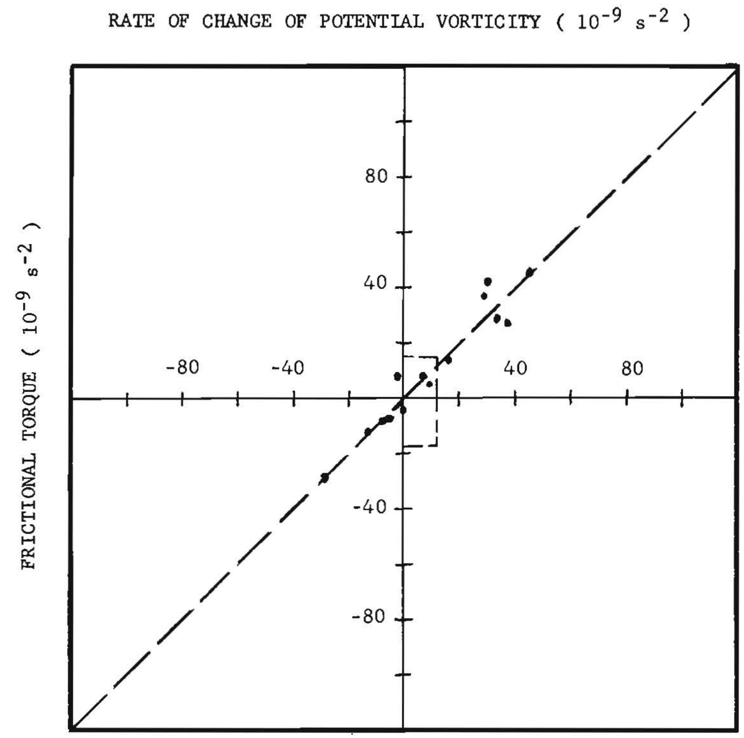


Figure 12f. Vorticity balance within clusters (•) for experiment 520. Shorter dashes approximately circumscribe vorticity balance of gross-scale drogue groups. Longer dashes indicates a balance of frictional torque and rate of change of potential vorticity.

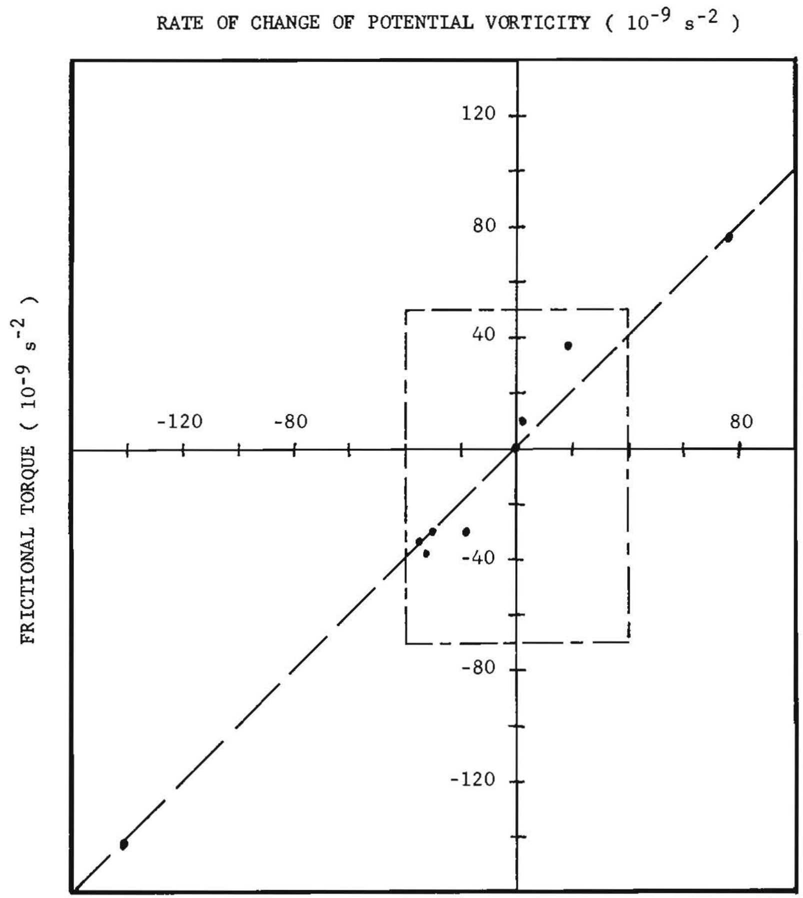


Figure 12g. Vorticity balance within clusters (•) for experiment 605. Shorter dashes approximately circumscribe vorticity balance of gross-scale drogue groups. Longer dashes indicates a balance of frictional torque and rate of change of potential vorticity.

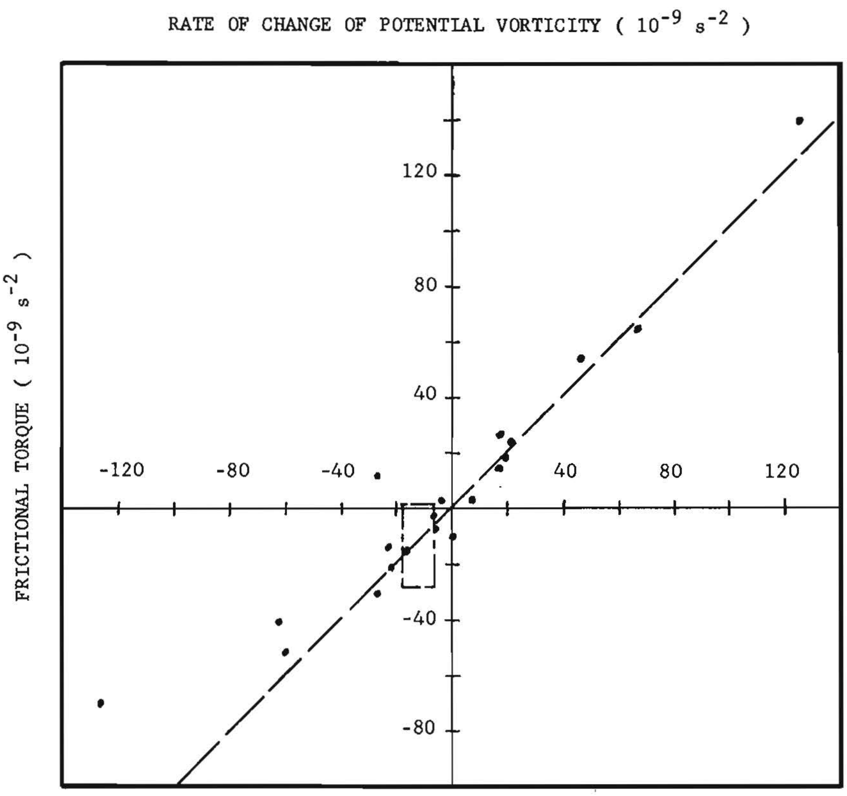


Figure 12h. Vorticity balance within clusters (•) for experiment 620. Shorter dashes approximately circumscribe vorticity balance of gross-scale drogue groups. Longer dashes indicates a balance of frictional torque and rate of change of potential vorticity.

Table 6. Comparison of turbulent displacement and speed and eddy diffusivities between gross-scale (G) and cluster averages (C). G values are time averages for each experiment. C averages contain beginning, middle and end times.

| Experiment designation | No. of cluster values | Standard deviation of turbulent displacement $r''$ (m) | | Standard deviation of turbulent speed $s''$ (cm $s^{-1}$) | | Momentary eddy diffusivity $K(10^2\ cm^2\ s^{-1})$ | |
|---|---|---|---|---|---|---|---|
| | | G | C | G | C | G | C |
| 120 | 15 | 7.92 | 3.18 | 1.06 | .434 | 3.13 | .708 |
| 205 | 6 | 4.38 | 3.41 | .545 | .434 | .932 | .482 |
| 220 | 24 | 12.1 | 2.69 | 1.61 | .359 | 3.62 | .933 |
| 305 | 15 | 5.65 | 3.42 | .792 | .466 | 2.23 | 1.05 |
| 320 | 18 | 5.77 | 3.41 | .791 | .464 | 2.02 | .728 |
| 520 | 15 | 4.58 | 2.19 | .626 | .306 | 1.26 | .397 |
| 605 | 12 | 4.90 | 2.24 | .640 | .300 | 1.27 | .244 |
| 620 | 21 | 3.38 | 1.92 | .453 | .261 | .676 | .217 |
| Average | 16 | 6.09 | 2.81 | .815 | .378 | 1.89 | .595 |

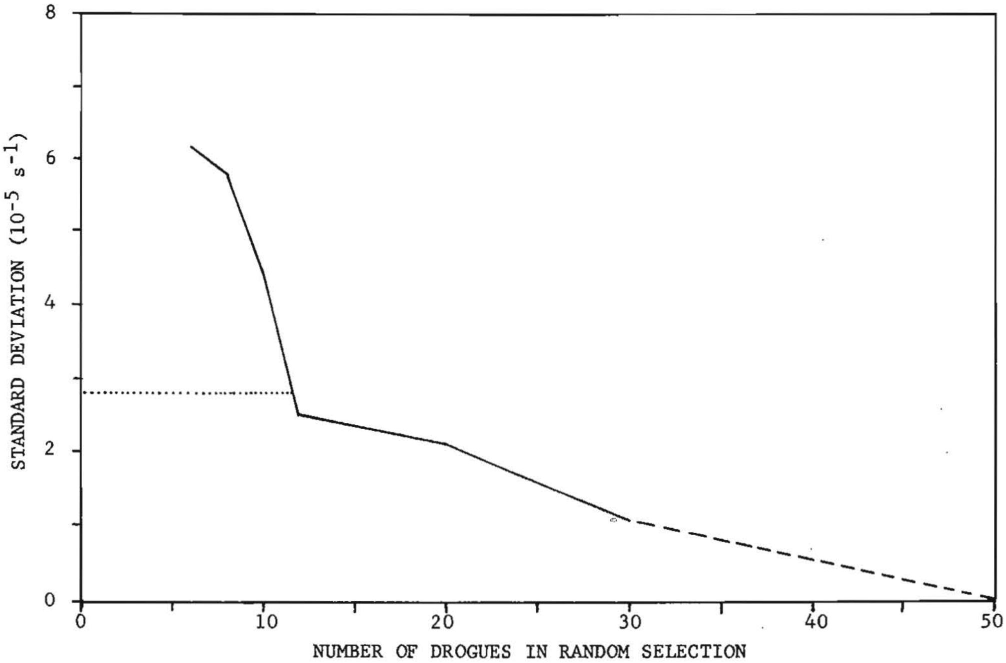


Figure 13a. Standard deviation of difference of horizontal divergence. Difference is taken between values corresponding to random selection and gross-scale. Dotted line corresponds to the average 95% confidence limits of gross-scale values.

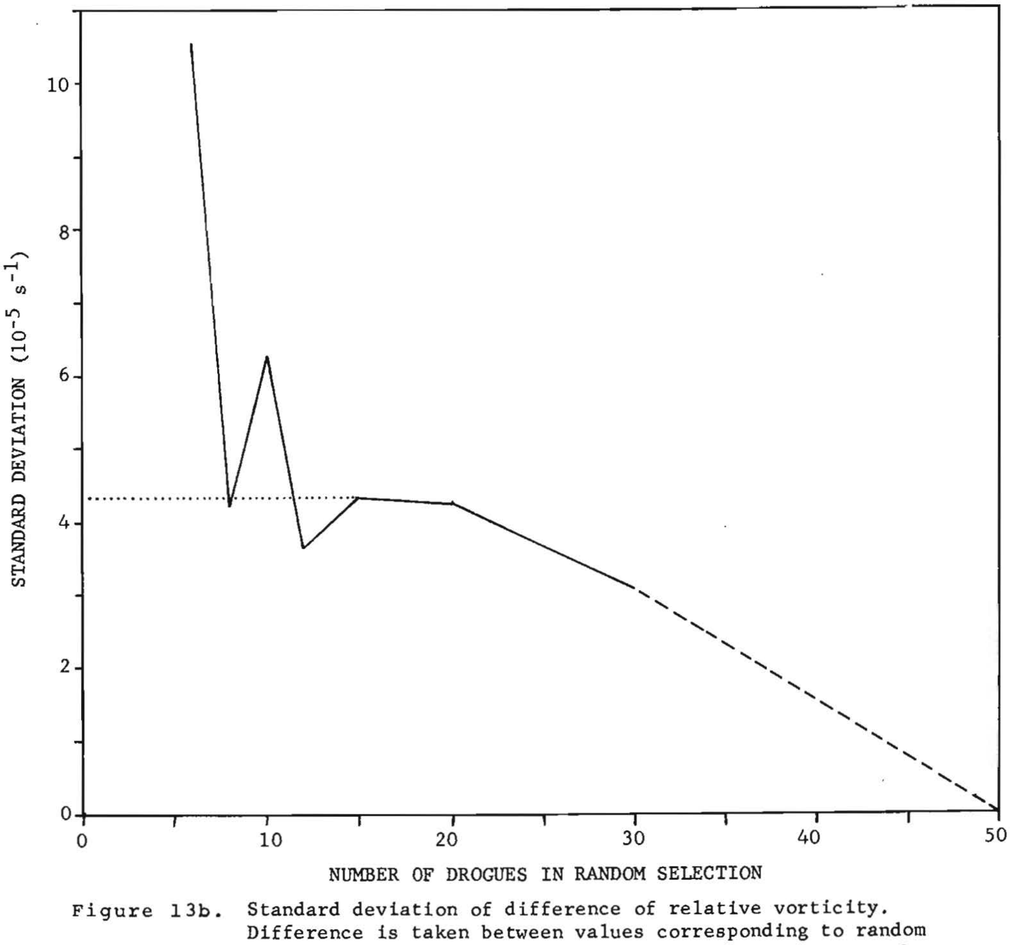


Figure 13b. Standard deviation of difference of relative vorticity. Difference is taken between values corresponding to random selection and gross-scale. Dotted line corresponds to the average 95% confidence limits of gross-scale values.

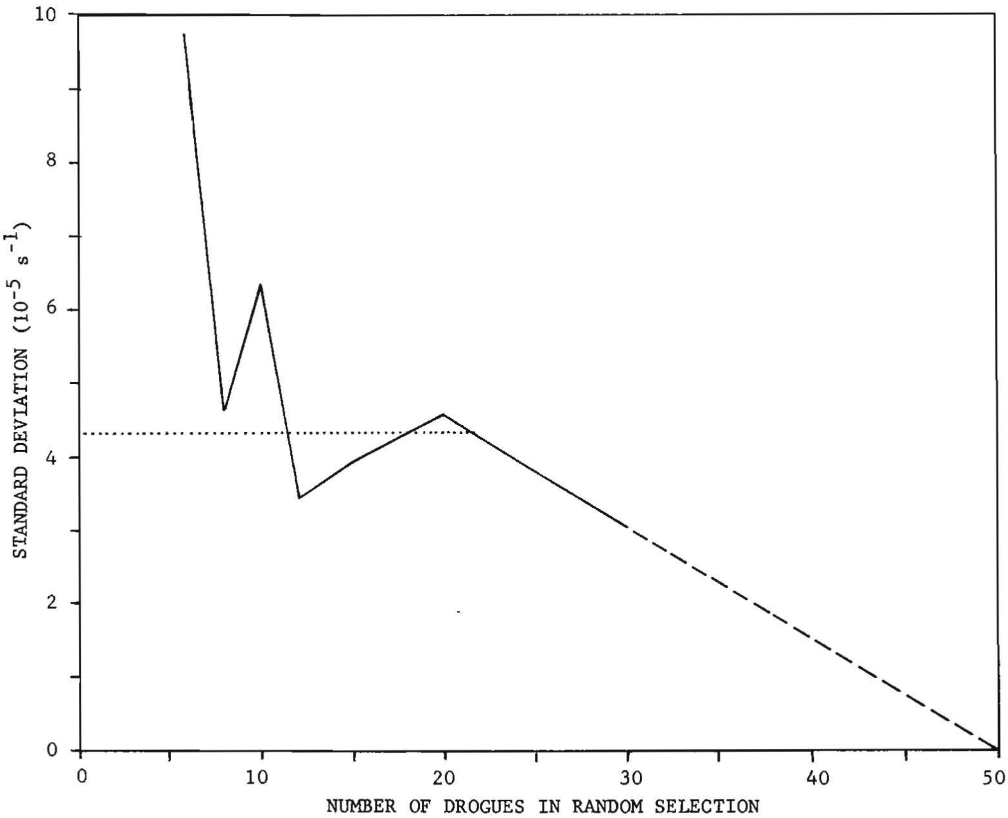


Figure 13c. Standard deviation of difference of shearing deformation rate. Difference is taken between values corresponding to random selection and gross-scale. Dotted line corresponds to the average 95% confidence limits of gross-scale values.

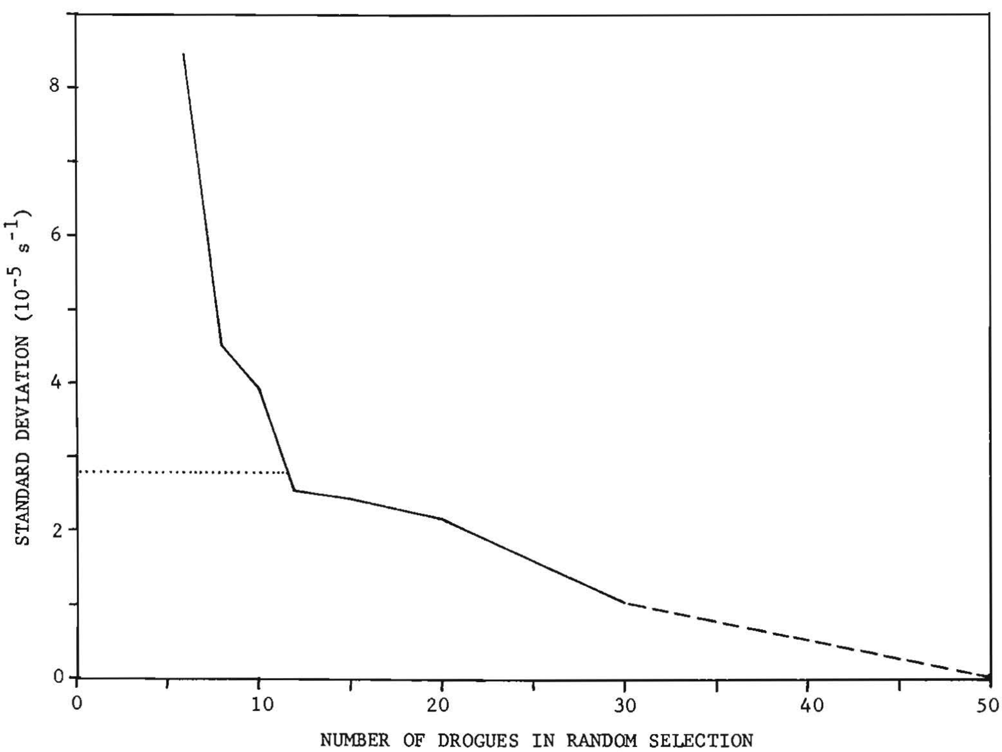


Figure 13d. Standard deviation of difference of stretching deformation rate. Difference is taken between values corresponding to random selection and gross-scale. Dotted line corresponds to the average 95% confidence limits of gross-scale values.

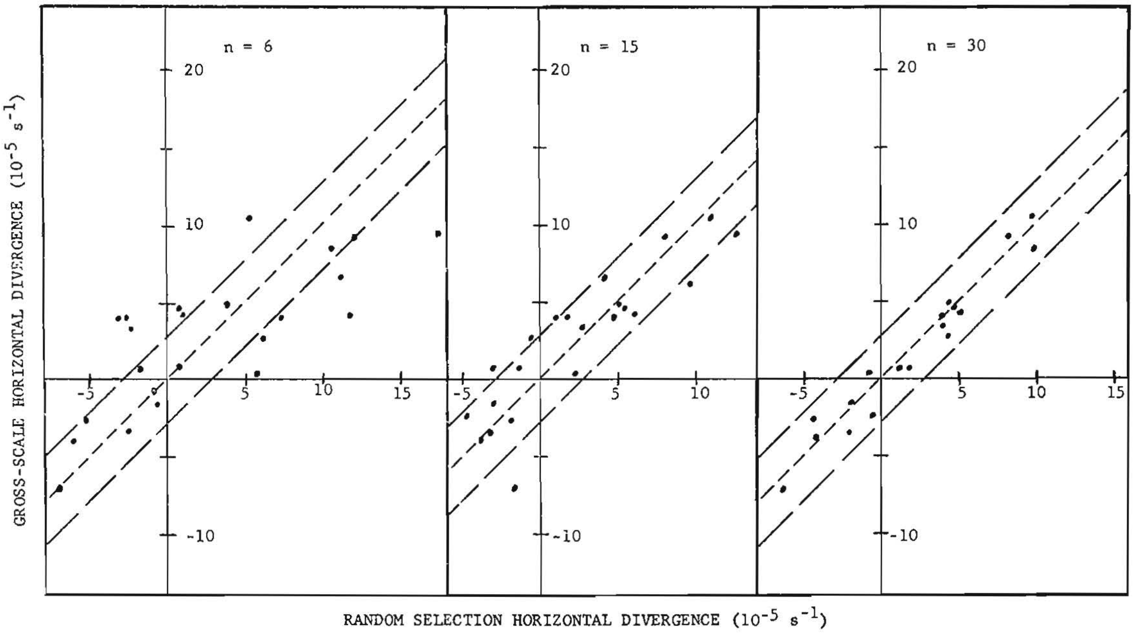


Figure 14a. Gross-scale horizontal divergence versus corresponding values for random selections of n = 6, 15, and 30 drogues. The 45° line (smaller dashes) represents equality. Longer dashes correspond to mean 95% confidence limits of the gross-scale values.

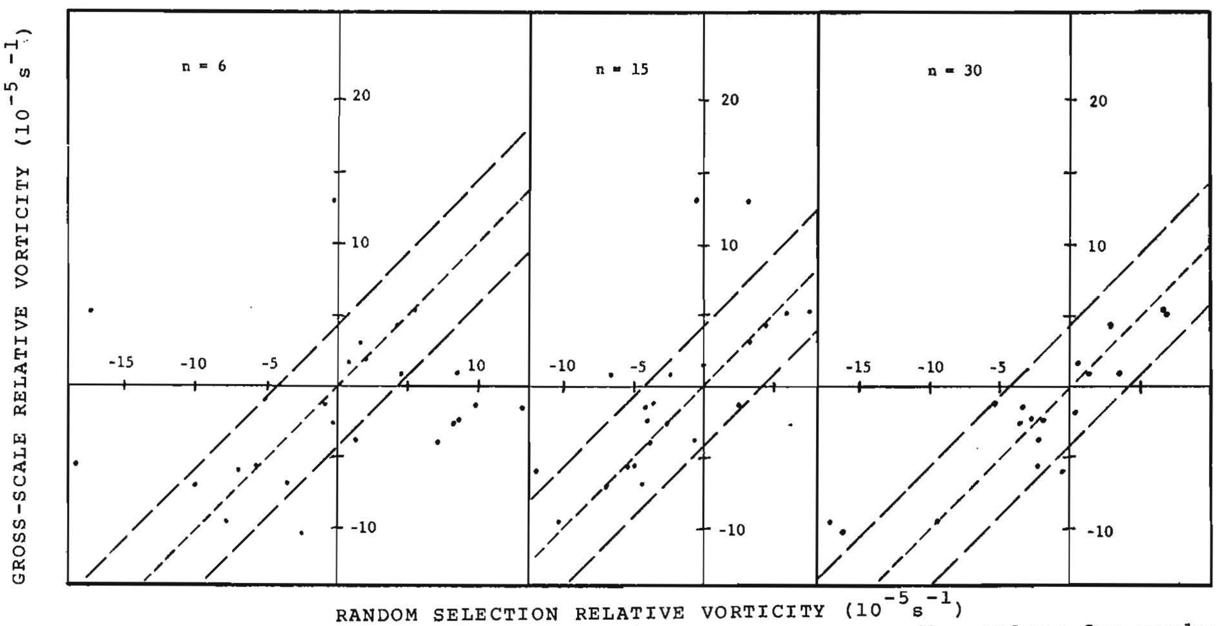


Figure 14b. Gross-scale relative vorticity versus corresponding values for random selections n=6, 15, and 30 drogues. The 45° line (smaller dashes) represents equality. Longer dashes correspond to mean 95% confidence limits of the gross-scale values.

drogues without significantly altering the results of the gross-scale calculations. However, smaller-scale variability would have been more difficult to examine.

# CHAPTER 5
# TIME DEPENDENT ADVECTION-DIFFUSION MODEL

## 5.1 *Advection-diffusion equation and its Lagrangian form*

Heterogeneity in currents, i.e. velocity gradients, plays a crucial role in dispersing a batch of drogues as studied in other regions by Ebbesmeyer and Helseth (1975) and Molinari and Kirwan (1975). In the previous chapters we have shown that current shears, assumed uniform within batches, are highly variable in time and appear to primarily control their dispersion. We can study the shear effect more quantitatively using an advection-diffusion equation.

Okubo (1966) noted that the Lagrangian form of the advection-diffusion equation is mathematically more tractable than the original Eulerian form. He dealt with a case of constant velocity gradients and eddy diffusivities. However, a generalized advection-diffusion equation with time variable velocity gradients and eddy diffusivities can still be solved analytically replacing time variable velocity-gradient parameters by their time variable Lagrangian counterparts: Lagrangian deformations.

The detail of deriving the Lagrangian form of the advection-diffusion equation should be consulted with Ebbesmeyer, Okubo, Helseth and Robbins (1976), henceforth abbreviated EOHR. Only the resultant equation is presented here:

$$\frac{\partial S}{\partial t} + (g_{11}+g_{22})S = J^{-2}\left\{K_{11}\left[e_{22}^2\frac{\partial^2 S}{\partial a^2} - 2e_{21}e_{22}\frac{\partial^2 S}{\partial a\partial b} + e_{21}^2\frac{\partial^2 S}{\partial b^2}\right] - (K_{12}+K_{21})\left[e_{12}e_{22}\frac{\partial^2 S}{\partial a^2}\right.\right.$$
$$\left.\left. -(e_{11}e_{22}+e_{12}e_{21})\frac{\partial^2 S}{\partial a\partial b} + e_{11}e_{21}\frac{\partial^2 S}{\partial b^2}\right] + K_{22}\left[e_{12}^2\frac{\partial^2 S}{\partial a^2} - 2e_{11}e_{12}\frac{\partial^2 S}{\partial a\partial b} + e_{11}^2\frac{\partial^2 S}{\partial b^2}\right]\right\} \tag{16}$$

where $S(t, a, b)$: concentration expressed in Lagrangian coordinates $(a,b)$, $t$: time, $g_{11}(t) + g_{22}(t)$: horizontal divergence, $e_{ij}(t)$: Lagrangian deformations with respect to initial positions $(a,b)$, $J(t) \equiv e_{11}e_{22}-e_{12}e_{21}$, $K_{ij}(t)$: momentary eddy diffusion coefficients. Note that (16) is reduced to the Lagrangian diffusion equation given by Corrsin (1962) and Okubo (1966) when $g_{11} + g_{22} = 0$, $J=1$ (incompressible), $K_{11} = K_{22} = A$(constant), and $K_{12} = K_{21} = 0$. Thus (16) is a generalized Lagrangian diffusion equation for anisotropic, time-variable diffusion in a compressible flow with spatially uniform, time-variable, deformations.

Note that $K_{ij}$ differ somewhat from momentary eddy diffusivities $K_x$, $K_y$ defined in Section 3.5. For detail see EOHR. The OEH provides a method for computing $K_{ij}$ as well as $e_{ij}$ directly from drogue positions.

## 5.2 *Solution of time dependent advection-diffusion equation*

The Lagrangian equation (16) can be solved analytically under an initial condition for a Gaussian patch, i.e. the concentration distribution is Gaussian, and the solution can then be transformed back into Eulerian form. The EOHR gives details of the calculation. The result in standard form is:

$$S(t,X,Y) = (2\pi\sigma_X^2\sigma_Y^2)^{-1}\exp-\left(\frac{X^2}{2\sigma_X^2} + \frac{Y^2}{2\sigma_Y^2}\right) \tag{17}$$

where X, Y are the (momentary) major and minor principal axes of dispersion (Fig. 1) and the three primary characteristics of dispersion are:

1. Variance along the major principal axis:

$$\sigma_X^2(t) = B_1+B_3 + [(B_3-B_1)^2 + 4B_2^2]^{\frac{1}{2}}$$

2. Variance along the minor principal axis:

$$\sigma_Y^2(t) = B_1+B_3 - [(B_3-B_1)^2 + 4B_2^2]^{\frac{1}{2}}$$

3. Orientation of the principal axes:

$$\theta(t) = \tfrac{1}{2}\tan^{-1}[2B_2(B_3-B_1)^{-1}] \qquad (18)$$

where $\theta$ is taken with respect to orientation of the initial principal axes, and where

$$B = \underbrace{\tfrac{1}{2}PI}_{\text{Pure deformation}} + \underbrace{P\int_0^t Q(t')K(t')J^{-2}(t')dt'}_{\text{Deformation-diffusion 'effect'}} \qquad (19)$$

in which the following matrix definitions are used:

$$B = \begin{pmatrix} B_1 \\ B_2 \\ B_3 \end{pmatrix} \quad I = \begin{pmatrix} \sigma_{Y_0}^2 \\ \rho_0\sigma_{X_0}\sigma_{Y_0} \\ \sigma_{X_0}^2 \end{pmatrix} \quad K = \begin{pmatrix} K_{11} \\ \tfrac{1}{2}(K_{12}+K_{21}) \\ K_{22} \end{pmatrix} \quad P = \begin{pmatrix} e_{22}^2 & -2e_{12}e_{22} & e_{21}^2 \\ e_{12}e_{22}-(e_{11}e_{22}+e_{21}e_{12}) & e_{11}e_{21} \\ e_{12}^2 & -2e_{11}e_{12} & e_{11}^2 \end{pmatrix}$$

$$Q = \begin{pmatrix} e_{21}^2 & -2e_{11}e_{21} & e_{11}^2 \\ e_{21}e_{22}-(e_{11}e_{22}+e_{12}e_{21}) & e_{11}e_{12} \\ e_{22}^2 & -2e_{12}e_{22} & e_{12}^2 \end{pmatrix} \qquad (20)$$

where $\sigma_{x_0}^2$, $\sigma_{y_0}^2$, $\rho_0$ are the initial variance in x direction, initial variance in y direction and initial correlation coefficient, respectively.

The solution (17) of the generalized advection-diffusion has a quadratic form in X and Y. An initial Gaussian patch remains Gaussian; the contours of the concentration are a set of ellipses with common principal axes, whose orientation varies with time.

### 5.3 *Calculations of the characteristics of the advection-diffusion equation: comparison with drogue distribution*

From (17), (18), (19) and (20) we can evaluate some important characteristics of diffusion. They are drogue area $A(t) \equiv 4\pi\sigma_X\sigma_Y$, elongation $\varepsilon(t) \equiv \sigma_X/\sigma_Y$, orientation $\theta(t)$, among others. For these evaluations are used values of the Lagrangian deformations $e_{ij}(t)$ and momentary diffusion coefficients $K_{ij}(t)$ obtained by the OEH method.

Figure 15 compares calculated and observed characteristics. We conclude that the generalized advection-diffusion model provides good approximation to the dispersion characteristics of drogues.

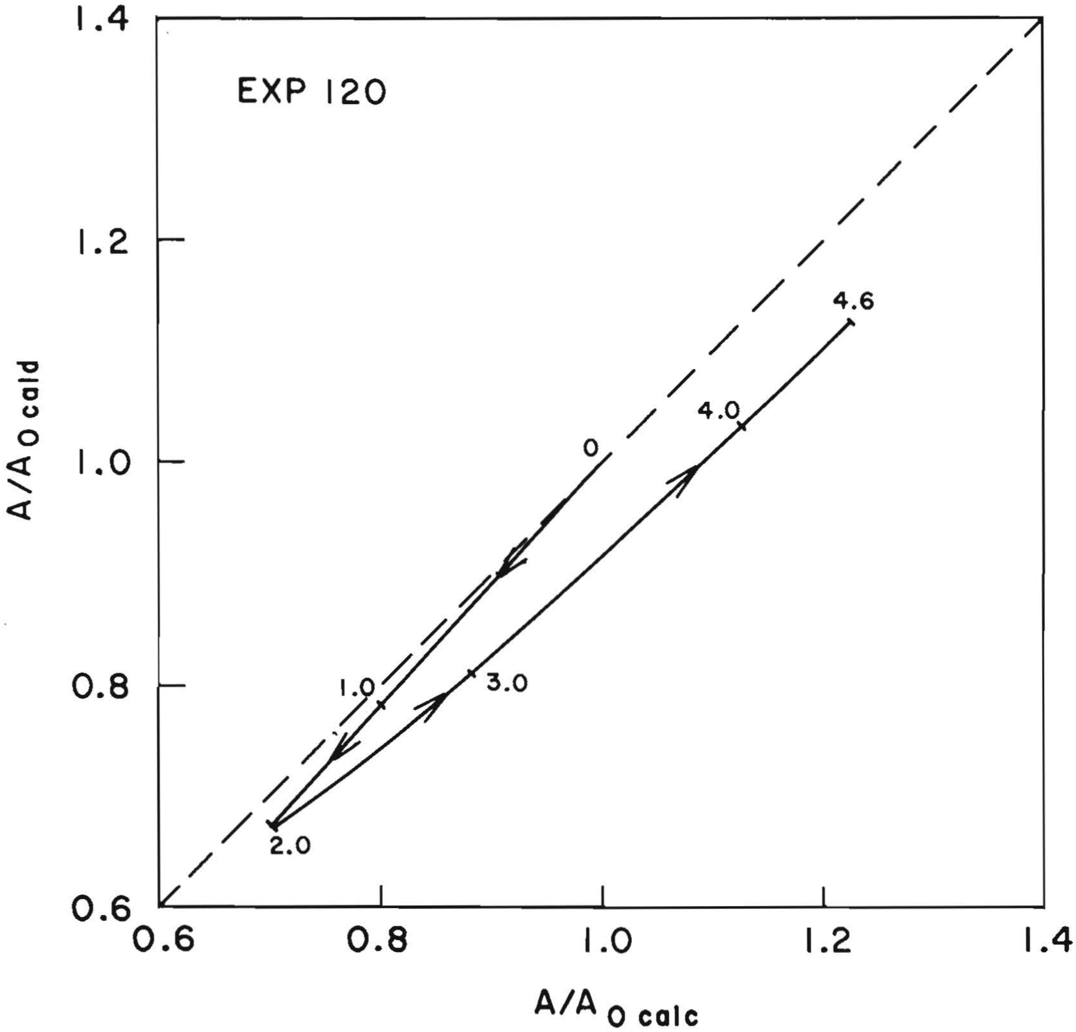


Fig. 15a 1. Comparison of calculated and observed drogue area for experiment 120. Numerals in the figure indicate the time in hours.

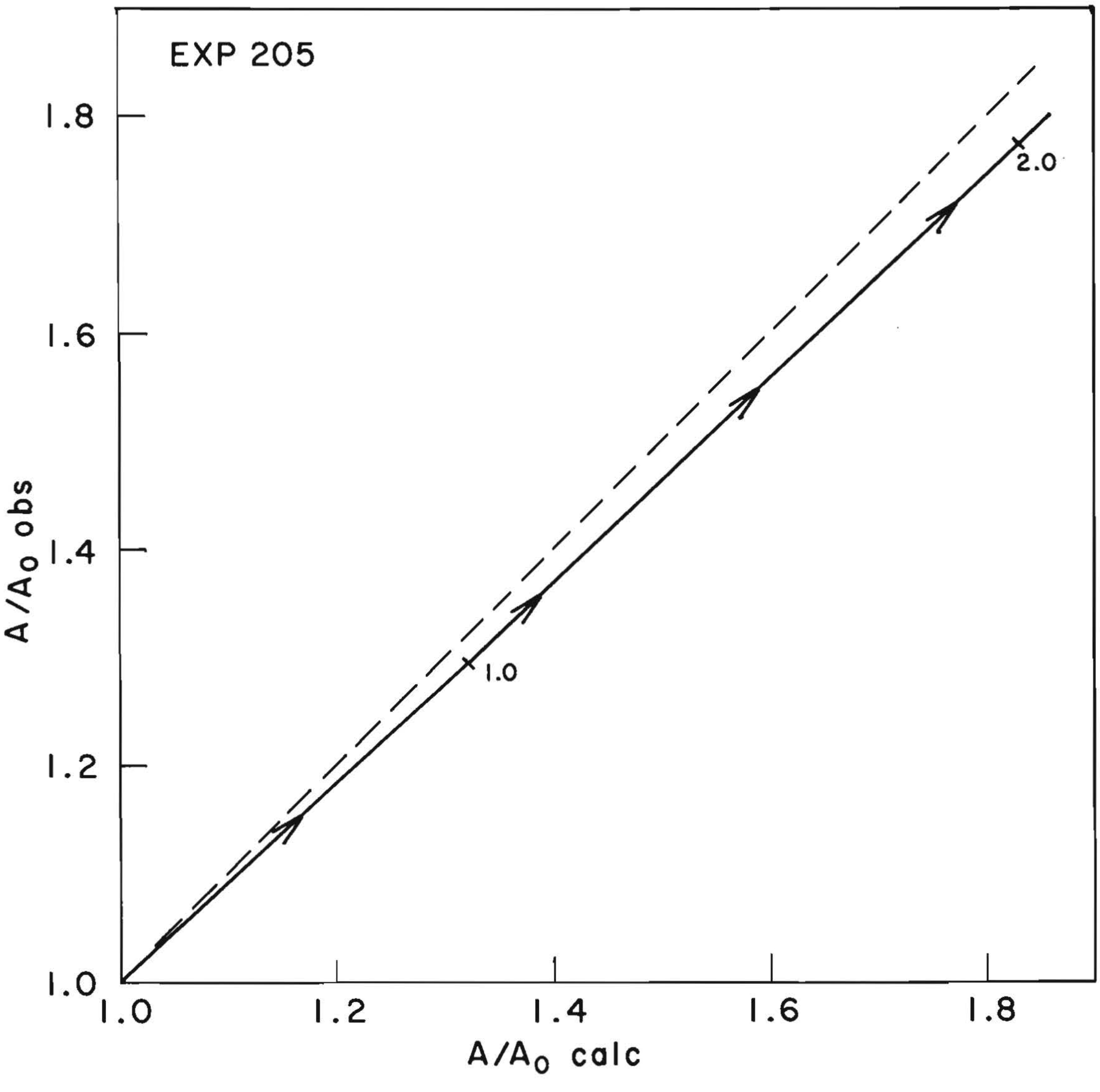


Fig. 15a 2. Comparison of calculated and observed drogue area for experiment 205. Numerals in the figure indicate the time in hours.

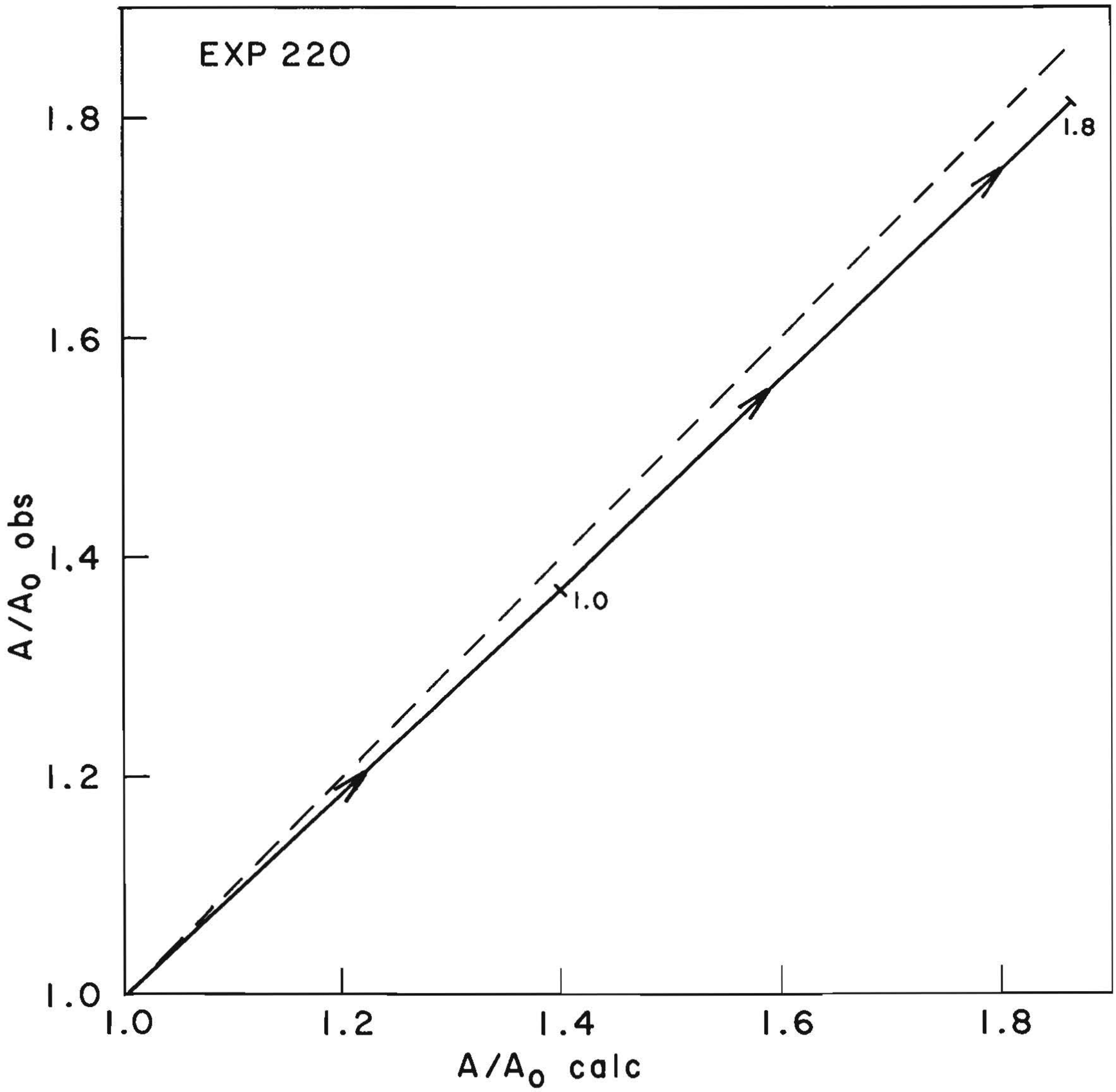


Fig. 15a 3. Comparison of calculated and observed drogue area for experiment 220. Numerals in the figure indicate the time in hours.

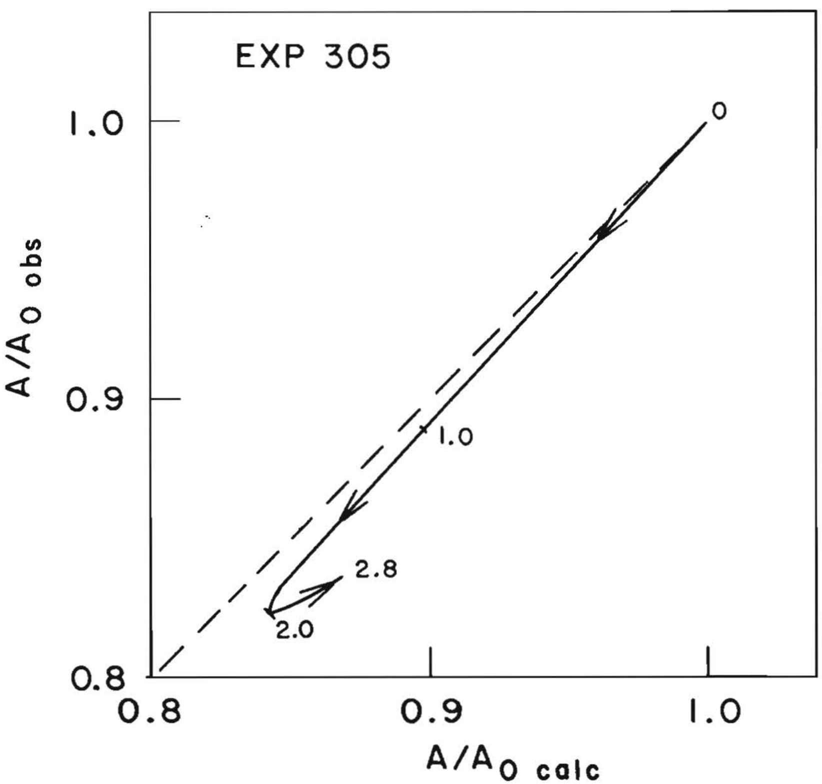


Fig. 15a 4. Comparison of calculated and observed drogue area for experiment 305. Numerals in the figure indicate the time in hours.

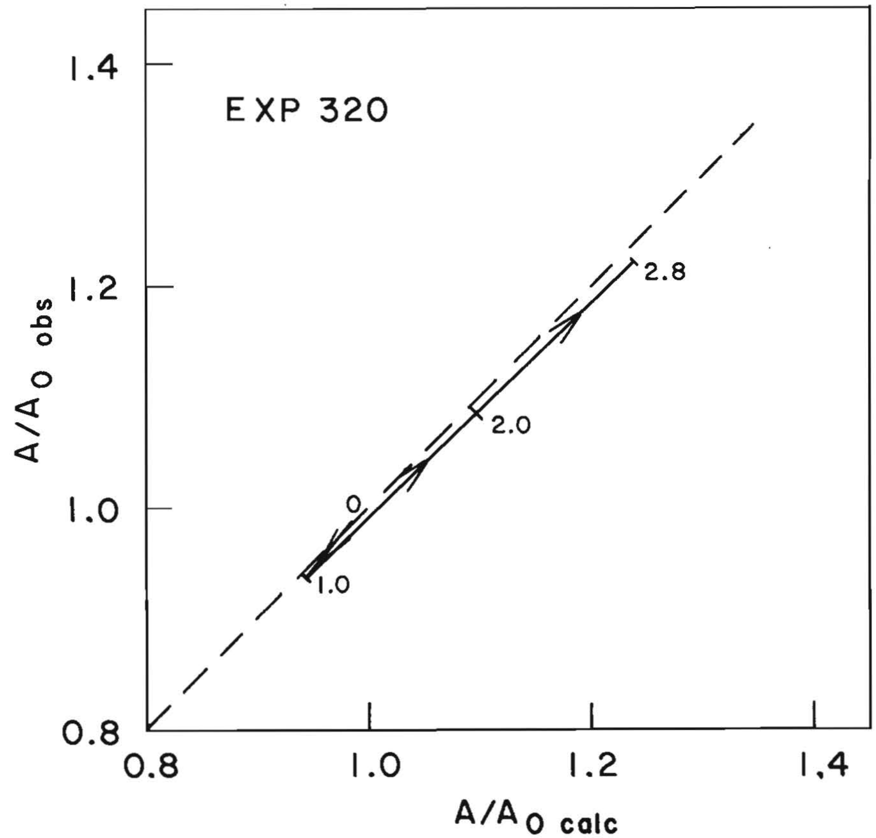


Fig. 15a 5. Comparison of calculated and observed drogue area for experiment 320. Numerals in the figure indicate the time in hours.

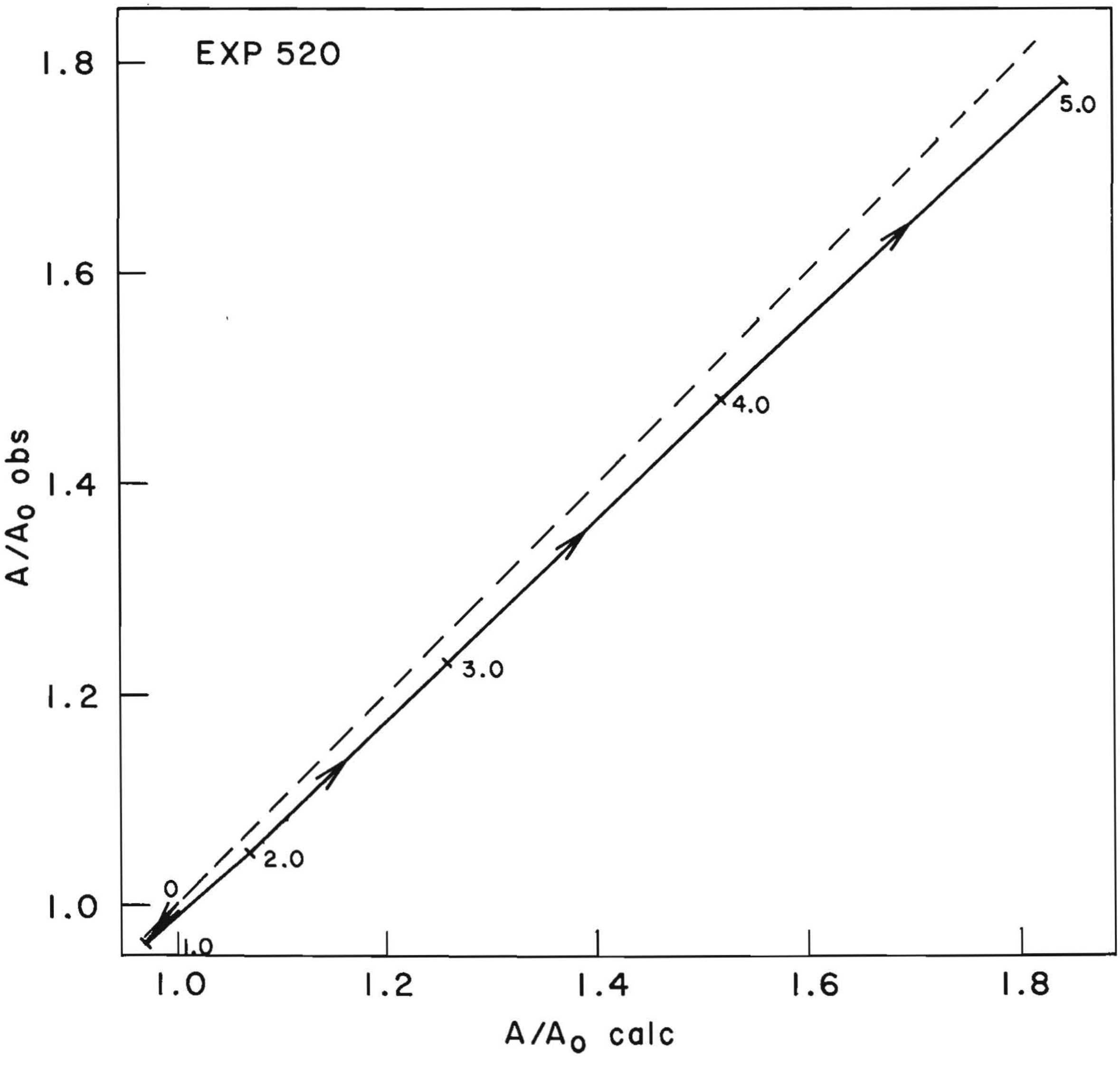


Fig. 15a 6. Comparison of calculated and observed drogue area for experiment 520. Numerals in the figure indicate the time in hours.

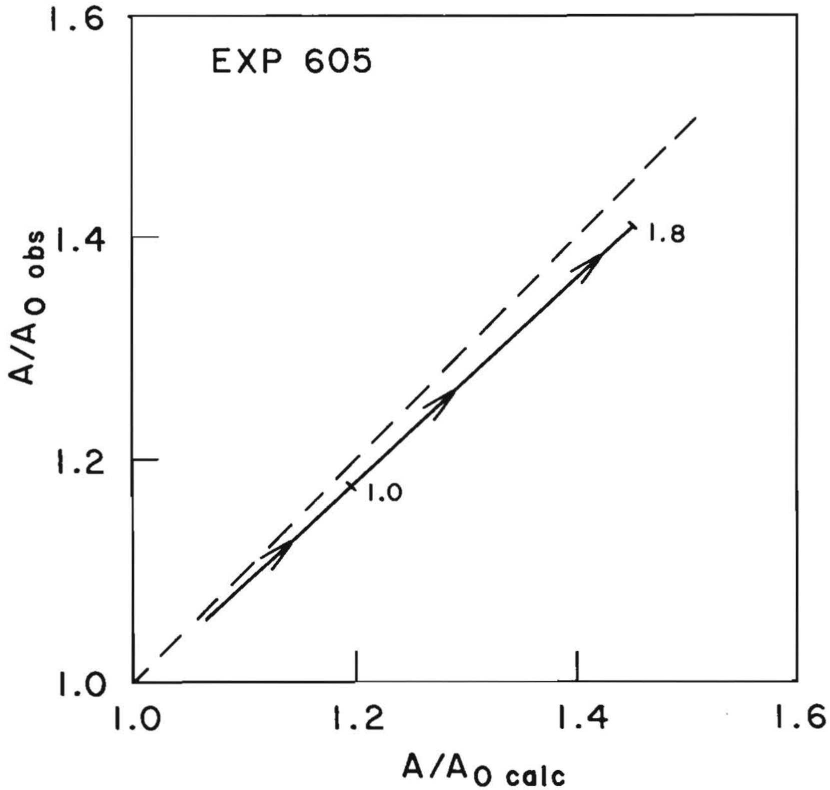


Fig. 15a 7. Comparison of calculated and observed drogue area for experiment 605. Numerals in the figure indicate the time in hours.

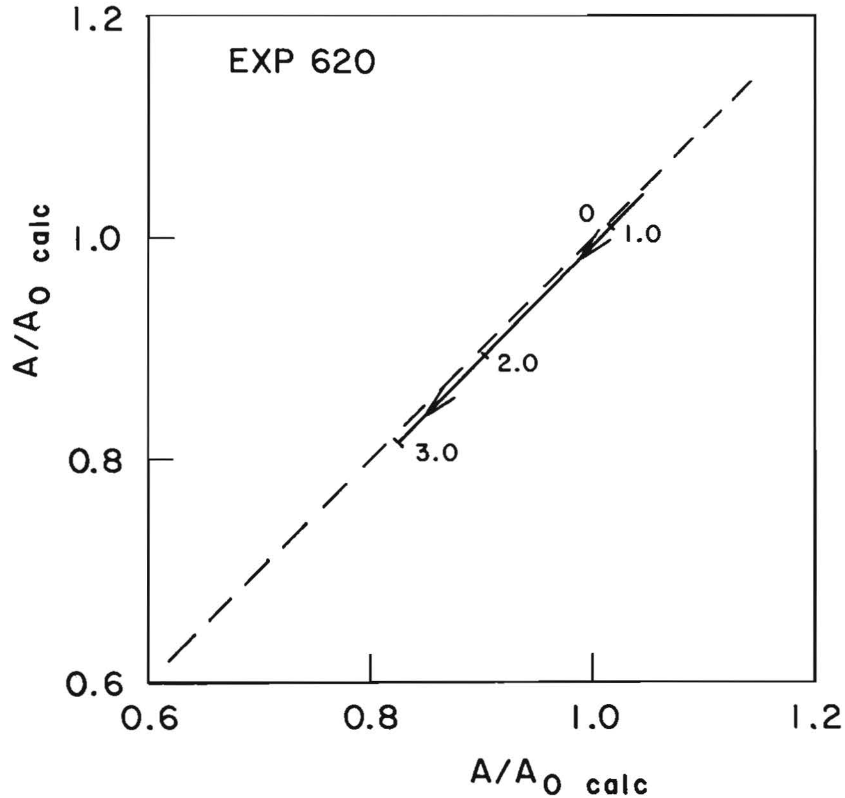


Fig. 15a 8. Comparison of calculated and observed drogue area for experiment 620. Numerals in the figure indicate the time in hours.

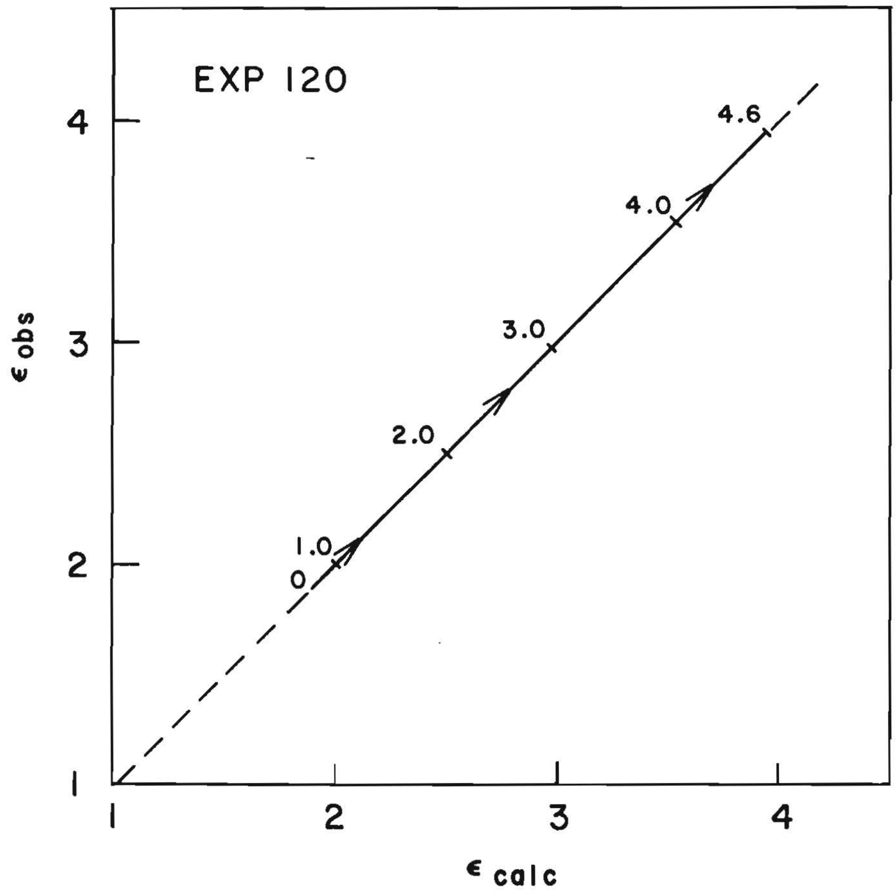


Fig. 15b 1. Comparison of calculated and observed elongations for experiment 120. Numerals in the figure indicate the time in hours.

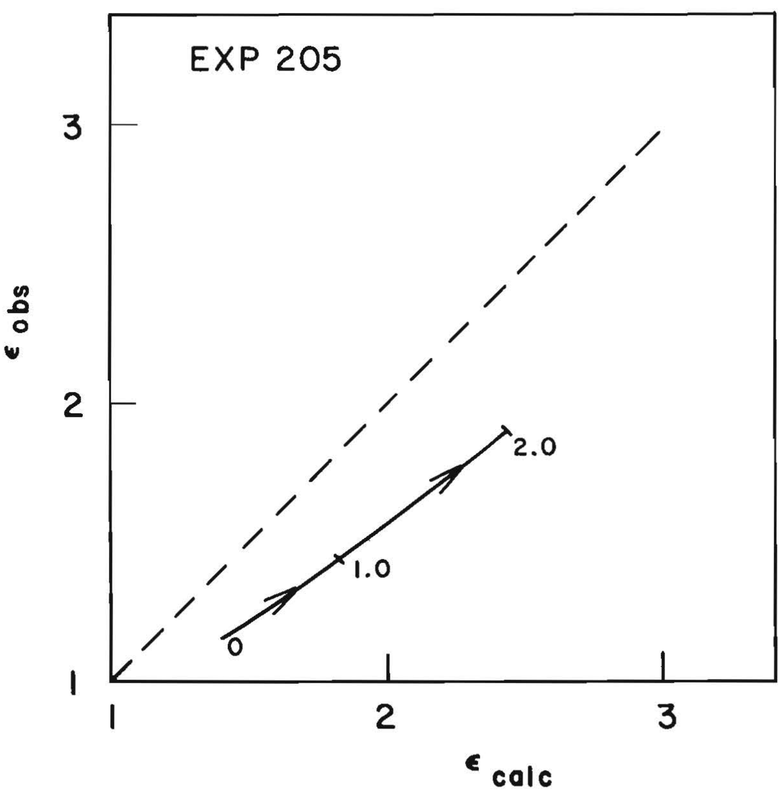


Fig. 15b 2. Comparison of calculated and observed elongations for experiment 205. Numerals in the figure indicate the time in hours.

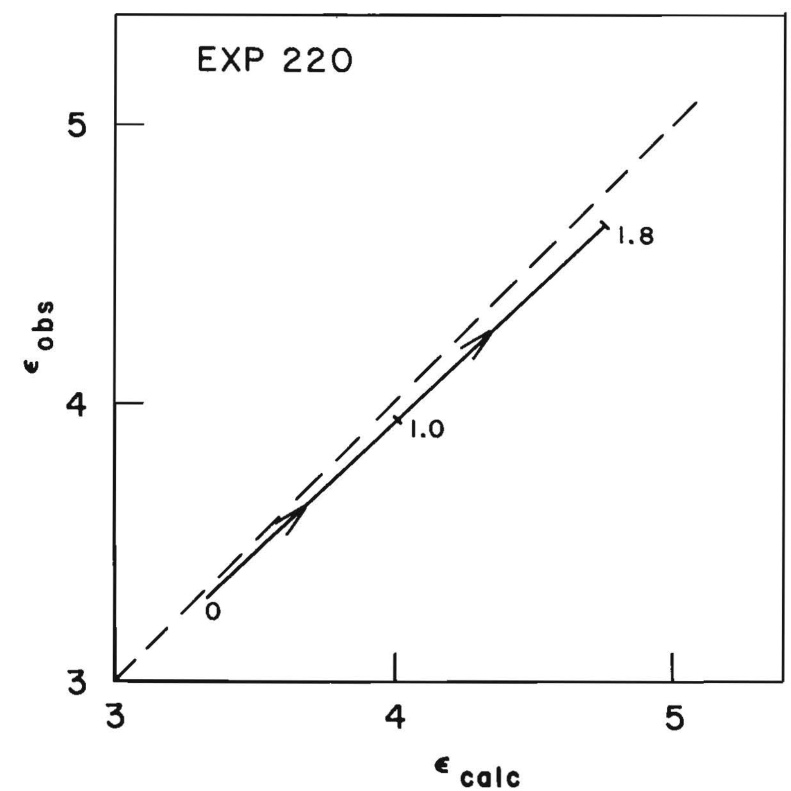


Fig. 15b 3. Comparison of calculated and observed elongations for experiment 220. Numerals in the figure indicate the time in hours.

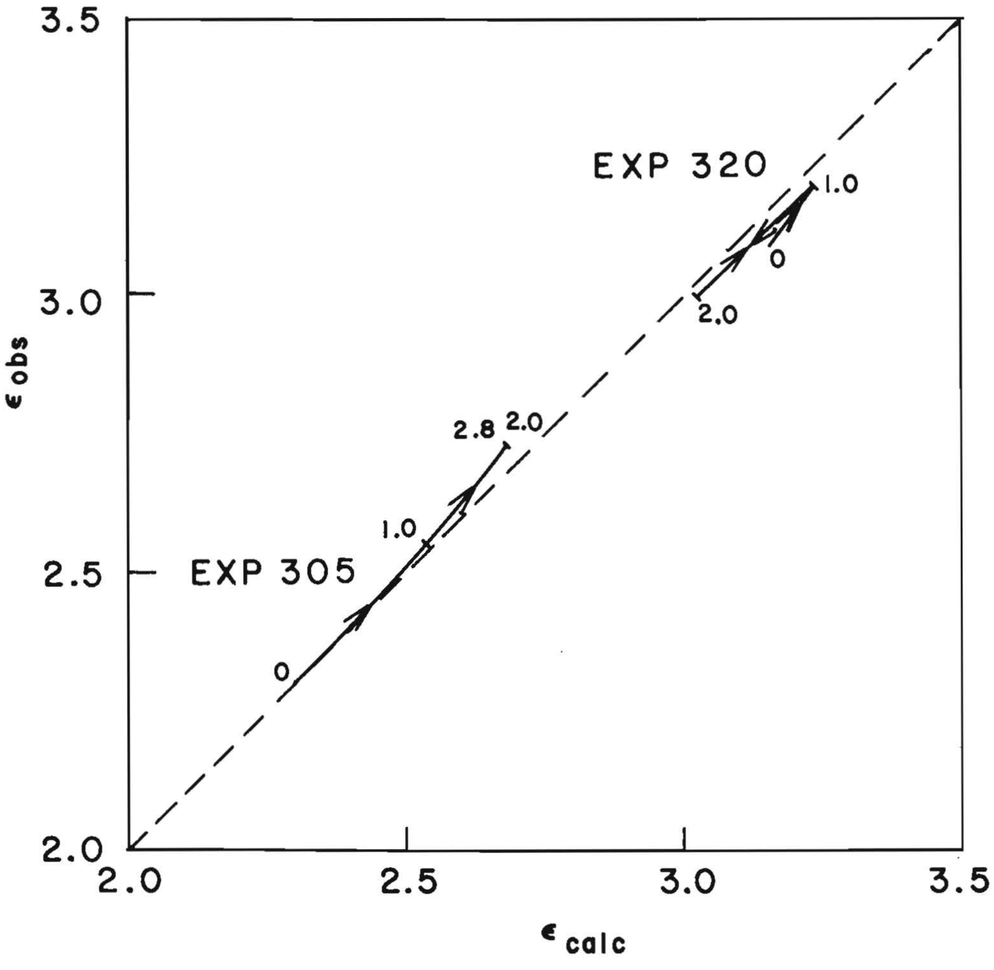


Fig. 15b 4. Comparison of calculated and observed elongations for experiments 305 and 320. Numerals in the figure indicate the time in hours.

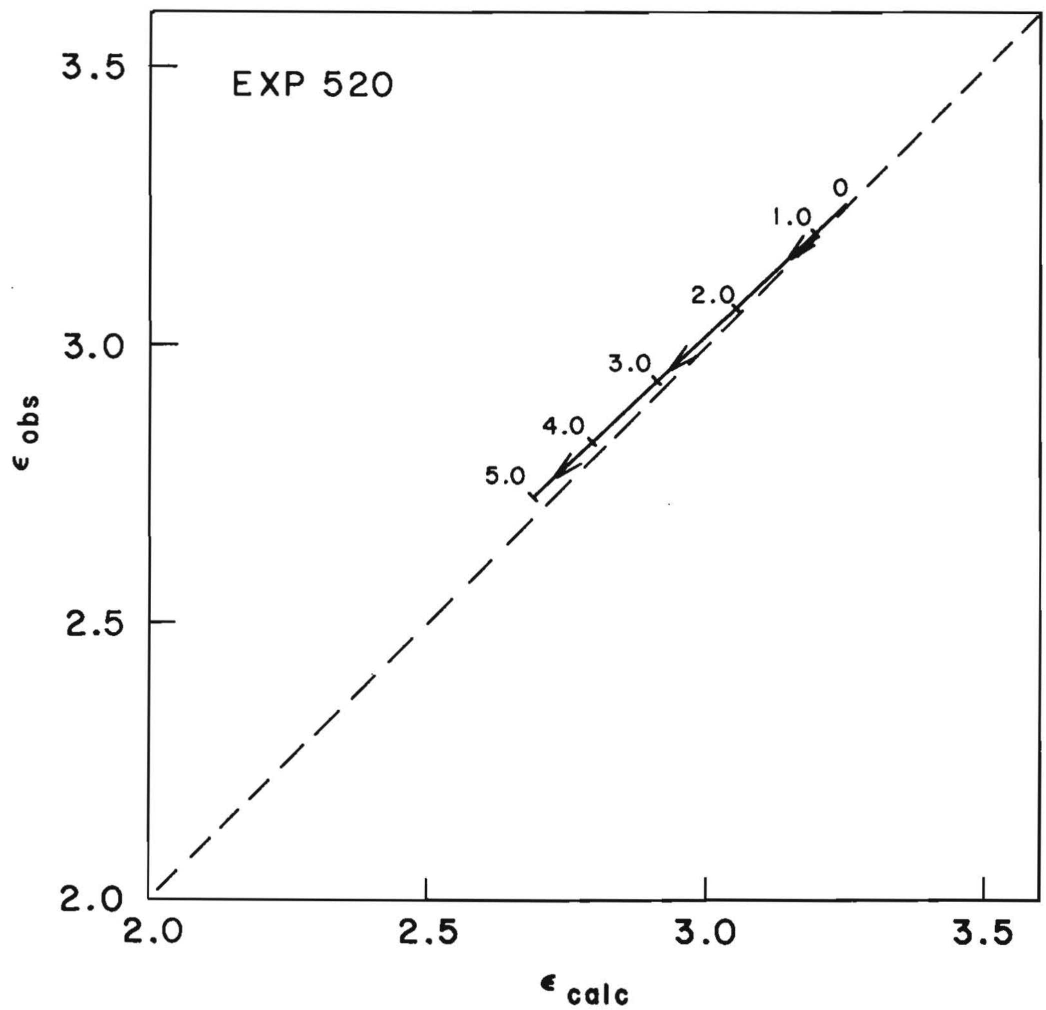


Fig. 15b 5. Comparison of calculated and observed elongations for experiment 520. Numerals in the figure indicate the time in hours.

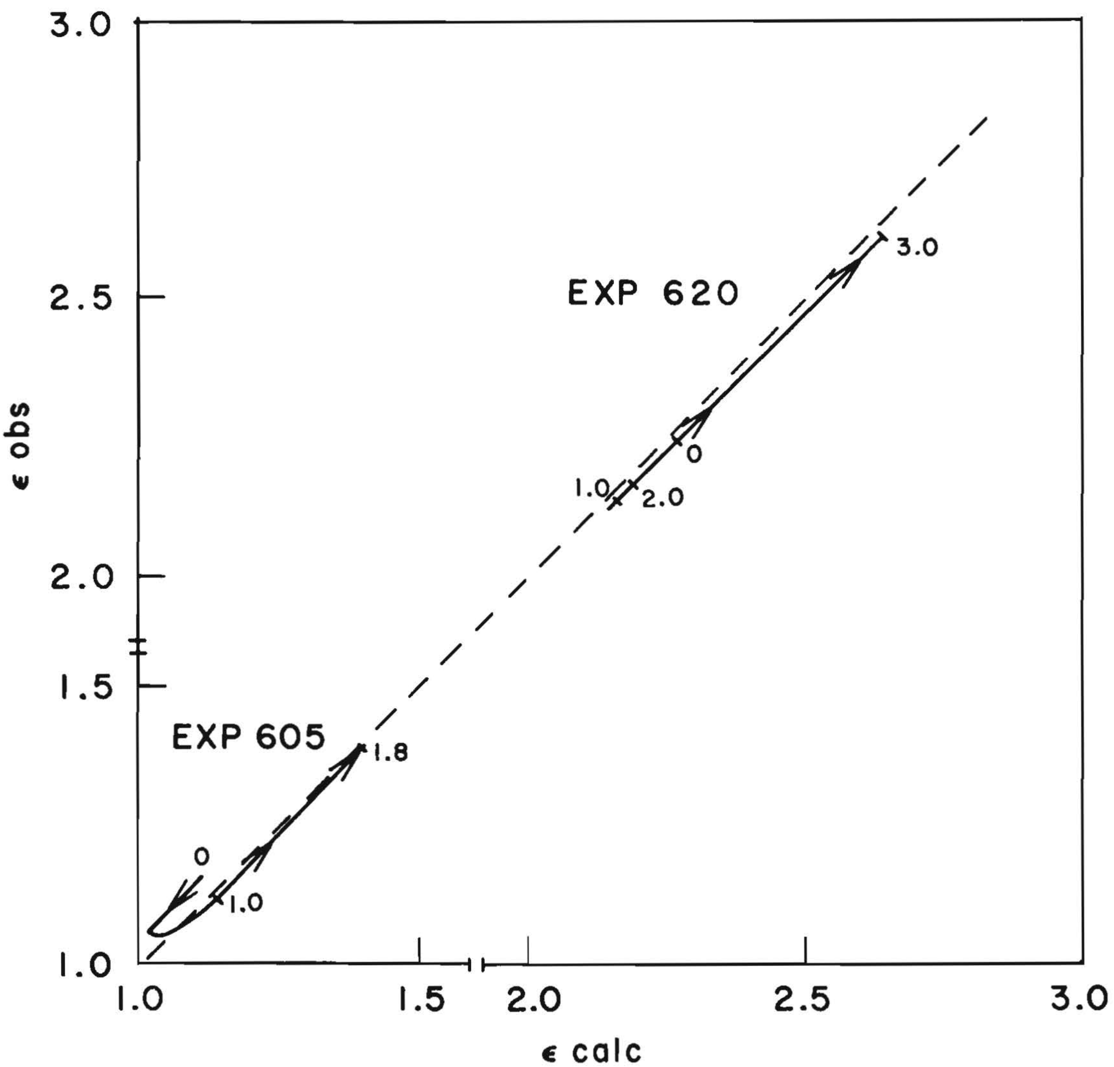


Fig. 15b 6. Comparison of calculated and observed elongations for experiments 605 and 620. Numerals in the figure indicate the time in hours.

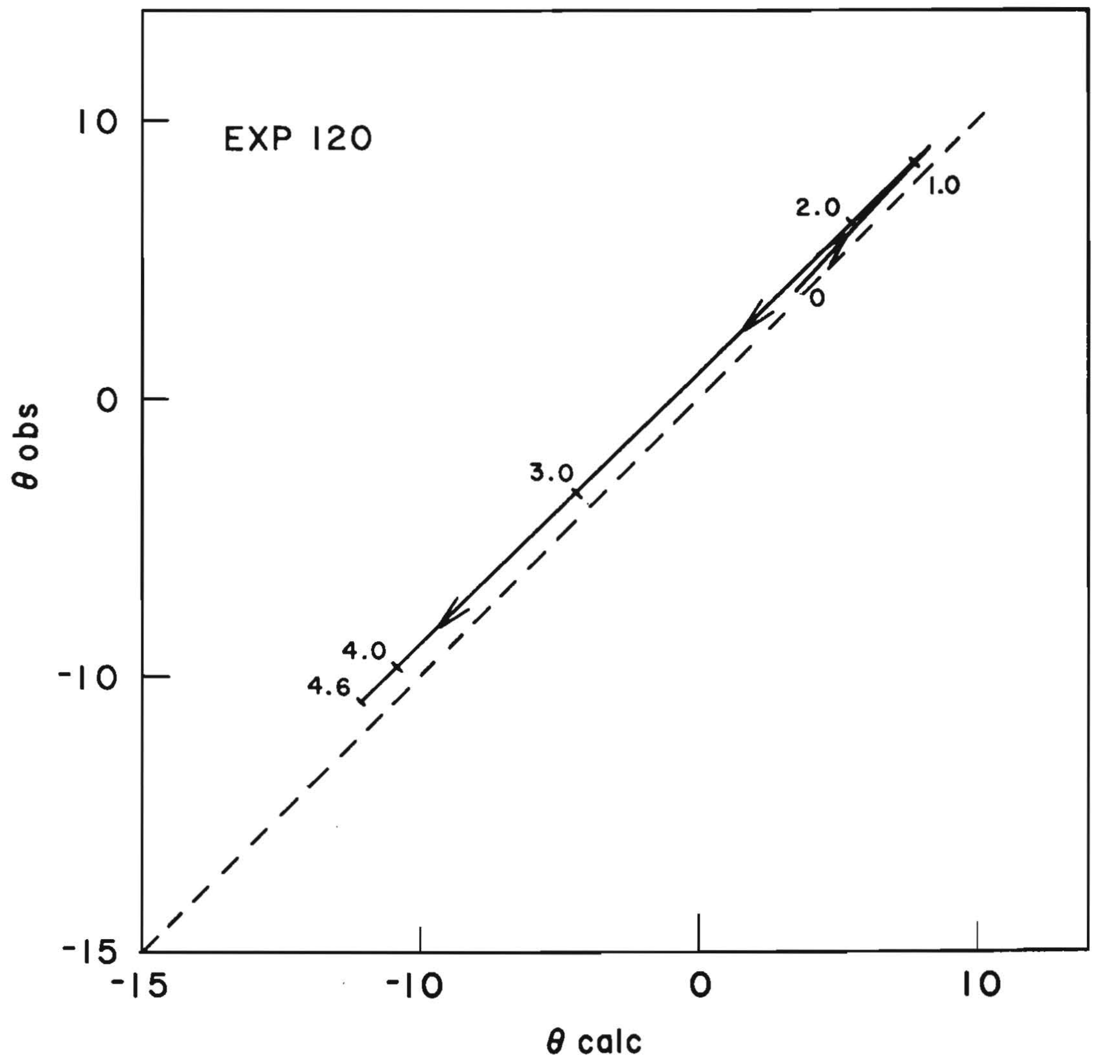


Fig. 15c 1. Comparison of calculated and observed orientation angles for experiment 120. Numerals in the figure indicate the time in hours.

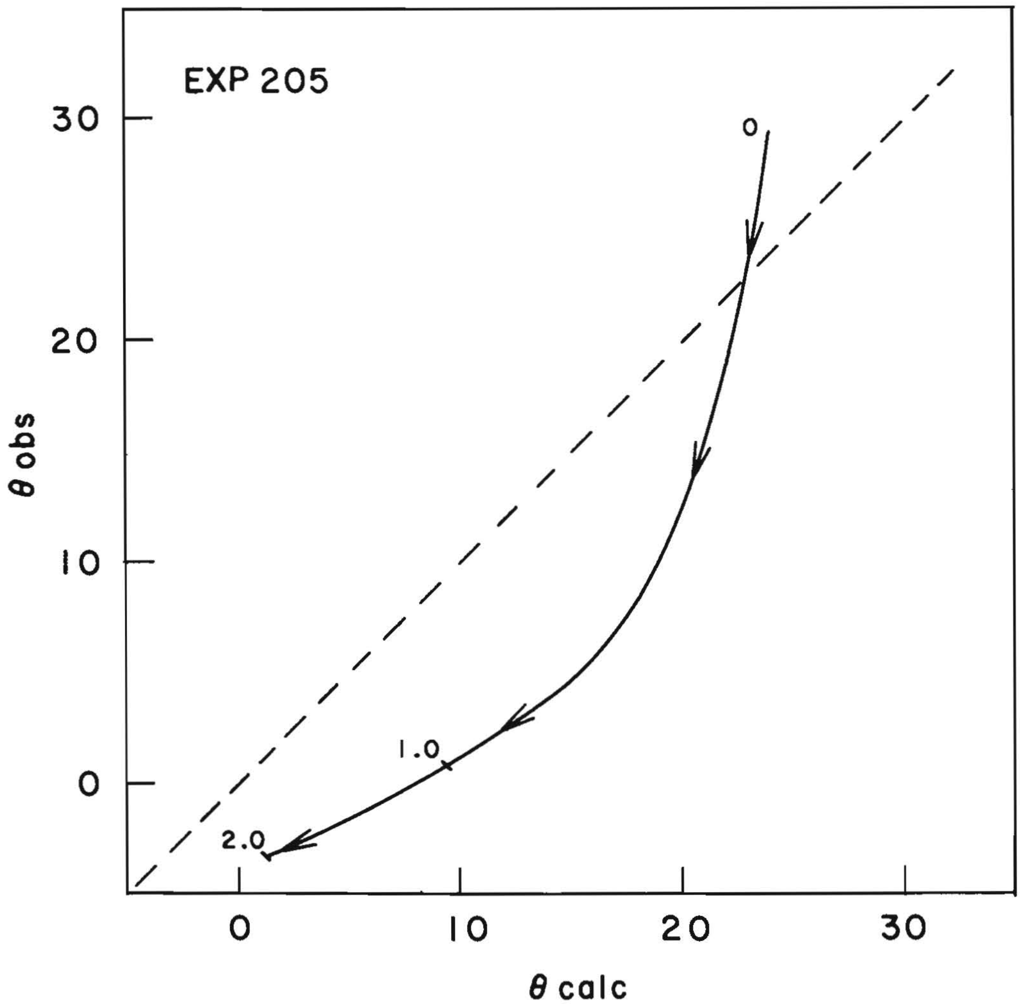


Fig. 15c 2. Comparison of calculated and observed orientation angles for experiment 205. Numerals in the figure indicate the time in hours.

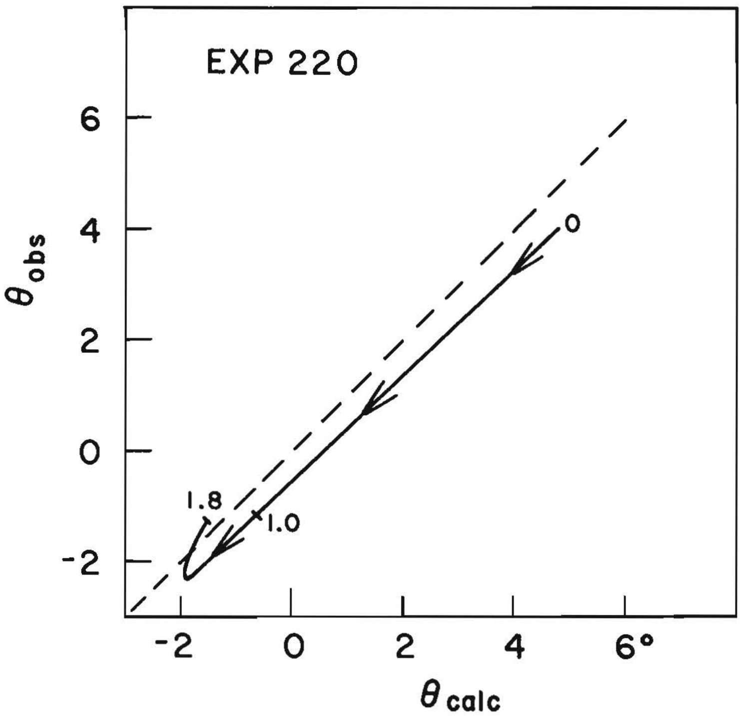


Fig. 15c 3. Comparison of calculated and observed orientation angles for experiment 220. Numerals in the figure indicate the time in hours.

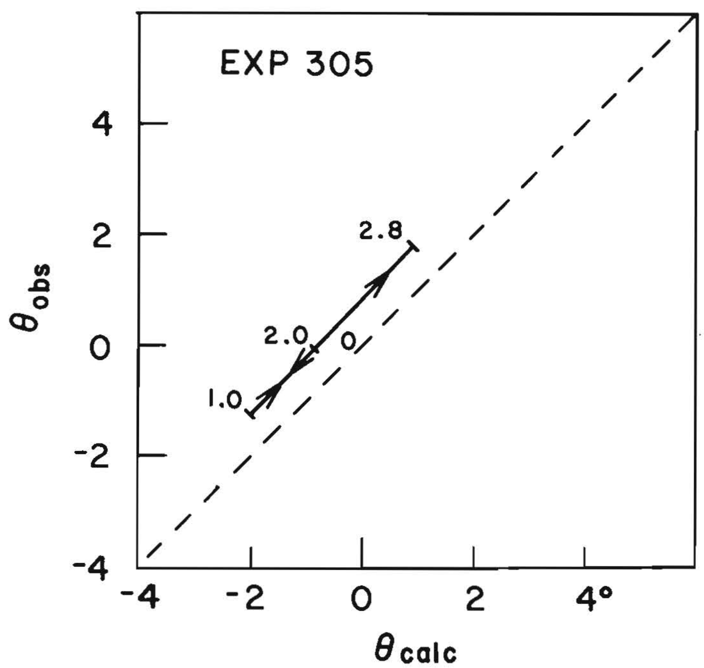


Fig. 15c 4. Comparison of calculated and observed orientation angles for experiment 305. Numerals in the figure indicate the time in hours.

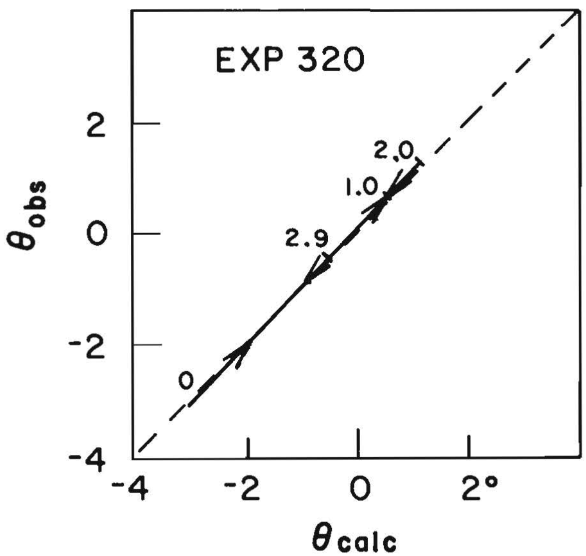


Fig. 15c 5. Comparison of calculated and observed orientation angles for experiment 320. Numerals in the figure indicate the time in hours.

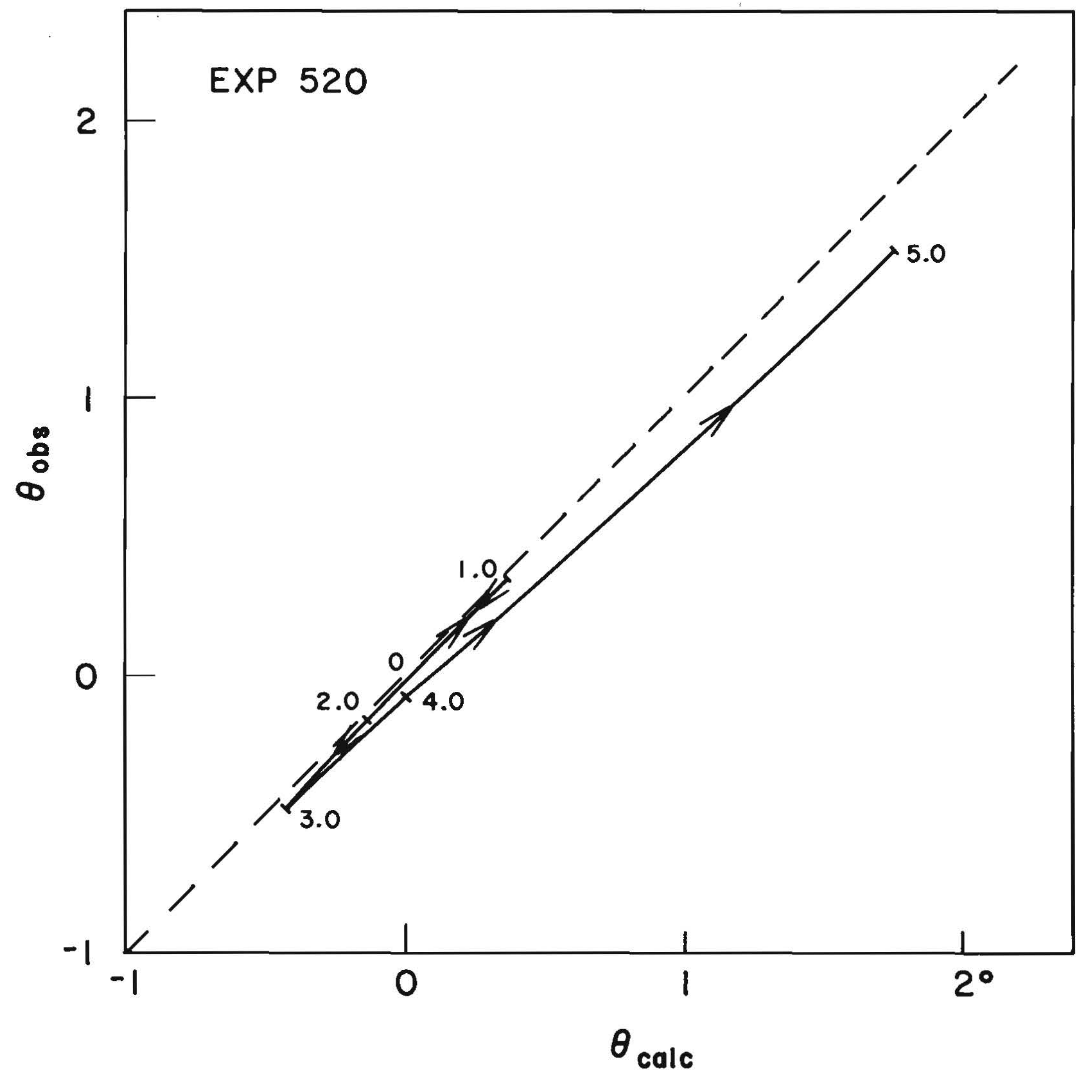


Fig. 15c 6. Comparison of calculated and observed orientation angles for experiment 520. Numerals in the figure indicate the time in hours.

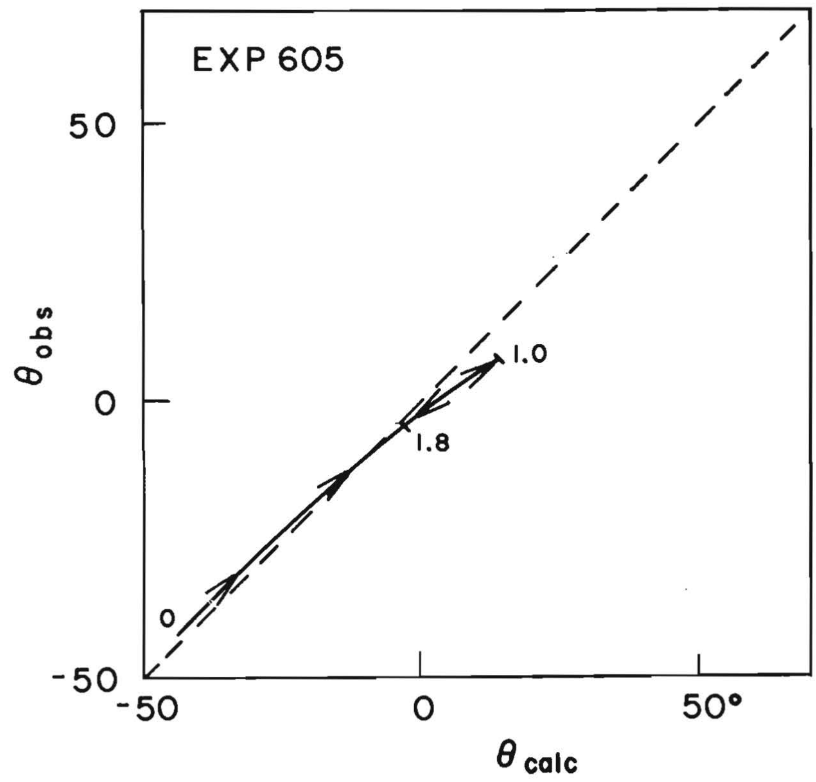


Fig. 15c 7. Comparison of calculated and observed orientation angles for experiment 605. Numerals in the figure indicate the time in hours.

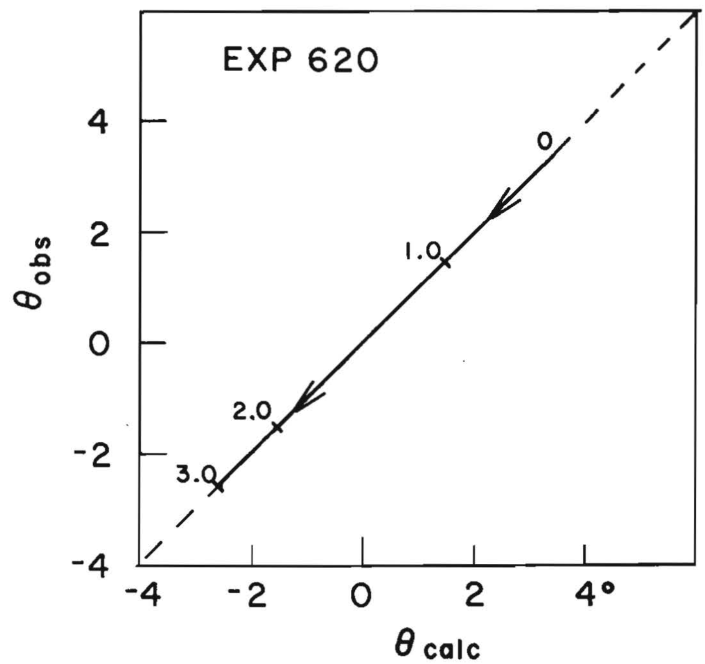


Fig. 15c 8. Comparison of calculated and observed orientation angles for experiment 620. Numerals in the figure indicate the time in hours.

## CHAPTER 6
## DISCUSSION

The linear regression procedure developed by OEH is shown to be a consistent method for evaluating Lagrangian deformations and diffusion coefficients. These characteristics in turn may be used to predict a concentration pattern from a generalized advection-diffusion equation. The entire scheme is internally consistent.

However, the analysis is based purely on kinematics. Recently Kirwan (1975) has pointed out the importance of oceanic velocity gradients in understanding both the kinematics and dynamics of oceanic motions. He derived equations governing the dynamic behavior of velocity gradients. It will be important to develop similar dynamical equations from Lagrangian deformations.

The analysis of smaller-scale variability demonstrates that drogues tend to cluster over local convergences while the overall groups of clusters tend to diverge. This finding points out the need for further investigation on the dynamics of convergence fields. The real mechanism of convergences and divergences may be closely related to the Langmuir cells (Assaf, Gerard and Gordon, 1971). In this context the difference between drogue dispersion (2-dimensional diffusion) and dye dispersion (3-dimensional diffusion) should be studied more seriously. Field experiments in an area of well defined circulation will be necessary.

## ACKNOWLEDGMENTS

The authors are grateful to John S. Farlow, EPA, New Jersey, for his helpful advice in editing the original drogue data.

---

## BIBLIOGRAPHY

Assaf, G., R. Gerard, and A. L. Gordon. 1971. Some mechanisms of oceanic mixing revealed in aerial photographs. J. Geophys. Res. 76:6550-6572.

Corrsin, S. 1962. Theories of turbulent dispersion. *In* Mechanics of Turbulence, Internat. Symp. of Nat. Sci. Res. Center, Marseille, Aug. 28-Sept. 2, 1961, Gordon and Breach Science Publishers, New York.

Ebbesmeyer, C. C. 1975. Computing current shear from dye observations using one of Okubo's advective-diffusive models. J. Phys. Oceanogr. 5:191-193.

Ebbesmeyer, C. C., and J. M. Helseth. 1975. A study of current properties and mixing using drogue movements observed during summer and winter in central Puget Sound, Washington. Final report dated June 1975 from Evans-Hamilton, Inc. to the Municipality of Metropolitan Seattle. 81 p.

Ebbesmeyer, C. C., A. Okubo, J. M. Helseth, and A. S. Robbins. 1976. Relative importance of current shear and eddy diffusion in dispersing current followers (in preparation).

Farlow, J. S. 1965. A field technique used for horizontal diffusion studies in Lakes Michigan and Erie. Pub. No. 13, Great Lakes Research Division, The University of Michigan, p. 299-303.

Kirwan, A. D. 1975. Oceanic velocity gradients. J. Phys. Oceanogr. 5:729-735.

Molinari, R., and A. D. Kirwan. 1975. Calculations of differential kinematic properties from Lagrangian observations in the Western Caribbean Sea. J. Phys. Oceanogr. 5:361-368.

Okubo, A. 1966. A note on horizontal diffusion from an instantaneous source in a nonuniform flow. J. Oceanogr. Soc., Japan. 22:35-40.

Okubo, A. 1970. Horizontal dispersion of floatable particles in the vicinity of velocity singularities such as convergences. Deep-Sea Res. 17: 445-454.

Okubo, A., and J. S. Farlow. 1967. Analysis of some Great Lakes drogue studies. Proceedings Tenth Conference on Great Lakes Research. p. 299-308.

Okubo, A., and J. L. Verber. 1967. Drogue studies, Chapter 8 of "Lake Currents." Technical Rept. F.W.P.C.A. Great Lakes Region, Illinois. November 1967.

Okubo, A., and C. C. Ebbesmeyer. 1976. Determination of vorticity, divergence, and deformation rates from analysis of drogue observations. Deep-Sea Res. (in press).

Okubo, A., C. C. Ebbesmeyer and J. M. Helseth. 1976. Determination of Lagrangian deformations from analysis of current followers. (Submitted to J. Phys. Oceanogr.).